EXPERIMENTAL INVESTIGATION OF THE BEHAVIOR OF BURIED PIPES UNDER VERTICAL LOADS

by

Baran Tulan

B.S., Civil Engineering, Istanbul Technical University, 2020

Submitted to the Institute for Graduate Studies in
Science and Engineering in partial fulfillment of
the requirements for the degree of
Master of Science

Graduate Program in Civil Engineering

Boğaziçi University

2024

ACKNOWLEDGEMENTS

First of all, I would like to thank my thesis supervisor Prof. Özer Çinicioğlu for giving me the opportunity to complete my master's degree under her guidance. During his guidance, I was very impressed by both his competence in geotechnical engineering and his approach to his students. I am grateful to him for being a role model in both my professional and daily life.

I would like to also thank my co-advisor Assist. Prof. Selçuk Bildik for enlightening me with his extensive knowledge and never-ending support. I solved many problems I encountered in my study with the help of his critical and solution-oriented perspective.

I place on record, my sincere gratitude to member of thesis committee, Assoc.Prof. Ilgın Yaşar and Assist. Prof. Berrak Teymür, for their valuable contributions.

I also would like to express my gratitude to my friends Gizil Tak and Peter Rogenbuke. I am very proud that we did this work with a great team spirit and I hope our friendship will remain forever.

I would like to thank my mother very much; without her, I would not have achieved anything I have achieved in my life.

I would like to express my appreciation to Türkiye Bilimsel ve Teknolojik Araştırma Kurumu (TUBITAK) for supporting me financially. This project was supported by TUBITAK, with Project Number: 116R020.

ABSTRACT

EXPERIMENTAL INVESTIGATION OF THE BEHAVIOR OF BURIED PIPES UNDER VERTICAL LOADS

In today's developed cities, buried pipes have been one of the most essential parts of society's well-being for a long time due to their functions. Since they are buried, it is complicated to detect any damage that has occurred to them and even if they are detected, the cost of repairing the damage is very high. One of the most common problems in buried pipes is deformation and the source of this is mostly the vertical loads acting on it. Buried pipe location, which determines burial depth and horizontal distance from the load source, properties of backfill soil such as relative density and pipe material properties are the main parameters affect the pressure acting on the pipe. In this study, small-scale laboratory model tests were conducted in a rigid test box at 1g to determine the effects of pipe location and relative density of backfill on pipe stresses and bearing capacity of the backfill soil. Model tests were conducted with and without a buried pipe. Strain gauges attached to buried pipes were used to record the pipe stresses and the chosen backfill was sand. A model footing was loaded in the model experiments until a predetermined settlement value was reached. A load cell was used to measure load values. Settlements were detected using LVDT transducers. Resulting displacements on the backfill soil are visualized and determined by analyzing consecutive photographs of the model tests' loading process using Particle Image Velocimetry (PIV) software, which is a MATLAB based image analysis module. A total of 18 model tests were performed, three of which were conducted without the buried pipe as a reference. In the model tests, buried depth, horizontal distance from the foundation and relative density of the backfill varied systematically. Obtained data was analyzed and the results were discussed in this study.

ÖZET

GÖMÜLÜ BORULARIN DİKEY YÜKLER ALTINDA DAVRANIŞLARININ DENEYSEL OLARAK İNCELENMESİ

Günümüzün gelişmiş şehirlerinde gömülü borular, işlevleri gereği uzun zamandır toplum refahının en önemli parçalarından biri olmuştur. Gömülü oldukları için üzerlerinde oluşan herhangi bir hasarın tespit edilmesi karmaşıktır ve tespit edilse bile hasarın onarılmasının maliyeti oldukça yüksektir. Gömülü borularda en sık karşılaşılan sorunlardan biri deformasyondur ve bunun kaynağı çoğunlukla üzerine etkiyen düşey yüklerdir. Gömme derinliğini ve yük kaynağından yatay mesafeyi belirleyen gömülü borunun konumu, sıkılık gibi dolgu zeminin özellikleri ve boru malzemesi özellikleri, boruya etkiyen basıncı etkileyen ana parametrelerdir. Bu çalışmada, boru konumu ve dolgunun sıkılığının boru gerilmeleri ve dolgu zeminin taşıma kapasitesi üzerindeki etkilerini belirlemek için 1 g'lik rijit bir test kutusunda küçük ölçekli laboratuvar model testleri yapılmıştır. Model testleri gömülü borulu ve borusuz olarak gerçekleştirilmiştir. Boru gerilimlerini kaydetmek için gömülü borulara takılan gerinim ölçerler kullanılmıştır ve seçilen dolgu malzemesi kum olarak seçilmiştir. Yük değerlerini ölçmek için yük hücresi kullanılmıştır. Oturmalar LVDT dönüştürücüler kullanılarak tespit edilmiştir. Dolgu zeminde ortaya çıkan yer değiştirmeler, MATLAB tabanlı bir görüntü analiz modülü olan Parçacık Görüntüleme Hız Ölçümü (PIV) yazılımıyla, model testlerinin yükleme sürecinin ardışık fotoğrafları analiz edilerek görselleştirilmiş ve belirlenmiştir. Toplam 18 model testi gerçekleştirilmiştir ve bunların üçü referans olarak kullanılmak amacıyla gömülü boru olmadan gerçekleştirilmiştir. Model testlerde gömülü derinlik, temelden yatay uzaklık ve dolgunun sıkılığı sistematik olarak değiştirilmiştir. Elde edilen veriler analiz edilmiş ve sonuçlar bu çalışmada tartışılmıştır.

TABLE OF CONTENTS

ACKNOWLEDGEMENTS iii
ABSTRACT iv
ÖZET v
LIST OF FIGURES viii
LIST OF TABLES xvii
LIST OF SYMBOLS xxii
LIST OF ACRONYMS/ABBREVIATIONS xxiv
1. INTRODUCTION 1
2. LITERATURE REVIEW 2
2.1. Introduction 2
2.2. Experimental Investigations on Buried Pipes 5
2.2.1. Static Load Model Tests 5
2.2.2. Dynamic Load Model Tests 10
2.3. Bearing Capacity Failure Mechanisms of Shallow Foundations 13
2.3.1. General Shear Failure 14
2.3.2. Punching Shear Failure 15
2.3.3. Local Shear Failure 16
2.3.4. Failure Surfaces 17
2.4. Particle Image Velocimetry Method In Geotechnical Engineering 18
3. EXPERIMENTAL METHODOLOGY 25
3.1. Physical Model Test Setup 25
3.1.1. Test Box 25
3.1.2. Model Footing 25
3.1.3. Linear Variable Differential Transformer (LVDT) Transducer . . 26
3.1.4. Load Cells 27
3.1.5. Strain Gauges 30
3.1.6. Pipe Properties 31
3.1.7. Data Acquisition System 33

3.1.8. LabView Software 34
3.1.9. PIV Analysis 35
3.1.10. Camera 36
3.2. Properties of the Backfill Material 36
3.3. Required Mass Calculation for Predetermined Relative Density 38
3.4. Procedure of the Model Tests 39
4. RESULTS 45
4.1. Effect on Bearing Capacity and Soil Displacement 47
4.1.1. Model Tests Without Buried Pipe 47
4.1.2. Effect on Bearing Capacity and Soil Displacement 50
4.2. Pipe Location Effect on Bearing Capacity and Soil Displacement 85
4.2.1. Burial Depth Effect (D_r=35%) 85
4.2.2. Horizantal Distance Effect (D_r=35 H/B=0.75) 88
4.2.3. Burial Depth Effect (D_r= 50%) 90
4.2.4. Burial Depth Effect (D_r= 65%) 92
4.2.5. Horizantal Distance Effect (D_r= 65%, H/B= 0.75) 94
4.2.6. Horizantal Distance Effect (D_r = 65%, H/B = 1.5) 96
5. DISCUSSION 101
6. CONCLUSION 104
REFERENCES 106
APPENDIX A: MODEL FOOTING SETTLEMENT AND BASE PRESSURE VALUES OF MODEL TESTS 110
APPENDIX B: STRESSES ACTING ON A PIPE AND CORRESPONDING SETTLEMENT VALUES 119

LIST OF FIGURES

Figure 2.1. Experimental setup Won *et al.* (2004). 6

Figure 2.2. Schematic representation of model test setup 7

Figure 2.3. Three different orientation type: horizontal orientation (left), inverted orientation (middle) and enveloped orientation (right) Pires and Palmeria (2017). 8

Figure 2.4. Vertical stress acting on the crown of the pipe-surcharge pressure acting on model footing with different geogrid types and orientations Pires and Palmeria (2017). 8

Figure 2.5. Hoop stresses on bottom and top of the pipe with horizontal distance from the model footing Bildik and Laman (2019). 10

Figure 2.6. Hoop stresses on left and right side of the pipe with horizontal distance from the model footing Bildik and Laman (2019). 10

Figure 2.7. Schematic representation of model test setup Tafrahsi and Khalaj (2011). 11

Figure 2.8. Schematic representation of model test setup 13

Figure 2.9. Soil surface settlement and soil pressure with applied stresses Mehrjardi *et al.* (2012). 13

Figure 2.10. Typical load-displacement curve of general shear failure. 14

Figure 2.11. General shear failure. 14

Figure 2.12. Typical load-displacement curve of punching shear failure. 15

Figure 2.13. Punching shear failure. 15

Figure 2.14. Typical load-displacement curve of local shear failure. 16

Figure 2.15. Local shear failure. 16

Figure 2.16. Failure surface for shallow foundations. 17

Figure 2.17. Usage of images in PIV method White *et al.* (2003). 20

Figure 2.18. Movement accuracy diagram White *et al.* (2003). 20

Figure 2.19. Schematic represantation of tunnel under the buried pipe Marshall *et al.* (2010). 21

Figure 2.20. Settlement profile of pipe and settlement profile of soil just below the pipe obtained from PIV analysis for two pipe types Marshall *et al.* (2010). 22

Figure 2.21. Schematic representation of model test setup Wang *et al.* (2021). . 23

Figure 2.22. Shear strain contours under different burail depth obtained from PIV Wang *et al.* (2021). 24

Figure 3.1. Test box. 26

Figure 3.2. Strip steel model footing used in the model tests. 26

Figure 3.3. Spring system used in the model tests. 27

Figure 3.4. Location of the spring system on model footing. 27

Figure 3.5. Placement of the steel marbles. 28

Figure 3.6. LVDT transducers used in the model tests. 29

Figure 3.7. 500kg capacity S-Type Load Cell used in the model tests. 29

Figure 3.8. GFLA-6-50 model strain gauge used in the model tests. 30

Figure 3.9. Adhesive product used in the model tests. 31

Figure 3.10. Tape used in the model tests. 31

Figure 3.11. Model pipe used in the model tests. 32

Figure 3.12. NI-9237 bridge module. 33

Figure 3.13. NI-9949 terminal adapter. 34

Figure 3.14. NI-cDAQ-9179 chassis with NI-9237 bridge module attached. . . . 34

Figure 3.15. Algorithm flow in labView. 35

Figure 3.16. Meshed area (RoI). 36

Figure 3.17. The camera used in the model tests. 36

Figure 3.18. Granulometric curve. 37

Figure 3.19. Cleaned pipe. 40

Figure 3.20. Placement of strain gauge. 40

Figure 3.21. Numbered papers and SB tape attached on strain gauge. 42

Figure 3.22. Drill with a flat end. 42

Figure 3.23. Water gauge. 42

Figure 3.24. Spring system. 43

Figure 3.25. Test control panel. 43

Figure 3.26. LabView software strain front panel. 43

Figure 3.27. Test setup before the experiment. 44

Figure 3.28. Side view illustration of model test setup. 44

Figure 4.1. Investigated parameters. 45

Figure 4.2. T1-T4-T7 test setups, respectively. 48

Figure 4.3. Normalized base pressure-model footing settlement ratios for T1,T4 and T7. 49

Figure 4.4. Normalized base pressure at ultimate model footing settlement state for T1, T4 and T7. 49

Figure 4.5. Vectorial displacement vectors, resultant displacement contours and shear strain contours at S/B=10% (10mm) vertical model footing settlement for T1. 51

Figure 4.6. Vectorial displacement vectors, resultant displacement contours and shear strain contours at S/B=10% (10mm) vertical model footing settlement for T4. 52

Figure 4.7. Vectorial displacement vectors, resultant displacement contours and shear strain contours at S/B=10% (10mm) vertical model footing settlement for T7. 53

Figure 4.8. Vectorial displacement vectors comparison for T1, T4 and T7 at at S/B=10% (10mm) vertical model footing settlement. 54

Figure 4.9. Comparison 1 test setups (T2, T5 and T8, respectively). 55

Figure 4.10. Comparison 2 test setups (T3, T6 and T9, respectively). 56

Figure 4.11. Comparison 3 test setups (T10 and T13, respectively). 57

Figure 4.12. Comparison 4 test setups (T11 and T14, respectively). 57

Figure 4.13. Comparison 5 test setups (T12 and T15, respectively). 58

Figure 4.14. Normalized base pressure-model footing settlement ratios for T2,T5 and T8. 58

Figure 4.15. Normalized ultimate base pressure at ultimate model footing settlement state for T2, T5 and T8. 59

Figure 4.16. Vectorial displacement vectors, resultant displacement contours and shear strain contours at S/B=10% (10mm) vertical model footing settlement for T2. 61

Figure 4.17. Vectorial displacement vectors, resultant displacement contours and shear strain contours at S/B=10% (10mm) vertical model footing settlement for T5. 62

Figure 4.18. Vectorial displacement vectors, resultant displacement contours and shear strain contours at S/B=10% (10mm) vertical model footing settlement for T8. 63

Figure 4.19. Normalized base pressure-model footing settlement ratios for T3,T6 and T9. 65

Figure 4.20. Normalized ultimate base pressure at ultimate model footing settlement state for T3, T6 and T9. 65

Figure 4.21. Vectorial displacement vectors, resultant displacement contours and shear strain contours at S/B=10% (10mm) vertical model footing settlement for T3. 67

Figure 4.22. Vectorial displacement vectors, resultant displacement contours and shear strain contours at S/B=10% (10mm) vertical model footing settlement for T6. 68

Figure 4.23. Vectorial displacement vectors, resultant displacement contours and shear strain contours at S/B=10% (10mm) vertical model footing settlement for T9. 69

Figure 4.24. Normalized base pressure-model footing settlement ratios for T10 and T13. 71

Figure 4.25. Normalized ultimate base pressure-model footing settlement ratios for T10 and T13. 71

Figure 4.26. Vectorial displacement vectors, resultant displacement contours and shear strain contours at S/B=10% (10mm) vertical model footing settlement for T10. 73

Figure 4.27. Vectorial displacement vectors, resultant displacement contours and shear strain contours at S/B=10% (10mm) vertical model footing settlement for T13. 74

Figure 4.28. Normalized base pressure-model footing settlement ratios for T11 and T14. 75

Figure 4.29. Normalized ultimate base pressure-model footing settlement ratios for T11 and T14. 75

Figure 4.30. Vectorial displacement vectors, resultant displacement contours and shear strain contours at S/B=10% (10mm) vertical model footing settlement for T11. 77

Figure 4.31. Vectorial displacement vectors, resultant displacement contours and shear strain contours at S/B=10% (10mm) vertical model footing settlement for T14. 78

Figure 4.32. Normalized base pressure-model footing settlement ratios for T12 and T15. 80

Figure 4.33. Normalized ultimate base Pressure-model footing settlement ratios for T12 and T15. 80

Figure 4.34. Vectorial displacement vectors, resultant displacement contours and shear strain contours at S/B=10% (10mm) vertical model footing settlement for T12. 83

Figure 4.35. Vectorial displacement vectors, resultant displacement contours and shear strain contours at S/B=10% (10mm) vertical model footing settlement for T15. 84

Figure 4.36. Test setups of T16, T17 and T18, respectively. 86

Figure 4.37. Normalized base pressure-model footing settlement ratios for T1, T2 and T3. 87

Figure 4.38. Normalized ultimate base pressure-model footing settlement ratios for T1 T2 and T3. 87

Figure 4.39. Normalized base pressure-model footing settlement ratios for T1, T2, T10, T11 and T12. 89

Figure 4.40. Normalized ultimate base pressure-model footing settlement ratios for T10 T11 and T12. 89

Figure 4.41. Normalized base pressure-model footing settlement ratios for T4, T5, and T6. 91

Figure 4.42. Normalized ultimate base pressure-model footing settlement ratios for T4, T5 and T6. 91

Figure 4.43. Normalized base pressure-model footing settlement ratios for T7, T8, and T9. 93

Figure 4.44. Normalized ultimate base pressure-model footing settlement ratios for T7, T8 and T9. 93

Figure 4.45. Normalized base pressure-model footing settlement ratios for T7, T8, T13, T14 and T15. 95

Figure 4.46. Normalized ultimate base pressure-model footing settlement ratios for T7, T8, T13, T14 and T15. 95

Figure 4.47. Normalized base pressure-model footing settlement ratios for T7, T9, T16, T17 and T18. 97

Figure 4.48. Normalized ultimate base pressure-model footing settlement ratios for T16, T17 and T18. 97

Figure 4.49. Vectorial displacement vectors, resultant displacement contours and shear strain contours at S/B=10% (10mm) vertical model footing settlement for T16. 98

Figure 4.50. Vectorial displacement vectors, resultant displacement contours and shear strain contours at S/B=10% (10mm) vertical model footing settlement for T17. 99

Figure 4.51. Vectorial displacement vectors, resultant displacement contours and shear strain contours at S/B=10% (10mm) vertical model footing settlement for T18. 100

LIST OF TABLES

Table 2.1. Pipe stifness classes. 3

Table 2.2. Adaptability of trenchless installation methods under different soil types. R= Recommended, P= Possible, U= Unsuitable. 4

Table 3.1. Load cell specifications. 28

Table 3.2. Specifications of the strain gauge used in the model tests. 32

Table 3.3. Specifications of the pipe used in the model tests. 32

Table 3.4. Index properties. 37

Table 3.5. Strength properties. 38

Table 3.6. Required mass for every layer at three different relative densities. . 39

Table 4.1. Model test program. 46

Table 4.2. Classification of sand density according to the value of relative density Mithcell and Soga (2005). 47

Table 4.3. Ultimate base pressure values (q_u), model footing settlement ratios (S/B) and relative density values (D_r) for T1, T4 and T7. 48

Table 4.4. Relative density effect model tests comparisons. 50

Table 4.5. Ultimate base pressure values (q_u), model footing settlement ratios and pipe location for comparison 1 model tests. 55

Table 4.6. Ultimate base pressure values, pipe stress values and stress ratios at S/B=0.1 for bomparison 1 model tests. 60

Table 4.7. Ultimate base pressure values (q_u), model footing settlement ratios and pipe location for comparison 2 model tests. 64

Table 4.8. Ultimate base pressure values, pipe stress values and stress ratios at S/B=0.1 for comparison 2 model tests. 66

Table 4.9. Ultimate base pressure values (q_u), model footing settlement ratios and pipe location for comparison 3 model tests. 70

Table 4.10. Ultimate base pressure values, pipe stress values and stress ratios at S/B=0.1 for comparison 3 model tests. 70

Table 4.11. Ultimate base pressure values (q_u), model footing settlement ratios and pipe location for comparison 4 model tests. 72

Table 4.12. Ultimate base pressure values, pipe stress values and stress ratios at S/B=0.1 for comparison 4 model tests. 76

Table 4.13. Ultimate base pressure values (q_u), model footing settlement ratios and pipe location for comparison 5 model tests. 79

Table 4.14. Ultimate base pressure values, pipe stress values and stress ratios at S/B=0.1 for comparison 5 model tests. 81

Table 4.15. Ultimate base pressure values (q_u), model footing settlement ratios and pipe locations for comparison 6 model tests. 85

Table 4.16. Ultimate base pressure values (q_u), model footing settlement ratios and pipe locations for comparison 7 model tests. 88

Table 4.17. Ultimate base pressure values (q_u), model footing settlement ratios and pipe locations for comparison 8 model tests. 90

Table 4.18. Ultimate base pressure values (q_u), model footing settlement ratios and pipe locations for comparison 9 model tests. 92

Table 4.19. Ultimate base pressure values (q_u), model footing settlement ratios and pipe locations for comparison 10 model tests. 94

Table 4.20. Ultimate base pressure values (q_u), model footing settlement ratios and pipe locations for comparison 11 model tests. 96

Table A.1. Model footing and base pressure values of T1. 110

Table A.2. Model footing and base pressure values of T2. 110

Table A.3. Model footing and base pressure values of T3. 111

Table A.4. Model footing and base pressure values of T4. 111

Table A.5. Model footing and base pressure values of T5. 112

Table A.6. Model footing and base pressure values of T6. 112

Table A.7. Model footing and base pressure values of T7. 113

Table A.8. Model footing and base pressure values of T8. 113

Table A.9. Model footing and base pressure values of T9. 114

Table A.10. Model footing and base pressure values of T10. 114

Table A.11. Model footing and base pressure values of T11. 115

Table A.12. Model footing and base pressure values of T12. 115

Table A.13. Model footing and base pressure values of T13. 116

Table A.14. Model footing and base pressure values of T14. 116

Table A.15. Model footing and base pressure values of T15. 117

Table A.16. Model footing and base pressure values of T16. 117

Table A.17. Model footing and base pressure values of T17. 118

Table A.18. Model footing and base pressure values of T18. 118

Table B.1. Pipe stresses and corresponding settlement values in T2. 119

Table B.2. Pipe stresses and corresponding settlement values in T3. 119

Table B.3. Pipe stresses and corresponding settlement values in T5. 120

Table B.4. Pipe stresses and corresponding settlement values in T6. 120

Table B.5. Pipe stresses and corresponding settlement values in T8. 121

Table B.6. Pipe stresses and corresponding settlement values in T9. 121

LIST OF SYMBOLS

A	Area of the Foundation
B	Width of the Shallow Foundation
C	Relative Stiffness Parameter of Pipe
C_c	Coefficient of Curvature
C_u	Coefficient of Uniformity
c	Cohesion
c'	Effective Cohesion
D	Diameter of the Pipe
Df	Foundation Depth
D_{50}	Median Particle Size
D_r	Relative Density
E	Modulus of Elasticity
e	Void Ratio
e_{max}	Maximum Void Ratio
e_{min}	Minimum Void Ratio
F	Relative Stiffness Parameter of Pipe
G_s	Specific Gravity
H	Vertical Distance between Buried Pipe and the Foundation
K_{py}	Passive Earth Pressure Coefficient
L	Length of the Shallow Foundation
Q	Base Pressure
q	Surcharge Pressure
S	Settlement
St	Stress Ratio
x	Horizontal Distance between Buried Pipe, Model Footing
$\Delta S/\Delta q$	Settlement to Load Ratio
ε	Strain

Φ	Friction Angle
Φ'	Effective Friction Angle
γ	Unit Weight (kN/m^3)
γ_w	Unit Weight of water (kN/m^3)
σ	Stress (kPa)
σj	Stress Value from Relevant Strain Gauge (kPa)

LIST OF ACRONYMS/ABBREVIATIONS

2D	Two Dimensional
3D	Three Dimensional
ASTM	American Society for Testing and Materials
BCR	Bearing Capacity Ratio
EPS	Expanded Polystrene
FBG	Fiber Bragg Gatting
FEM	Finite Element Method
HDPE	High Density Polyethylene
LPT	Linear Position Transducer
LVDT	Linear Variable Differential Transformer
N.D.	No Data
PIV	Particle Image Velocimetry
PVC	Polyvinyl Chloride
SW	Well Graded Sand
uPVC	Unplasticized Polyvinyl Chloride
USCS	Unified Soil Classification System

1. INTRODUCTION

Pipeline systems have a great importance to day to day life of today's people. Sewer systems help the management and sustainability of the cities; oil pipelines contribute significantly to the production process of goods and the transportation of vehicles by carrying fuel. Leaking, cracking, or any other structural or geotechnical failure pipelines might create enormous economic or physical devastation; therefore, necessary calculations should be done before installing pipeline systems and precautions should be taken before and after the placement.

The engineering behavior of buried pipes can be understood by construing stresses and strains. In the literature, most studies conducted on buried pipes used stresses acting on pipes to discern the behavior of both pipes and the surrounding soil; nevertheless, these studies predominantly include only measurements of stresses and strains; they do not combine measurements with image analysis.

In the extent of this thesis and TUBITAK Project No: 116R020A, an integrated study was conducted between image analysis and physical model tests. Physical model tests were done in a rigid box where pipes were placed in different locations inside the rigid box. The loading phases of the physical model tests were done by a modeled shallow foundation, which was placed on top of the fill materials, which have different relative densities. Fill materials were chosen as the same sand of different relative densities. The location effect of the pipe on pipe pressure was obtained by different types of data recorders, which can measure both load on the foundation model and displacement on the foundation model. Displacement and shear strain of the fill material were obtained by the image analysis with a method of Particle Image Velocimetry (PIV). The interaction behavior of buried pipes in different relative density backfills and the effect of pipe locations on this behavior were examined in detail with the results from both PIV analyses and data recorders.

2. LITERATURE REVIEW

2.1. Introduction

Since ancient times, buried pipeline systems have been engineering structures used for transportation and transmission. Buried pipes are still important engineering structures because they are more advantageous than other transportation methods in terms of pipeline safety, environmental and economical factors. They form the mandatory structures for today's cities, such as drinking water systems, sewage systems, drainage systems, gas lines and heat transmission systems. As buried pipeline systems are generally located in urban areas, they affect both the comfort and safety of the people; therefore, they need to be designed irreproachable. In order to design buried pipeline systems without causing any errors, it is necessary to analyze their interaction with filling soil and design them for their service time against static and dynamic loads.

As with all engineering structures, behavior with surrounding components is crucial in buried pipeline systems. According to Moore (2001), buried pipes are divided into four categories according to their stiffness behavior relative to the surrounding soil, which are rigid, semi-flexible, flexible and compressible. To define soil-pipe systems' rigidity behavior, Hoeg (1968)'s relative stiffness parameters F and C can be used. F and C are both dependent properties of pipe and soil, such as section properties of the pipe, soil's elastic modulus, soil's poissons ratio and elastic modulus of the pipe wall. As can be seen in the Table below, lower F and C values represent higher soil-pipe system rigidity behavior. The major difference between rigid and flexible pipes defined according to the C and F values is the effect of soil modulus on the deformations and bending moments of buried pipes. In rigid pipes, the filling soil spreads the earth pressures around the circumference without changing the magnitude. In flexible pipes, the stress distribution is more uniform and generally, pipe deflections occur because of the uniform stress; therefore, the soil modulus has a significant effect on the behavior of flexible pipes. Besides, for practical design purposes, rigid pipes are considered to

experience zero deformation, whereas in some standards, flexible pipes are considered to undergo at least 2% deformation according to their radius without causing any structural damage to the pipe-soil system.

Table 2.1. Pipe stifness classes.

Pipe Class	C values	F valuse
Rigid pipe	0.1>C	0.1>F
Semi-rigid pipe	0.1>C	10>F>0.1
Flexible pipe	0.1>C	F>10
Compressible pipe	100>C>0.1	F>10
Empty cavity	C>100	F>10

Another important parameter which affects soil-pipe behavior is the placement of the buried pipes. According to Spangler and Handy (2007), there are two major classes of placement of the buried pipes, which are ditch conduit and positive projective conduit. In ditch conduits, pipes are placed in a narrow ditch and filled with earth backfill. Sewers, drains and water mains are usually designed with this placement method. A positive projecting conduit with its top projecting above, the natural ground surface is erected in shallow bedding, where the pipe is installed and subsequently covered with an embankment. Most railway and highway culverts are designed by this method. Furthermore, there are two minor classes of placement methods, which are negative projecting conduit method and imperfect ditch method. A negative projecting conduit method was enhanced to decrease soil pressure on buried pipes under a fill. Soil pressure reduces by installing the pipes in a shallow ditch before it is covered with the embankment. In this method, the top of the buried pipes must be lower than the surrounding soil, which provides settlement on the soil column over the conduit, which leads to support by created friction. The imperfect ditch method is nearly the same with the negative projection method, except in this method, trenches are placed into the embankment over the conduit and filled with compressible soil. This method also provides a decrease in soil pressure; nevertheless, it is not recommended to use this method in water barriers since the loose backfill may allow seepage.

In today's cities, buried pipelines are extensive and complex. Without maintenance and less use of live spaces of the piping systems, cities can only deteriorate. Without well-maintained cities, the quality of human life deteriorates. Therefore, engineers propound the idea of trenchless technology on buried pipelines' placement. According to Lu *et al.* (2020), there are eight methods for buried pipe installation in trenchless technology. The methods are horizontal auger boring, horizontal directional drilling, pipe jacking, microtunneling, impact moling, pipe ramming and direct pipe. These methods have numerous advantages compared to traditional methods: high construction precision, low personnel usage, high safety, working under harsh geological conditions, small earthwork volume, accurate direction control, economic efficiency, short construction period and sustainability. Although trenchless methods have various benefits, they also have limitations. The most crucial factor of buried pipeline placement is soil type and not all methods are suitable for all soil types. The suitability of trenchless methods are listed in Table 2.2.

Table 2.2. Adaptability of trenchless installation methods under different soil types. R= Recommended, P= Possible, U= Unsuitable.

Soil type	**HAB**	**HDD**	**PJ**	**MT**	**IM**	**PR**	**DP**
Extremely soft to soft clay	P	R	P	P	U	R	R
Medium to hard clay	R	R	R	R	R	R	R
Hard clay and highly weathered chale	R	P	R	R	P	R	P
Loose sand	R	R	P	P	U	P	R
Medium to dense sand (above groundwater level)	R	R	R	R	R	P	R
Medium to dense sand (below groundwater level)	R	R	R	R	U	P	R
Gravel (particle size: 1.96-3.93 in.)	R	R		R	P	R	R
Gravel (particle size: 3.93-5.9 in.)	P	R	R	P	U	R	R
Weathered rock and hard soil	R	R	R	R	U	U	R
Microweathered and unweathered rock	U	R	R	R	U	U	R

2.2. Experimental Investigations on Buried Pipes

Analysis of the soil-buried pipeline interaction can be done by analytical investigations (Kou and Shukla, 2019), numerical studies (Daiyan *et al.* 2010), full-scale tests (Paulin *et al.* 1998) and physical model laboratory tests (Maljaei *et al.* 2021). Experimental studies often focus on primary factors that affect the bearing capacity of the soil-buried pipe system and the pressure on the pipe. These factors are the backfill relative density, pipe location, reinforcement and loading conditions. Geosynthetics have mostly been used as reinforcements. The performance of the soil-buried pipe system has been researched in relation to the effects of geosynthetic type, location of geosynthetic and properties of geosynthetic. Some of the experimental studies related to soil-buried pipe interaction will be briefly reviewed in this section.

2.2.1. Static Load Model Tests

Won *et al.* (2004) conducted laboratory experiments to examine the deformations of PVC pipes in reinforced soil. The experiments were carried out in a test box measuring 880x450x980 mm. Two different types of geogrids were used for soil reinforcement. In order to measure the stresses in the pipe during the experiment, four strain gauges were placed on the pipe. As a result of the experiments, it was seen that the use of a single geogrid contributed significantly to the bearing capacity and the deformations in the pipe were significantly reduced. It has been observed that the bearing capacity does not increase further if more than two layers of geogrid are used. It is observed that the geogrid effect against the deformation of the pipe is greater when the burial depth of the pipe decreases than when the burial depth increases. The experimental setup of model tests is given in Figure 2.1.

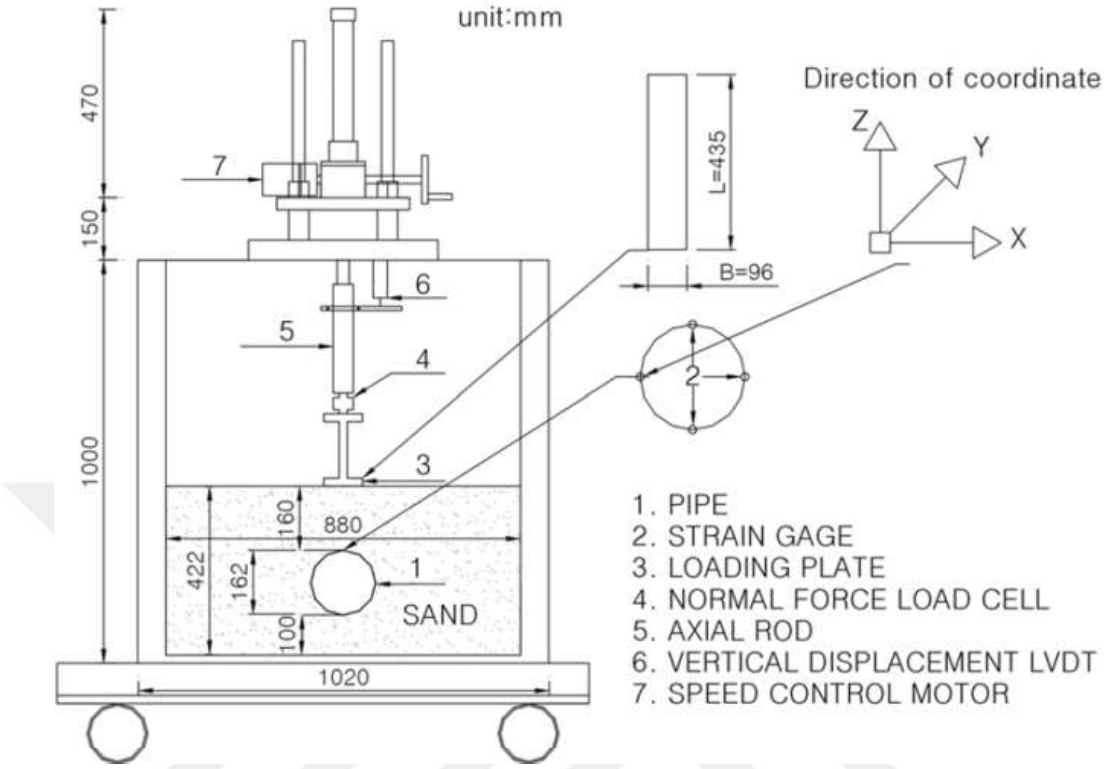


Figure 2.1. Experimental setup Won *et al.* (2004).

Terzi (2007) investigated the effect of backfill installation, backfill relative density and loading conditions on pipe deformation and pipe stability with HDPE flexible pipes of various diameters located on the 700x500x700mm sand box. In the experiments, deformations at pipe cross sections were measured by Linear Position Transducers and deformations were visualized by photogometric measurements. Different relative densities and various loading patterns were used in experiments to understand full behavior of the soil-pipe interaction under loading. Moreover, the test set up modeled in PLAXIS 2D and PLAXIS 3D TUNNEL program to compare experimental and numerical results.

Ahmed *et al.* (2015) conducted the experiments in order to investigate the distribution of contact pressure on buried pipes with a tactile sensor system and they modeled these experiments. They also investigated how geogrid reinforcement affects the contact pressure distribution on the pipe by placing geogrid reinforcement on the pipe. The backfill material used in the tests is a granular soil containing 77% sand and

33% gravel. The pipe used is a rigid PVC pipe. The results of the tests performed, showing the contact stresses at the crown of the pipe. The results of the experiments and models were consistent. As a result, it was seen that the contact stress on the pipe decreased after geogrid reinforcement and the effect of geogrid reinforcement increased gradually at higher loads.

Kawabata *et al.* (2003) performed two types of experiments, with and without geosynthetics and they used geogrid as geosynthetics for soil reinforcement. They used silica sand as backfill material and they prepared backfill material in the loosest condition possible. Results show that, with the geogrid reinforcement, vertical stress acting on the buried pipe decreased by 25%. The schematic representation of the cross section of test setup is shown in Figure 2.2.

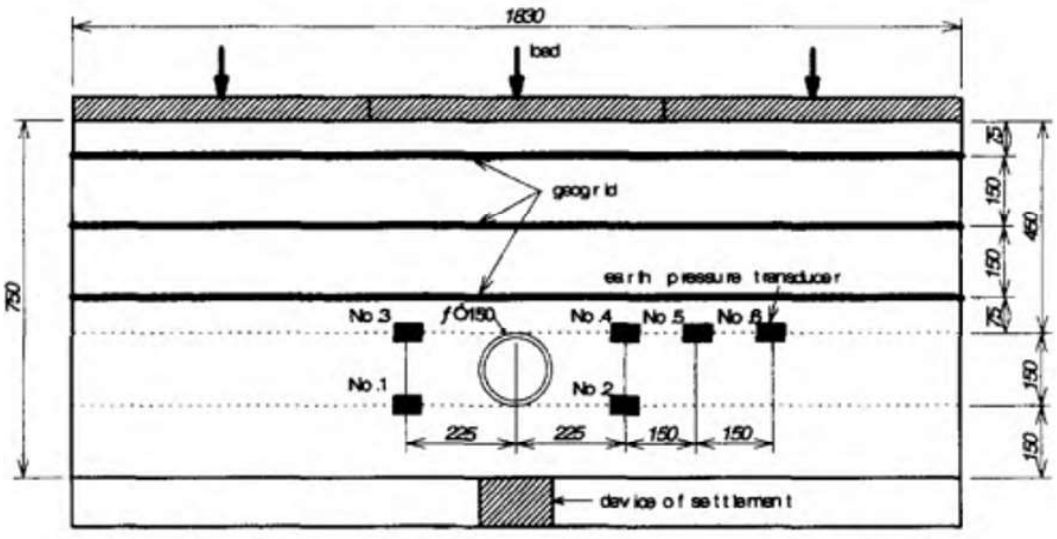


Figure 2.2. Schematic representation of model test setup Kawabata *et al.* (2003).

Pires and Palmeria (2017) performed laboratory experiments in order to investigate the type and orientation effects of geosynthetics on the pressure-settlement mechanism of the model footing and stress distribution around the pipe—the laboratory experiments conducted in a rigid metal tank filled by medium uniform sand with geogrid reinforcement. Every soil layer was prepared by using the sand rain technique to obtain uniform and desired relative density. To investigate the effects of geosynthet-

ics on the pressure-settlement mechanism of the model footing and stress distribution around the pipe, firstly, one model test was conducted as a reference model test with no reinforcement, then 9 model tests were conducted with three different geosynthetic orientations and type. Three orientation type can be seen in Figure 2.3, respectively. Tensile strength properties of different types of geogrids were 1.45kN/m, 12.0kN/m and 20.3kN/m and they were named R1, R2 and R3, respectively. As a result, the load-settlement curve of the model footing flattened with increasing the tensile strength of the geogrid. By using an enveloped type of orientation, minimum settlements were observed on the model footing and buried pipe. For the vertical crown stress, similar measurements were observed, shown in Figure 2.4. Minimum crown stress accomplished by using most stiff geogrid and envelope orientation.

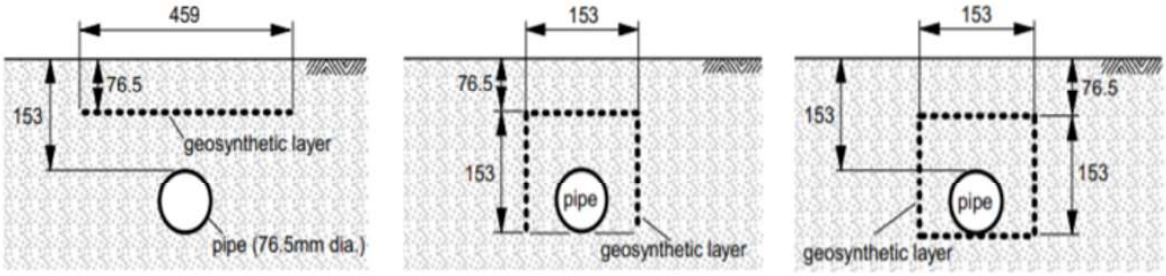


Figure 2.3. Three different orientation type: horizontal orientation (left), inverted orientation (middle) and enveloped orientation (right) Pires and Palmeria (2017).

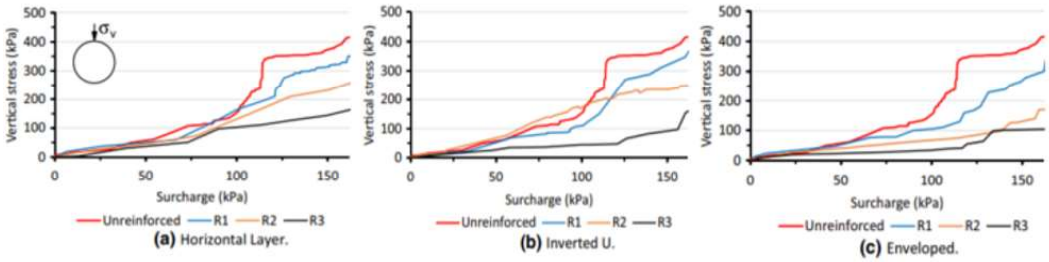


Figure 2.4. Vertical stress acting on the crown of the pipe-surcharge pressure acting on model footing with different geogrid types and orientations Pires and Palmeria (2017).

Chapman *et al.* (2007) studied the effect of the pipe installation method, the stiffness of the pipe and cover depth by applying increasing static surface load. The

used pipe was made of uPVC (unplasticed polyvinyl chloride) and two different pipes were used with external diameters of 250mm and 168mm. Leighton bazzard sand was used as a backfill material, which is a well graded sand. They determined that the load transferred to the buried pipe was significantly smaller for the well-placed dense sand. Furthermore, they found that cover/diameter ratios of 1 and 2 were almost identical. As a result, they observed that stiffer resisted a larger portion of the increasing static surface load at the same settlement level according to the less stiff pipe.

Laman and Bildik (2019) investigated the soil-pipe systems by conducting physical model tests considering the burial depth effect of the pipe and its horizontal distance from the model footing. During the experiments, they measured the load-settlement behavior of the system and the stress acting on the different locations of the pipe by placing strain gauges on the pipe. They found out that, with increasing burial depth for the same diameter pipes, the backfill soil's bearing capacity approximates the backfill's bearing capacity in the model test without the pipe. As the horizontal distance increases, the bearing capacity of the soil approximates the bearing capacity in the model test without the pipe. As a result, similar results were obtained with the horizontal distance comparison, with increasing distance of the buried pipe, backfill soil's bearing capacity approximates the without pipe condition. Furthermore, hoop stresses acting on the buried pipe decreased with the increasing burial depth and compression was obtained on the top and bottom surfaces of the pipe. With enough horizontal distance from the pipe, they recorded tension stresses on the top and bottom surfaces of the pipe. As horizontal distance increases, bottom and top hoop stresses reverse direction from compression to tension with proper burial depth. For the left and right side stresses, the left side hoop stress changes from compression to tension with increasing horizontal distance. In conclusion, with convenient horizontal distance, acting stresses on the four sides of the pipe are approximately zero.

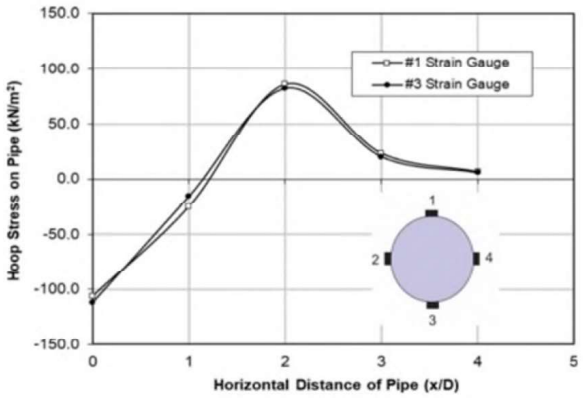


Figure 2.5. Hoop stresses on bottom and top of the pipe with horizontal distance from the model footing Bildik and Laman (2019).

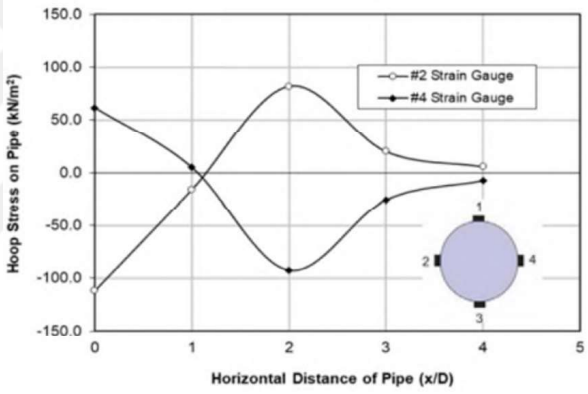


Figure 2.6. Hoop stresses on left and right side of the pipe with horizontal distance from the model footing Bildik and Laman (2019).

2.2.2. Dynamic Load Model Tests

Fattah *et al.* (2018) carried out various experiments by loading geocell-reinforced medium-dense sand to investigate the behavior of buried PVC pipes. The backfill used in the model tests consists of two layers, which are the subbase and the base. Geocell reinforcement was placed between the subbase and base. In order to investigate the effect of the geocell on the tension at the crown of the pipes and the vibration in the pipes, the pipes were exposed to repetitive loads with 0.5Hz, 1Hz and 2Hz frequencies with 0.5ton and 1ton loads. Furthermore, the experiment was modeled in 3D in order to investigate the effect of the geofoam on the pipe. They compared the reinforced soil

case with the unreinforced soil case in order to investigate the reinforcement effect. The results show that the geocell reinforcement reduced the tension in the crown by 41% and the shaking by 35%. The numerical model and the experimental study yielded consistent results and both show that the geocell plays a major role in the safety of the pipes.

Tafreshi and Khalaj (2011) conducted laboratory experiments with HDPE pipes under cyclic loading to simulate vehicle loads acting on buried pipes. Pipes with a diameter of 110 mm were used at different burial depths in the experiments. As can be seen in Figure 2.7, two types of soil were used in the experiments. Soil A (natural soil) was placed with the compaction method, while Soil B (ditch fill) was placed in the test case with a relative density of 42%, 57% and 72% by the raining method. They observed that a significant portion of the settlements and pipe deformations as a result of cyclic loading occurred as a result of the initial loading. They also concluded that the stress value in the pipe and the settlement on the ground surface decrease when the relative density increases, while the surface pressure increases and the stress value in the pipe decreases when the burial depth of the pipe increases.

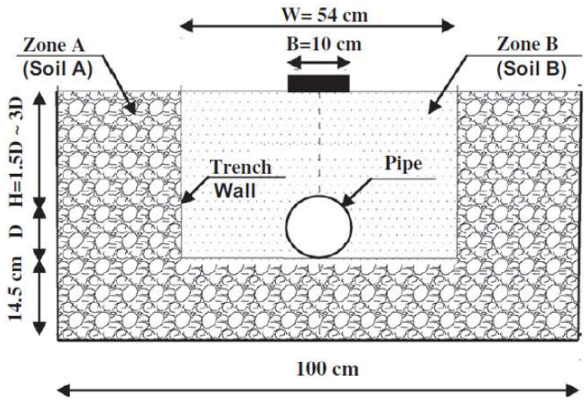


Figure 2.7. Schematic representation of model test setup Tafrahsi and Khalaj (2011).

Elshesheny *et al.* (2019) conducted laboratory experiments to investigate the behavior of polyethylene (HDPE) pipes in reinforced and unreinforced soils under increasing cyclic loading. The test box used in the experiments is 1500x1000x1000 mm in size. In the experiments, a geogrid with a modulus of elasticity of 300 MPa was

used for soil reinforcement. The experiments were carried out with cyclic loading in different phases. They chose the cyclic loading amplitude to be in the range of 20-30% of the monotonic loading. In the experiments, the effect of the embedment depth of the pipe and the number of reinforcements used in the system was investigated. The results obtained from the study are given below:

- Maximum settlement and strain occurred duringthe first loading phase and settlement and strain values decreased significantly in the later loading phases.
- Increasing the burial depth of the pipe led to a decrease of stress and deformation.
- While the reinforced case significantly reduced stress and deformations, it allowed the system to continue with the additional loading stages.
- In the single-reinforced condition, the settlement in the foundation decreased by 30% to 50%, while the deformation of the pipe and the stress values in the pipe were similarly decreased.
- It was observed that the stress measurement was consistently higher in the lower reinforcement layer than that recorded in the upper reinforcement layer, regardless of the burial depth and the load.

Mehrjardi *et al.* (2012) conducted the experiments schematically illustrated in the figure below to investigate the deformation restriction using geocell reinforcement in buried pipes. It is stated that the classification of the soils used according to the USCS classification system is SW. It is stated that the pipe used is PVC, its outer diameter is 160mm and its thickness is 4mm. While performing the experiments, three points, A, B and C, were determined and the soil stresses acting on these points were measured. As a result of the experiments, the soil surface settlement, soil stress and vertical displacement of the pipe were compared with and without reinforcement. As can be seen from the results shown, the ground surface settlement and the vertical displacement of the pipe can be reduced by 68% and 33% after the geocell is placed.

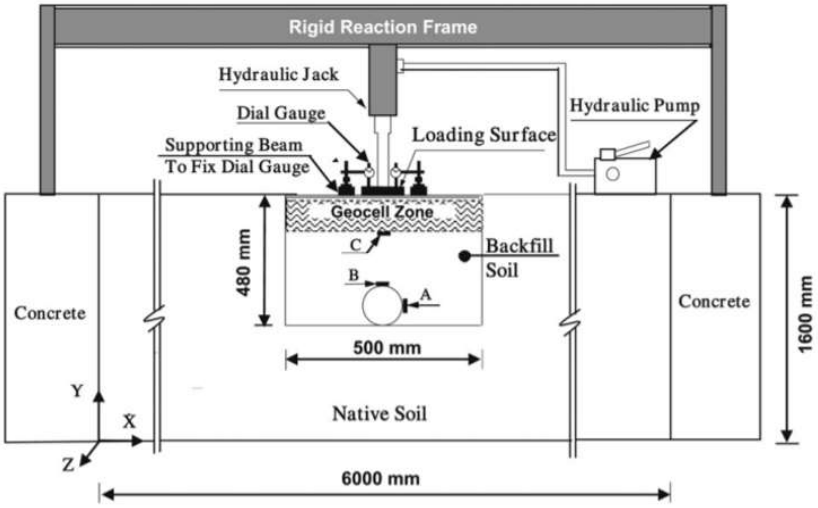


Figure 2.8. Schematic representation of model test setup Mehrjardi *et al.* (2012).

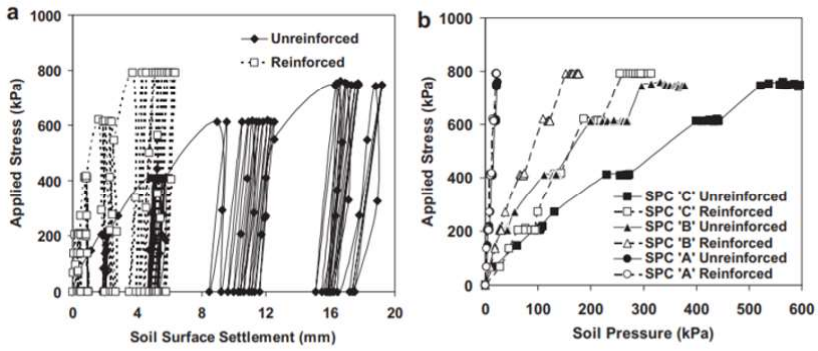


Figure 2.9. Soil surface settlement and soil pressure with applied stresses Mehrjardi *et al.* (2012).

2.3. Bearing Capacity Failure Mechanisms of Shallow Foundations

Shallow foundations transmit the load to the soil which creates deformations on the soil. If these loads are large enough, bearing capacity failure occurs depending on the type of soil, relative density of soil and the amount of the load. Studies have identified various bearing capacity failures, which are general shear failure, local shear failure and punching shear failure. (Coduto *et al.* 2016). Types of failure and failure surfaces are explained briefly in this section.

2.3.1. General Shear Failure

As mentioned in (Coduto *et al.* 2016), the most likely mode of failure for shallow foundations is general shear failure. It happens in moderately strong, incompressible soils. The load-displacement curve, which is shown in Figure 2.10, shows that the failure surface is well-defined and that failure happens both properly and quickly. Near the shallow foundation, the ground's surface shows a clearly defined bulge, as can be seen in Figure 2.11. Although there may be bulges on both sides of the footing, only one side ultimately fails and this failure is frequently followed by the rotation of the footing.

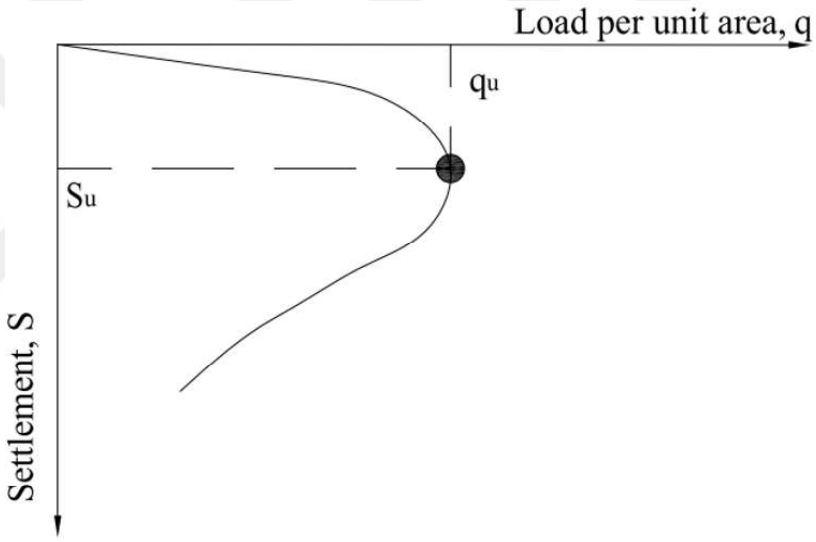


Figure 2.10. Typical load-displacement curve of general shear failure.

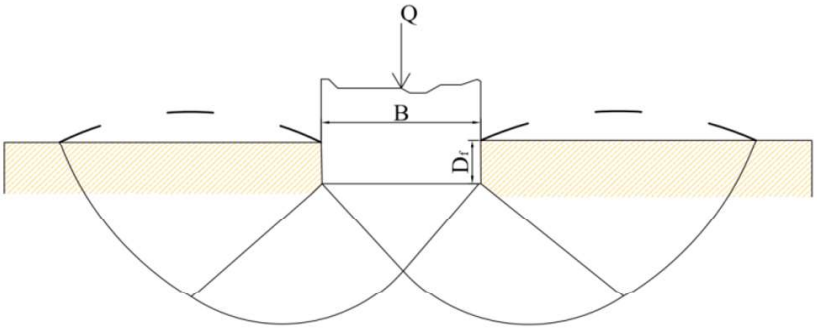


Figure 2.11. General shear failure.

2.3.2. Punching Shear Failure

As mentioned in (Coduto *et al.* 2016), Punching shear failure is the opposite extreme. This type of failure can occur in weak clays loaded under slow, draining conditions or in very loose sands, in a thin crust of strong soil underlain by very weak soil—such soil profiles' excessive compressibility results in significant settlements and poorly defined vertical shear surfaces. The load-settlement curve's depiction of an ever-increasing load, which is presented in Figure 2.12, shows that failure develops gradually and there is little to no bulging at the ground surface as can be seen in Figure 2.13.

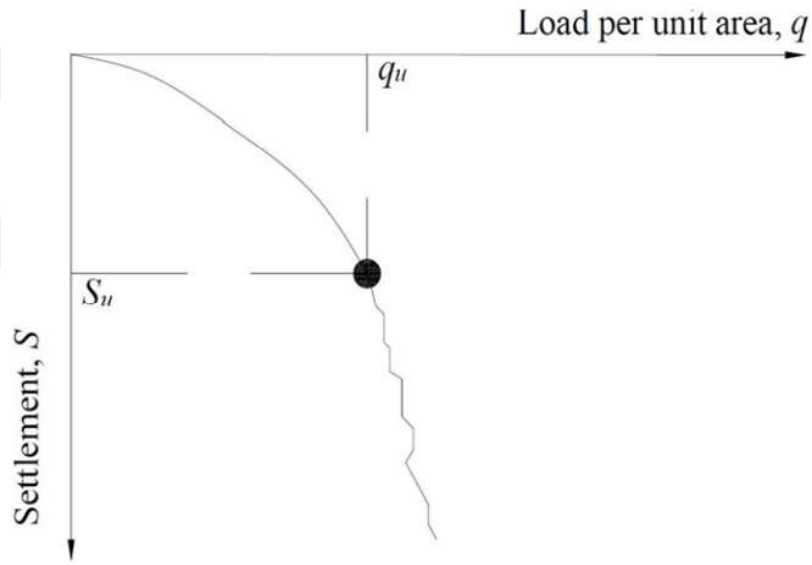


Figure 2.12. Typical load-displacement curve of punching shear failure.

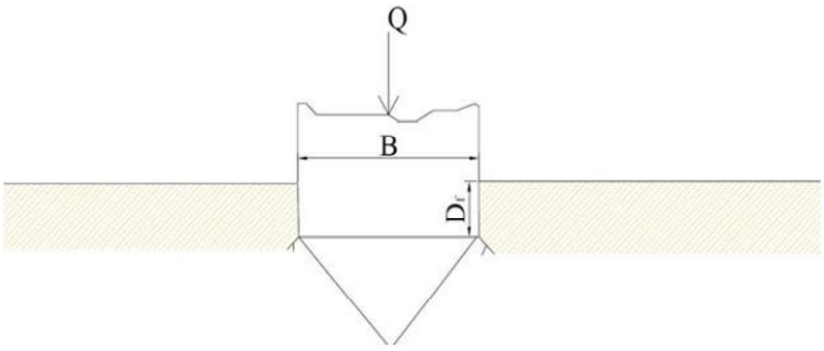


Figure 2.13. Punching shear failure.

2.3.3. Local Shear Failure

The local shear failure is the case between general shear failure and punching shear failure, as mentioned in (Coduto *et al.* 2016). Under the shallow foundation, the shear surfaces are very clean, as can be seen in Figure 2.15; nevertheless, they become indistinct very close to the ground surface. Small bulges are possible, but before a clear shear surface forms close to the ground, there must be a significant amount of settlement, maybe half the shallow foundation width. Even so, unlike in the general shear failure case, no rapid failure occurs. The footing keeps going deeper into the ground.

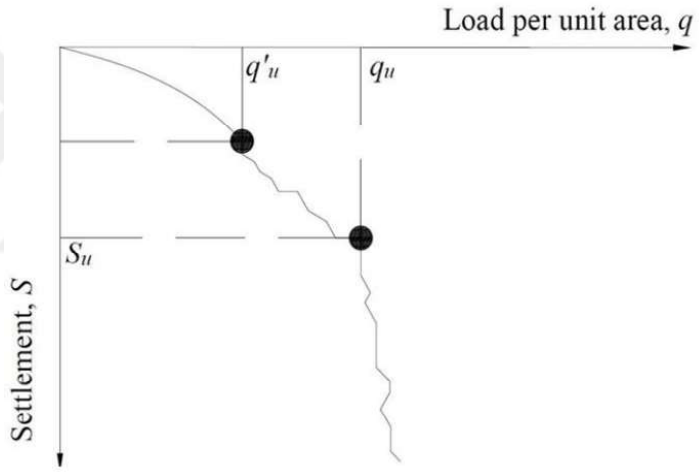


Figure 2.14. Typical load-displacement curve of local shear failure.

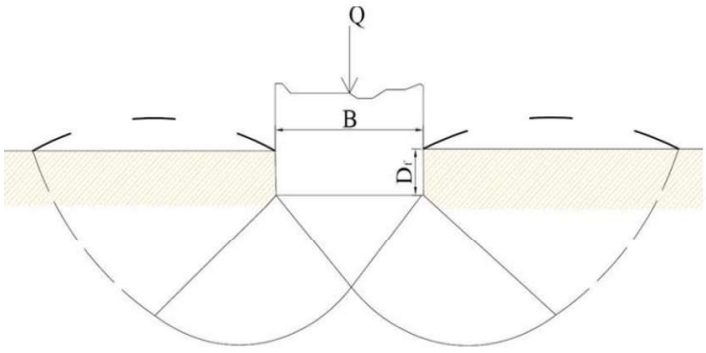


Figure 2.15. Local shear failure.

2.3.4. Failure Surfaces

Failure surface determination in the shallow foundation is crucial in order to predict the ultimate bearing capacity and estimate the affected zones from applied structural load. Terzaghi (1943) proposed one of the most important failure surface theories and his theory was based on the following assumptions;

- According to Terzaghi's (1943) definition of a shallow foundation, the depth of the foundation must be less or equal to the width of the foundation.
- The foundation's bottom is sufficiently rough to prevent any sliding between the shallow foundation and the soil.
- The soil beneath the shallow foundation is homogeneous.
- General shear failure is the controlling failure type.
- Soil does not experience any consolidation, which means that settlement of shallow foundation occurs only because of shearing and lateral movement.
- The shallow foundation is more stiff and rigid than the soil beneath the shallow foundation.
- The soil between the foundation depth (Df) and the surface is only for resisting a surcharge load.
- The applied load acting on shallow foundation has no eccentiricity and compressive.

Unter the given assumptions, failure surface that Terzaghi (1943) proposed is shown below in Figure 2.16.

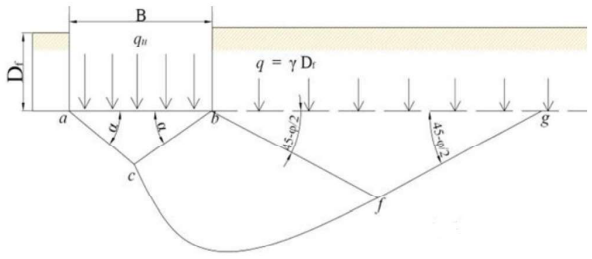


Figure 2.16. Failure surface for shallow foundations.

In Figure 2.16;

- B is the foundation width.
- Df is foundation depth.
- γ is the natural unit weight of the backfill soil
- ϕ is the friction angle of the backfill soil
- q_u is the surcharge pressure

As can be seen in Figure 2.16, failure surface can be divided into three main regions which are region abc, region bcf and region bfg.

- Region abc: This region located right below the shallow foundation and it is called triangular elastic zone with the inclination is equal to the friction angle of the backfill soil.
- Region bfg: This region named as Rankine Passive zone. Inclination of the Rankine Passive zone is stated as $\mp(45 - (\frac{\phi}{2}))$.
- Region bcf: This region named as Prandtl's radial shear zone, this zone, unlike others, contains a log spiral arc which shown above as cf.

2.4. Particle Image Velocimetry Method In Geotechnical Engineering

The particle image velocimetry measurement technique is defined by Grant (1997) as the simultaneous measurement of the velocity of a liquid across a region illuminated by a two-dimensional light plate. White *et al.* (2003) conducted studies to measure the movement of fine-grained soils by using the PIV method. Stanier *et al.* (2015) developed this technique and stated that it provides a tenfold improvement in particle movement measurements. Duan *et al.* (2019) state that the particle image velocity measurement technique can be used in measuring soil deformation problems such as slope problems and piled systems.

Stanier *et al.* (2015) developed the geoPIV_RG program, which is a MATLAB-based analysis method. This program divides a reference photograph taken at the start of the experiment into meshes. The program works by calculating the distances between each mesh of the reference photo and the next photo. Mesh sizes are determined by the user. Before starting the geoPIV_RG analysis, a region of interest must be established using the reference photo. Analysis is done in this region of interest.

As the mesh size increases, the resolution decreases while the computation time decreases. In this case, attention should be paid to the selection of the appropriate mesh size. In the following section, studies on the use of particle image velocity measurement technique in geotechnical engineering are explained in this section.

White *et al.* (2003) used PIV, a deformation measurement system developed based on grain image velocimetry, in geotechnical tests. They investigated the theory and performance of the improved strain measurement system. It was emphasized in the studies that the movement of a ground mesh was measured with a high accuracy using PIV. They mentioned that displacement vectors are converted from picture space to object space by photogrammetric conversion.

First, they illustrated the use of images in PIV analysis with the diagram given in Figure 2.17. As can be seen in Figure 2.17, they emphasized that the images are divided into meshes and the displacement vectors of the meshes are calculated separately. The movements of 480 points with meshes of 32x32 pixels were examined using the PIV method. Movement and position accuracy in the meshes are explained by the diagram shown in Figure 2.18 below. By analyzing the results, it was emphasized that PIV was more effective than the image-tracking analysis systems used before.

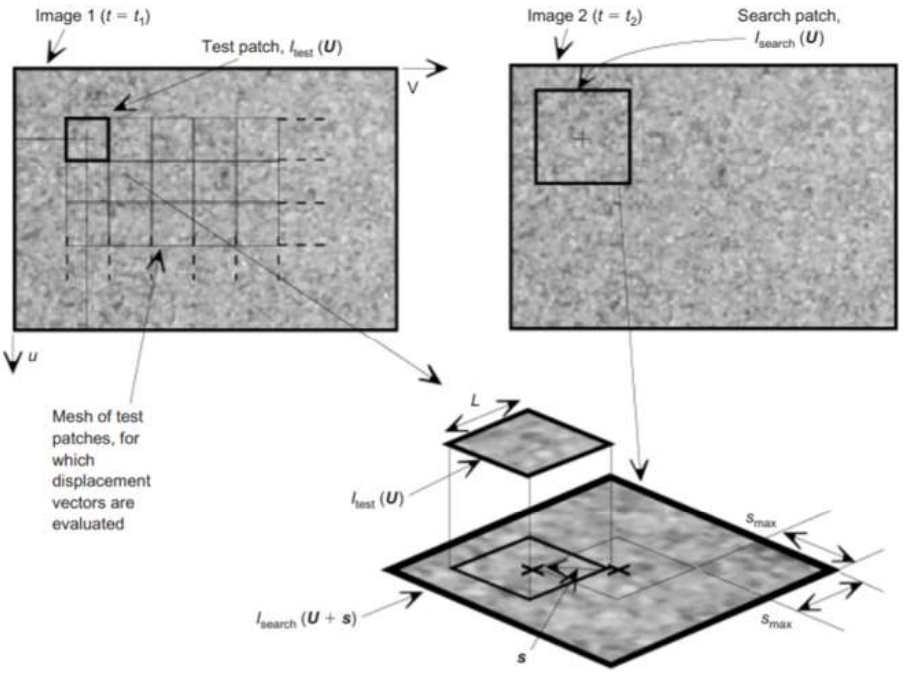


Figure 2.17. Usage of images in PIV method White *et al.* (2003).

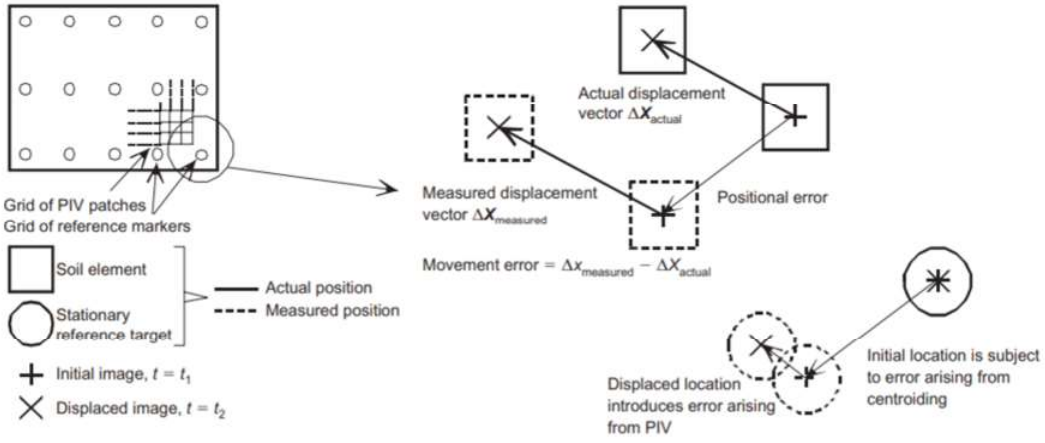


Figure 2.18. Movement accuracy diagram White *et al.* (2003).

Wu *et al.* (2021) performed model experiments at different burial depths to measure the response of a rigid pipe buried in sand when subjected to vertical motion. Model experiments in loose, medium-dense and very dense sand were analyzed with the help of the PIV technique. Displacement vectors coming from PIV analysis are obtained succesfully.

Marshall *et al.* (2010) conducted centrifugal tests on sandy soil to investigate tunnel constructions passing under buried pipes and the relationship between soil deformations and pipe bending behavior. They summarized the problem in Figure 2.19 given below.

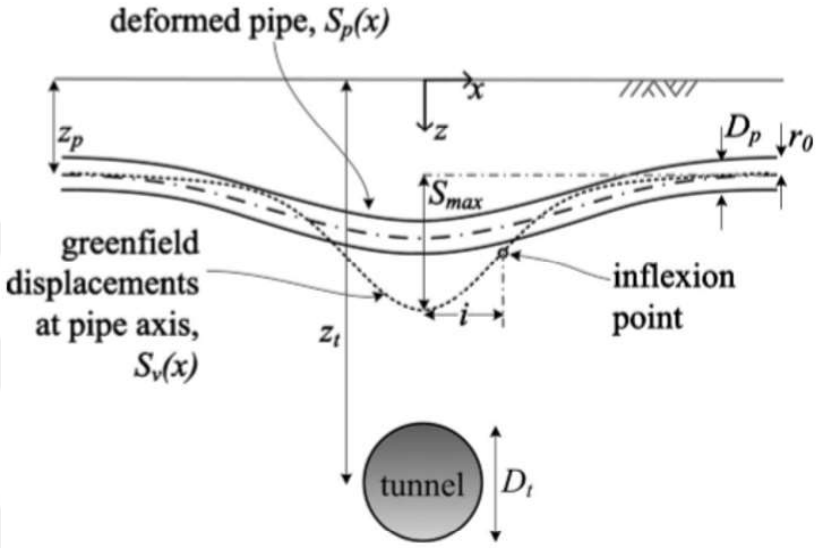


Figure 2.19. Schematic represantation of tunnel under the buried pipe Marshall *et al.* (2010).

In the studies, three different pipe types were used. The elastic modulus and geometric properties of the pipes were different from each other. Soil-pipe interaction was observed by PIV analyses. With the PIV analysis, the settlement results of the pipes were found according to the distance from the center of the tunnel. These results are shown in Figure 2.20. In the greenfield part of the results, the results are given for the cases where there is no pipe. According to the results obtained from the experiments, it has been understood that the behavior of the soil will not be completely elastic in the relationship between the pipe and the ground. Local changes in the stresses of the soil around the pipe will noticeably change the stiffness of the soil.

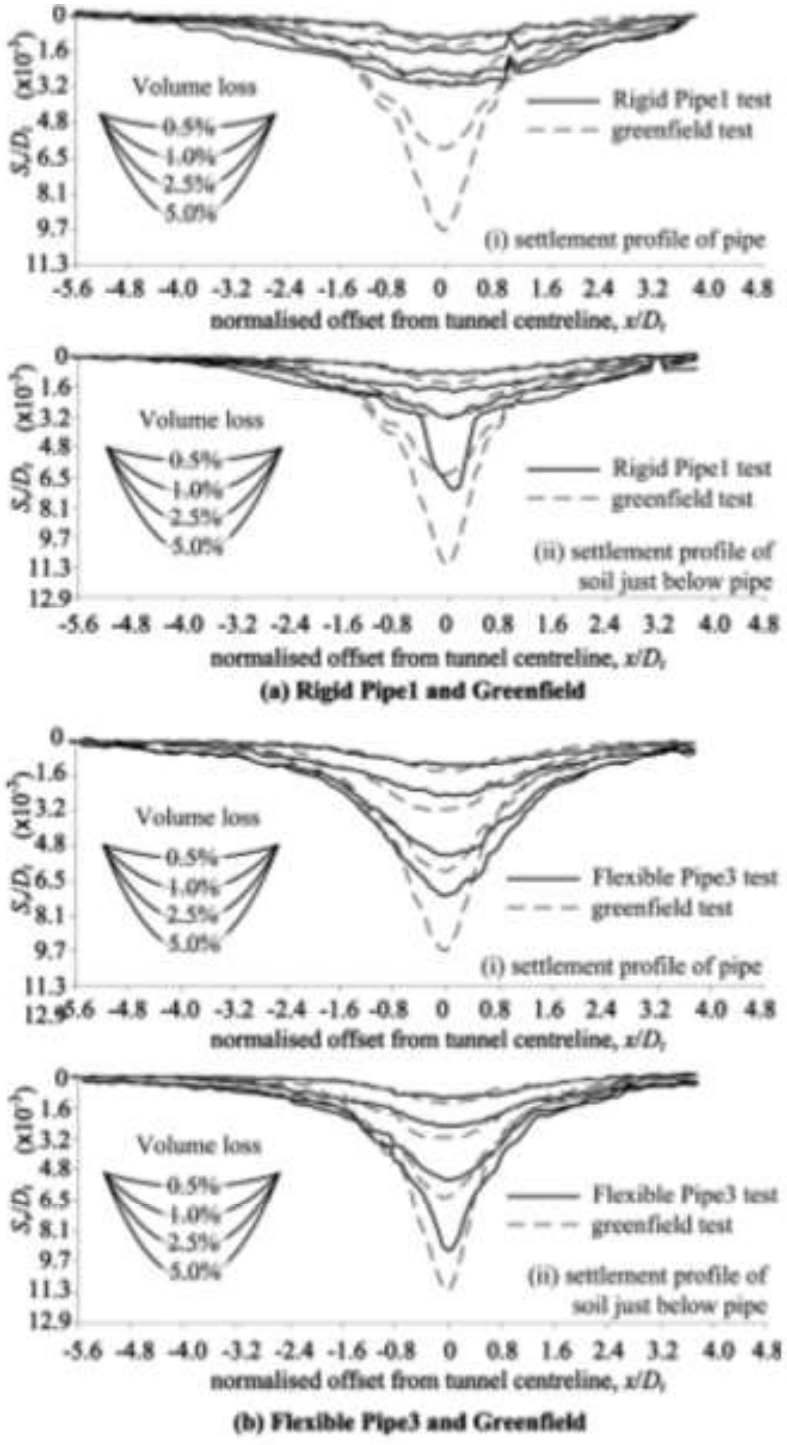


Figure 2.20. Settlement profile of pipe and settlement profile of soil just below the pipe obtained from PIV analysis for two pipe types Marshall *et al.* (2010).

Chen *et al.* (2019) conducted numerical and physical experiments in dense sand to examine the effect of pile placement on the deformation of pile groups. In the test, the PIV method was used to detect deformations. As a result of the tests, it was observed

that the bearing capacity of the piles increased and they had less displacement when the piles were built close to each other.

Wang *et al.* (2021) experimentally investigated the behavior of buried pipes under load. In the study, FBG (fiber bragg gating) sensors were used to determine the behavior of the pipe under load. At the same time, particle image velocimetry measurement technique was used to observe the shear-strain behaviors that will occur on the soil during the experiment. Wang *et al.* (2021) experimental setup is given in Figure 2.21. Measurements with FBG sensors have shown that the deformation behavior of the pipe under load depends on the burial depth. As a result of their studies, they determined that the failure surfaces can be formed in three ways: logarithmic spiral, linear and logarithmic. It has been observed that the fracture pattern that will occur is directly related to the pipe burial depth and load width. The results showed that the fracture surface of the pipe changed from a logarithmic spiral to a linear or logarithmic shape as the embedding depth of the pipe increased.

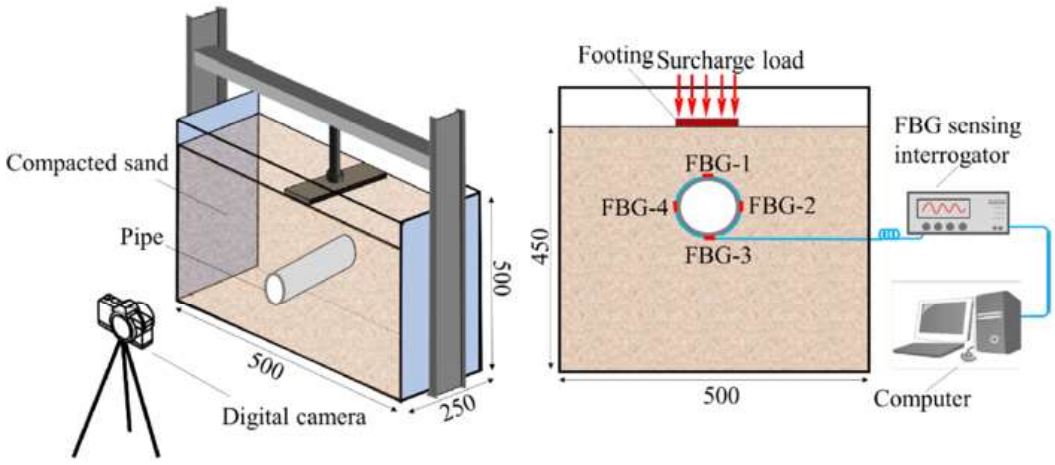


Figure 2.21. Schematic representation of model test setup Wang *et al.* (2021).

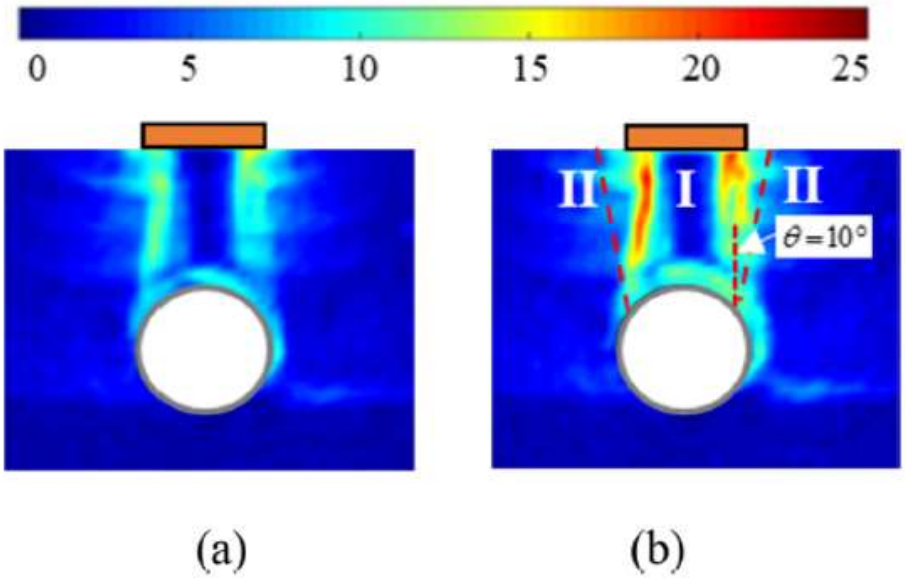


Figure 2.22. Shear strain contours under different burail depth obtained from PIV Wang *et al.* (2021).

3. EXPERIMENTAL METHODOLOGY

3.1. Physical Model Test Setup

3.1.1. Test Box

All model tests were conducted in a rigid text box with the dimensions of 100cm x 50cm x 60cm (length x width x depth). The test box is made of a steel frame system and has plexiglass panels that are 10 mm thick on its front and back faces in order to capture images while the experiments are being conducted. To determine whether the expected relative density was achieved while the backfill was being poured into the box, horizontal lines were drawn with 5cm intervals on the rear plexiglass to be able to use the weight-volume relationship. The test box used in the model tests is shown in Figure 3.1.

3.1.2. Model Footing

A strip steel model footing with the dimensions of 50cm x 10cm x 3cm (length x width x depth) was used in all experiments, which can be seen in Figure 3.2. Steel marbles are placed into circular housings on the model footing to ensure full contact with the hexagonal loading plate, which leads to uniform load distribution. Furthermore, a spring system was installed on the rear and front sides of the model footing to avoid the motion of the sand particles towards between the plexiglass panels and the model footing. This spring system, which sweeps the sand between the plexiglass and model footing while the footing settles, was produced to acquire valid PIV analysis since PIV analysis badly affects if there is a sand motion between the model footing and the front face of the plexiglass. The spring system and location of the spring system on the model footing are represented in Figure 3.3 and Figure 3.4, respectively.

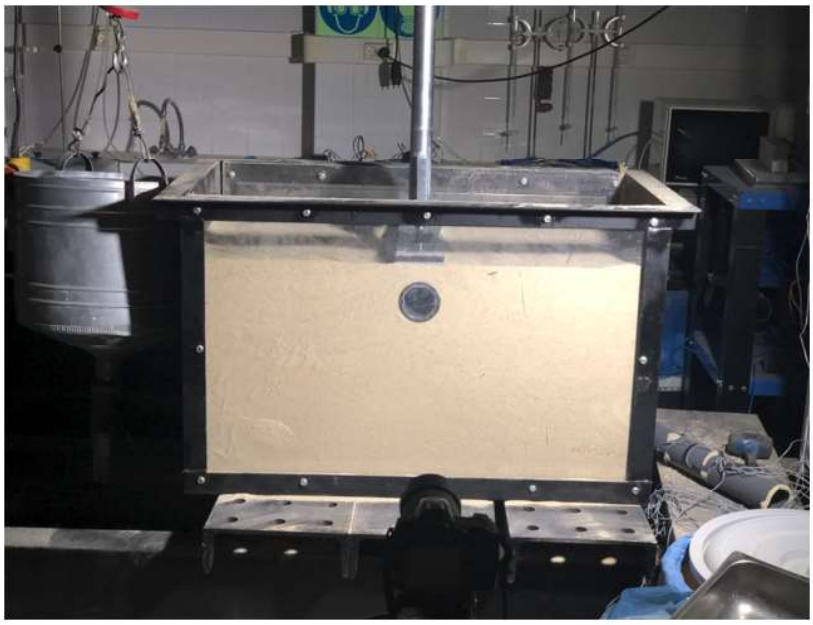


Figure 3.1. Test box.

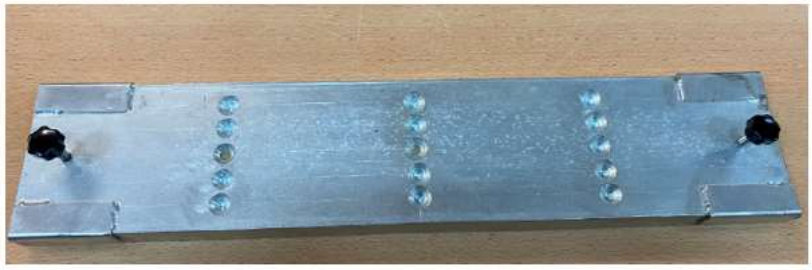


Figure 3.2. Strip steel model footing used in the model tests.

The model footing has three lines of 1.5 cm diameter grooves, with every line having five grooves. Three steel marbles were located in the third groove of every line. Other grooves were carved in order to carry out eccentrically loaded experiments if desired. Placement of the steel marbles shown in Figure 3.5.

3.1.3. Linear Variable Differential Transformer (LVDT) Transducer

To determine the displacement on the footing caused by vertical loading, the LVDT transducer was utilized in the model tests produced by the Yordam Test and Measurement firm. The LVDT transducer used in the experiments had a stroke length of 150.00mm, which means it was capable of measuring displacement up to 150.00mm.

The stress-displacement curves given in the results section were formed by using displacement values of the footing obtained from the LVDT transducer. During the experiments, the LVDT transducer was located behind the hexagonal loading plate, near the rear plexiglass. LVDT transducer can be seen in Figure 3.6.



Figure 3.3. Spring system used in the model tests.



Figure 3.4. Location of the spring system on model footing.

3.1.4. Load Cells

Three different S type load cells were used to measure the loads acting on the model footing in the model tests. The 500kg capacity load cell was produced by Yordam Test and Measurement Firm, 1 tonne and 2 tonnes capacity load cells were produced by CAS firm. The 500kg capacity load cell on the test set up can be seen in Figure 3.7 and load cell specifications are given in Table 3.1.



Figure 3.5. Placement of the steel marbles.

Calibration of load cells was accomplished by placing known weights on the loading system and editing required coefficients to obtain accurate readings using LabView software, as described in the following sections.

Table 3.1. Load cell specifications.

Property	**500kg Load Cell**	**1t on Load Cell**	**2ton Load Cell**
Precison Class	C3	C3	C3
Capacity (kg)	500	2000	2000
Input Resistonce (Ω)	385±10	400±3.5	400±3.5
Out Resistance (Ω)	350±3	350±3.5	350±3.5
Isolation Resistonce ($M\Omega$)	⩾5000	⩾2000	⩾2000
Compensated Temperature Interval (C^o)	-10∼+40	-10∼+40	-10∼+40
Working Temperature (C^o)	-35∼+65	-30∼+80	-30∼+80
Recommended Excitation (V(DC))	5-12	10	10
Maximum Excitation (V(DC))	15	15	15
Overloading Capacitiy (%)	150	150	150



Figure 3.6. LVDT transducers used in the model tests.



Figure 3.7. 500kg capacity S-Type Load Cell used in the model tests.

3.1.5. Strain Gauges

During the experiments, the GFLA-6-50 model Tokyo Sokki brand, suitable for plastic surface strain gauges, was used to measure pipe strains. Strain gauges were glued to the pipes by an adhesive product, which was produced specifically for strain gauges manufactured by Tokyo Sokki. S-B-type protective tape was used in order to protect and get accurate measurement values from strain gauges. The strain gauge, adhesive product and protective tape can be seen in Figure 3.8, Figure 3.9 and Figure 3.10, respectively.



Figure 3.8. GFLA-6-50 model strain gauge used in the model tests.

LabView software was used to calibrate the strain gauges. Strain gauge properties were entered manually into the software, which can be seen in Table 3.2. Strain values were used to calculate stresses acting on the chosen locations of the pipes by using Hooke's Law. During the model tests, it was assumed that pipes undergo elastic deformations and with using strain data and pipe stiffness, stresses on the pipes were calculated.



Figure 3.9. Adhesive product used in the model tests.



Figure 3.10. Tape used in the model tests.

3.1.6. Pipe Properties

In the scope of this thesis, pipe-soil interaction was examined by burying a single pipe in different locations under the model foundation; therefore, the selection of the pipe type was critical. To measure deformations accurately, strain gauges must stuck

to the pipe properly and the pipe must obey Hooke's Law; thus, PVC pipes produced by the Pilsa brand were used during the model tests.The model pipe used in the model tests and the specifications of the pipes can be seen in Figure 3.11 and Table 3.2, respectively.

Table 3.2. Specifications of the strain gauge used in the model tests.

Property	**Value**
Gauge Factor	2.09±1%
Gauge Resistance (Ω)	120.8±0.5
Gauge Length (m)	6
Lead Wire	10/0.124m
Transverse Sensitivity	1.00%
Temperature Compensation ($^oC^{-1}$)	50x10^{-6}



Figure 3.11. Model pipe used in the model tests.

Table 3.3. Specifications of the pipe used in the model tests.

Property	**Value**
Pipe Diameter (mm)	75
Pipe Wall Thickness (mm)	2.2
Modulus of Elasticity (MPA)	3000
Thermal Expansion Coefficient ($^oK^{-1}$)	0.7 x 10^{-4}
Specific Heat (J/g^{o}K)	1.0

3.1.7. Data Acquisition System

Acting load on the footing, footing displacement and pipe strains were recorded using a data logging chassis, data logger module and data transfer module produced by National Instruments. Due to these recordings, analyses were made. Digital data loggers work by measuring resistance variations during experiments and recording them using computer software.

In the experiments, the S-type load cell was wired to a NI-994 terminal adapter with full-bridge configuration and the RJ-50 cable was connected to an NI-9237 bridge module. Finally, the module was attached to the NI-cDAQ-9179 chassis. Product specifications, excitation values and calibration constants were entered into LabView software manually. The bridge module, the terminal adaptor and the chassis with the bridge module attached are given in Figure 3.12, Figure 3.13 and Figure 3.14 respectively.

LVDT transducers were wired to the main chassis using the NI-9472 bridge module without using any terminal adapter. NI-9472 bridge module was attached to the NI-Cdaq-9179 chassis. In order to connect strain gauge, the same procedure with the load cell was followed but instead of a full-bridge connection, a quarter-bridge configuration was used, following the instructions provided by the strain gauge supplier.



Figure 3.12. NI-9237 bridge module.



Figure 3.13. NI-9949 terminal adapter.

3.1.8. LabView Software

LabView is a data recording and monitoring software produced by National Instruments. Three separate LabView programs were created with the support of a National Instrument supervisor to record and monitor applied load, displacement of the model footing and strain values of the pipe during the model tests. Due to the created LabView programs, the system's behavior was understood and any possible problems were detected while model tests occurred. At the end of model tests, recorded data were exported to the Excel spreadsheets, filtered and results were analyzed. An example of the algorithm flow of the used LabView program is given in Figure 3.15.

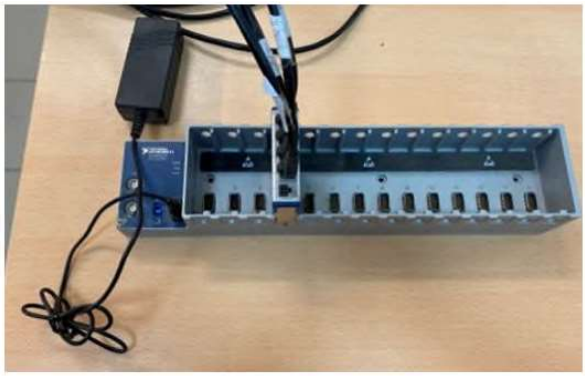


Figure 3.14. NI-cDAQ-9179 chassis with NI-9237 bridge module attached.

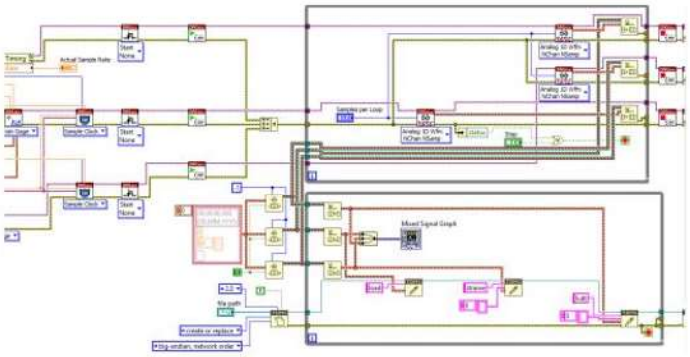


Figure 3.15. Algorithm flow in labView.

3.1.9. PIV Analysis

In the scope of this thesis, GEOPIV_RG MATLAB module developed by Stainer *et al.* (2015) was used. It is possible to exclude pipe from the region of interest (RoI) by defining pipe diameter in terms of pixel as a control point. In this study, the buried pipe was excluded from the RoI since the absence of the pipe in the analysis prevents observing displacement contours around the buried pipe. Moreover, the inside of the pipe creates immobile mesh as a void and the module cannot analyze the constant mesh; thus, analyses without defining RoI result in inaccurate displacement contours.

In PIV analysis, the leap frog analysis mode of the module was used rather than the control point analysis since the leap frog analysis is faster. Nevertheless, the leap frog analysis computes values in terms of pixels. In order to evade it, researchers created a unique MATLAB function to scale pixels into millimeters. The function scales the RoI to its original size and calculates displacements correspondingly due to having a constant (the plexiglass area) RoI. Another MATLAB function was created to scale the vectorial displacement fields. The PIV data were scaled in relation to vertical displacement on the assumption that the maximum vertical displacement at each subsequent photograph was 2 mm. The optimal mesh size used in the PIV analysis was determined as 50 x 50 pixels by trial and error. This mesh size led to understanding displacement mechanisms accurately while resulting in lower computation time, which can be seen in Figure 3.16. Meshed RoI can be seen in Figure 3.16.

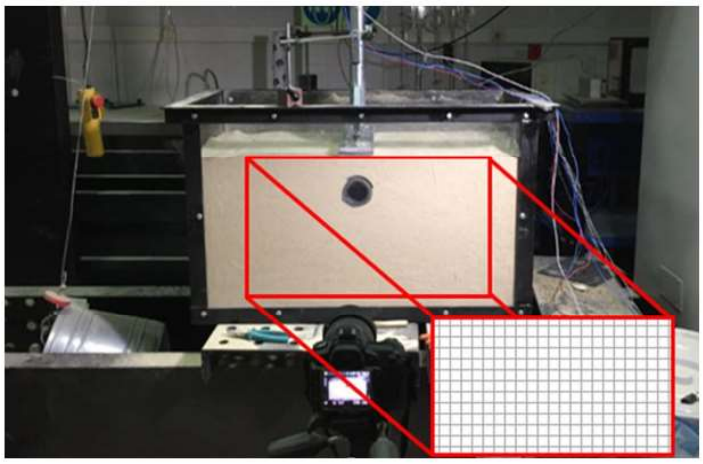


Figure 3.16. Meshed area (RoI).

3.1.10. Camera

During the experiments, photos were taken with a Nikon D90 camera. To analyze accurately, the camera was placed at a constant distance from the text box. The camera used in the model tests represented in Figure 3.17.



Figure 3.17. The camera used in the model tests.

3.2. Properties of the Backfill Material

In the experiments, the sand gathered from Çerkezköy, Tekirdağ was used. Çerkezköy sand was used by Oner (2020) and its index and strength properties were determined

by laboratory tests conducted by Oner (2020). The conducted tests are sieve analysis, maximum and minimum void ratio, specific gravity, microscopic tests to examine sand particle mineralogy and triaxial tests. All of the tests were done by following ASTM standards. Granulometric curve, index properties and strenght properties of Çerkezköy Sand are given in Figure 3.18, Table 3.4 and Table 3.5, respectively.

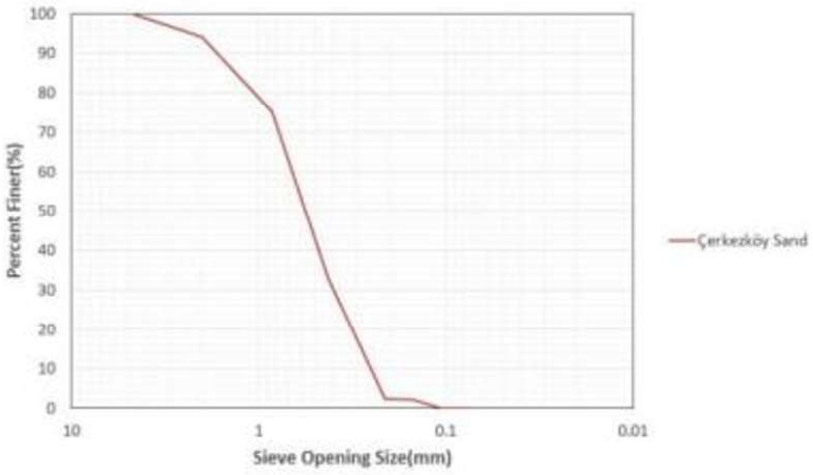


Figure 3.18. Granulometric curve.

Table 3.4. Index properties.

Property	**Value**
Classification	SP
Median Particle Size (D_{50})	0.64
Coefficient of Uniformity (C_u)	2.37
Coefficient of Curvature (C_c)	0.93
Specific Gravity (G_s)	2.62
Maximum Void Ration (e_{max})	0.83
Minimum Void Ratio (e_{min})	0.5
Average Sphericity (S_{ave})	0.56
Average Roundness (R_{ave})	0.749

Table 3.5. Strength properties.

Property	**Value**
ϕc^T	33.04
r_{tx}	0.59
r_{ps}	0.93
α_ψ	-0.03
m_ψ	0.302
E_{50ave}	16.3

In Table 3.5;

- ϕc^T is the critical state friction angle determined by triaxial tests.
- r_{tx} is the dilatancy effect parameter on friction for axisymmetric conditions.
- r_{ps} is the dilatancy effect parameter on friction for plain-strain conditions.
- α_ψ a stress based material constant (Cinicoglu and Abadkon, 2015).
- m_ψ a density based material constant (Cinicoglu and Abadkon, 2015).

3.3. Required Mass Calculation for Predetermined Relative Density

Relative density of sands calculated with using maximum void ratio of used sand (e_{max}), minimum void ratio of used sand (e_{min}) and current state void ratio of used sand (e). The needed void ratio (e) of sand at the desired relative density can be determined because the relative density values for used sands in this study are predetermined and the minimum and maximum void ratios are known from Table 3.6. After determining the necessary void ratio, the dry density value is calculated by using soil's phase relations.

After the dry density of the backfill at the target relative density calculation, the required mass per layer can be obtained by multiplying the test box volume with the density value and dividing it by ten. In order to expedite the process, a spreadsheet was created. For the trials involving buried pipe, pipe volume was deducted from the

total volume. The required mass calculation for the tests with buried pipe was done by subtracting the pipe volume from the volume of the test box and then multiplying the found volume value with the density value. In order to expedite the process of mass calculation, a spreadsheet was created. Table 3.6 lists the required mass values for each layer without and with the pipe, designated as Mp and M, respectively, at the desired relative densities.

Table 3.6. Required mass for every layer at three different relative densities.

Relative Density (%)	$\gamma_d(kg/m^3)$	*M(kg)*	*Mp(kg)*
35	33.04	38.79	38.45
50	0.59	39.95	39.60
65	0.93	41.17	40.81

3.4. Procedure of the Model Tests

In every model test, following procedure was chronologically conducted.

- In the buried pipe model tests, firstly the strain gauges were placed. To place strain gauges correcty, the surface of the pipe was cleaned with using alcahol, then strain gauge was glued with a special glue, can be seen in Figure 3.19 and Figure 3.20, respectively.
- After placement of the strain gauge, SB tape is attached around the strain gauges to protect it from outside effects. Finally, numbered papers are attached to SB tape in order to understand which strain data came from which strain gauge is shown in Figure 3.21.



Figure 3.19. Cleaned pipe.



Figure 3.20. Placement of strain gauge.

- Three different relative densities were used in the model tests; therefore, the required mass, which was calculated by using index properties, was changed throughout some of the tests.
- In order to compact Çerkezköy Sand accurately, Çerkezköy Sand was placed in 10 layers, which were 5cm thick. Layers were separated by lines drawn on the rier face of the test box. For every layer, 10% of the total required mass was poured

carefully and compacted using a drill with a flat end. A drill with a flat end can be seen in Figure 3.22.

- The pipe with attached strain gauges was placed in the compacted backfill when the appropriate burial depth had been attained.
- The pipe was precisely horizontally leveled using a water gage and any necessary adjustments were made.
- The remaining backfill was poured until it reached the top of the final layer. Then, a spatula was used to flatten the ground and a water gauge was used to control the footing's leveling, as shown in Figure 3.23.
- The spring system was activated using the screws shown in Figure 3.24.
- Marbles were placed on the model footing.
- LVDT transducer was positioned on the footing's edge and the camera was positioned in front of the test box at a fixed distance.
- To check for any measurement issues, the LabView software was controlled.
- Two spotlights were placed towards to the text box and turned on to illiminate the text box. Laboratory lights were turned out.
- The hexagonal loading plate was lowered until it came into contact with the marbles.
- First photo was taken as reference.
- At a continuous pace of 10mm/min, loading starts. A 2mm settlement results in a photo being taken every 12 seconds. The footing was generally loaded up to a displacement of 20mm. Test control panel shown in Figure 3.25.
- Using LabView software, load-displacement and strain values were recorded can be seen in Figure 3.26.
- Finally, test and image data were transmitted to personal computers for analysis in Excel and GeoPIV_RG.

Test setup before the loading process and side view illustration of model test setup can be seen in Figure 3.27 and Figure 3.28 respectively.



Figure 3.21. Numbered papers and SB tape attached on strain gauge.

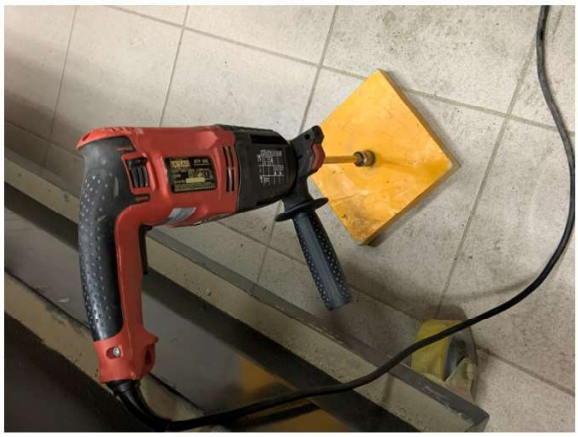


Figure 3.22. Drill with a flat end.



Figure 3.23. Water gauge.

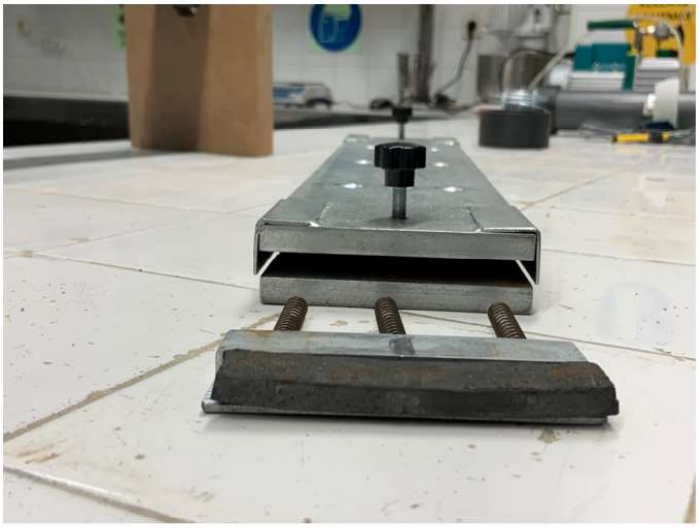


Figure 3.24. Spring system.



Figure 3.25. Test control panel.

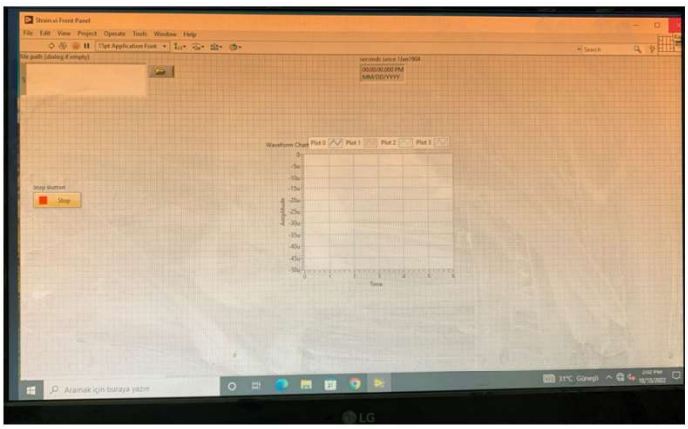


Figure 3.26. LabView software strain front panel.

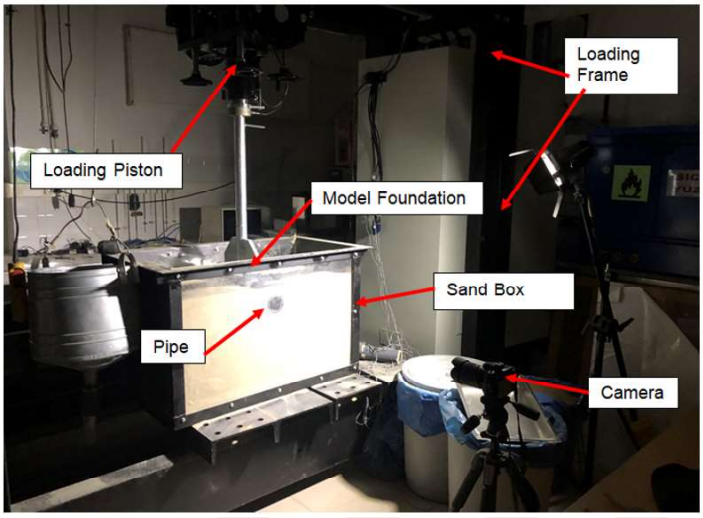


Figure 3.27. Test setup before the experiment.

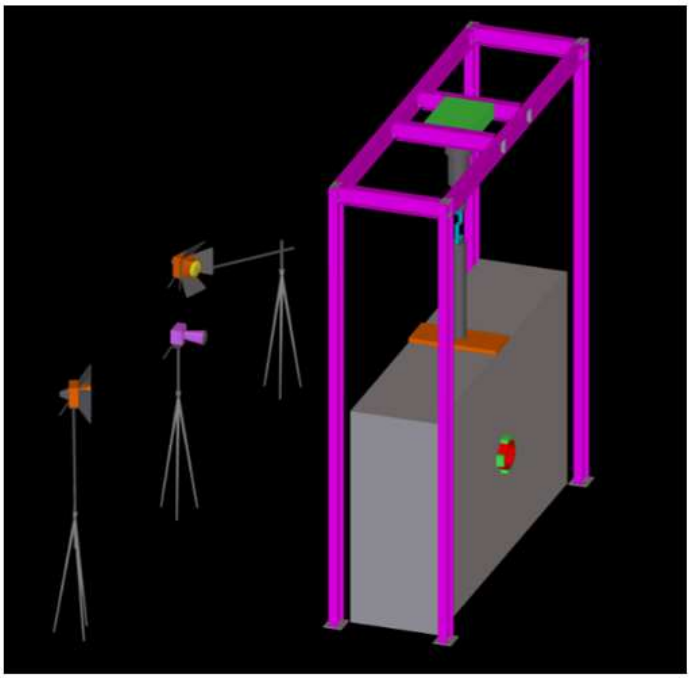


Figure 3.28. Side view illustration of model test setup.

4. RESULTS

Schematic representation of investigated parameters in model tests can be seen in Figure 4.1.

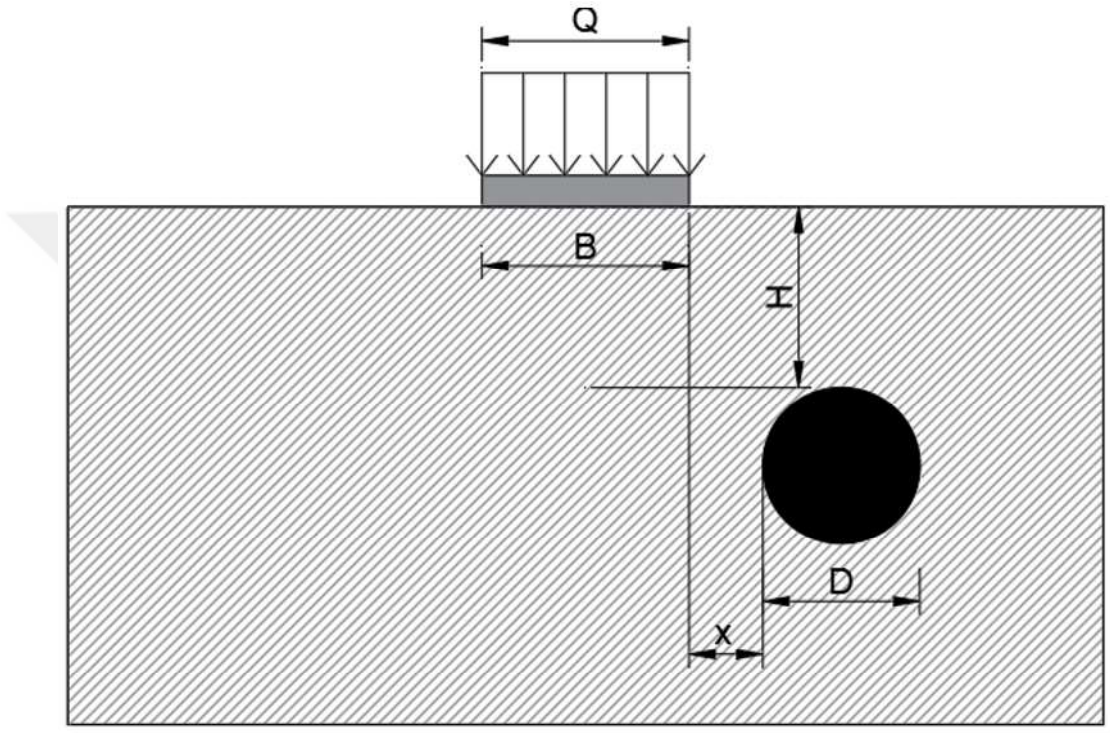


Figure 4.1. Investigated parameters.

In Figure 4.1;

- Q is the load which applied on model footing
- D is the diameter of the buried pipe
- B is the width of footing
- H is the vertical distance between crest of the pipe and the footing bottom
- x is the horizantal distance between outer left side of the pipe and right end of the model footing.

Table 4.1. Model test program.

Model Test No.	D_r (%)	**H/B**	**x/B**
T1	35	-	-
T2	35	0.75	-
T3	35	1.5	-
T4	50	-	-
T5	50	0.75	-
T6	50	1.5	-
T7	65	-	-
T8	65	0.75	-
T9	65	1.5	-
T10	35	0.75	0
T11	35	0.75	0.75
T12	35	0.75	1.5
T13	65	0.75	0
T14	65	0.75	0.75
T15	65	0.75	1.5
T16	65	1.5	0
T17	65	1.5	0.75
T18	65	1.5	1.5

The test program is shown in Table 4.1, in Table 4.1;

- D_r is the relative density of Çerkezköy Sand
- H/B is the ratio of distance between crest of the buried pipe and bottom of the model footing with respect to model footing width
- x/B is the ratio of horizantal distance between outer left side of the pipe and right end of the model footing with respect to model footing width

The model tests included three different relative density values in order to investigate the behavior of the soil-buried pipe system in loose, medium-dense and dense relative density classifications, which can be seen in Table 4.2, note that this classification can be subjective. Furthermore, model tests were conducted with varying buried pipe locations both horizontally and vertically to see the effect of buried pipe positions. T1, T4 and T7 are the reference model tests conducted without a pipe to compare only soil behavior with different relative densities.

Settlement of the model footing equal to 10% of the model footing width is defined as the ultimate state due to there being no specific bearing capacity failure criteria in cohesionless-sandy backfills. The width of the model footing is 10cm; therefore, a 1cm settlement of model footing is accepted as a failure. Another reason for this failure criteria was chosen: in some model tests, sand intrusion towards the buried pipe was started after 1cm of model footing settlement.

Table 4.2. Classification of sand density according to the value of relative density Mithcell and Soga (2005).

Relative Density, D_r (%)	**Description**
0-20	Very Loose
20-40	Loose
40-60	Medium Dense
60-80	Dense
80-10	Very Dense

4.1. Effect on Bearing Capacity and Soil Displacement

4.1.1. Model Tests Without Buried Pipe

The relative density effect on load-bearing capacity and soil displacement of different relative density sands without a buried pipe is discussed in this section. The results are analyzed in two subsections, which are the base pressure-settlement relationship and PIV results. For this section, T1, T4 and T9 model tests are used. Test setups of T1, T4 and T7 can be seen in Table 4.2.

Firstly, base pressure-model footing settlement results are discussed. Values of base pressure are normalized according to the highest base pressure within T1, T4 and T7 at a maximum settlement, which is equal to 10% of the model footing width. For the three model tests, T7 has the highest base pressure at the ultimate settlement state, corresponding to 95.14kPa at 65%.

As can be seen from Figure 4.4, the base pressure at the ultimate settlement state level increases as the relative density does. The base pressure of the loosest soil was 45% of that of the densest soil, whereas the medium-density soil (T4) could carry 80% of the densest soil at the ultimate settlement state. Higher relative density means lower porosity in the sands, leading to lower compressibility and high interlocking forces between soil particles, which could be the reason higher relative density sand resists the most base pressure. Furthermore, if the base pressure-model footing settlement curve is examined, which is given in Figure 4.3, T4 is steeper than T7; nevertheless, as the model footing settlement increases, the ultimate base pressure value is higher in T7.

Table 4.3. Ultimate base pressure values (q_u), model footing settlement ratios (S/B) and relative density values (D_r) for T1, T4 and T7.

Model Test	q_u **(kPa)**	**S/B(%)**	D_r**(%)**	**x/B**
T1	43.61	10	35	-
T2	74.25	10	50	-
T3	95.12	10	65	-

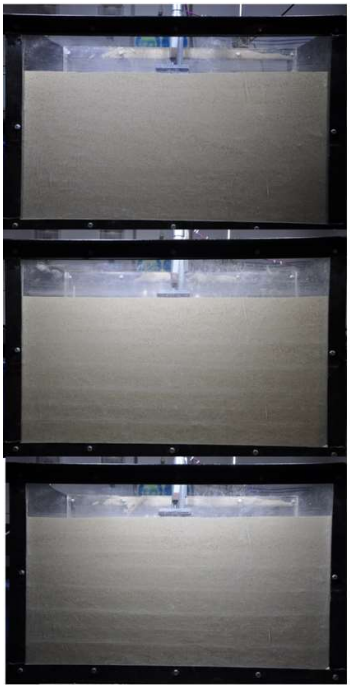


Figure 4.2. T1-T4-T7 test setups, respectively.

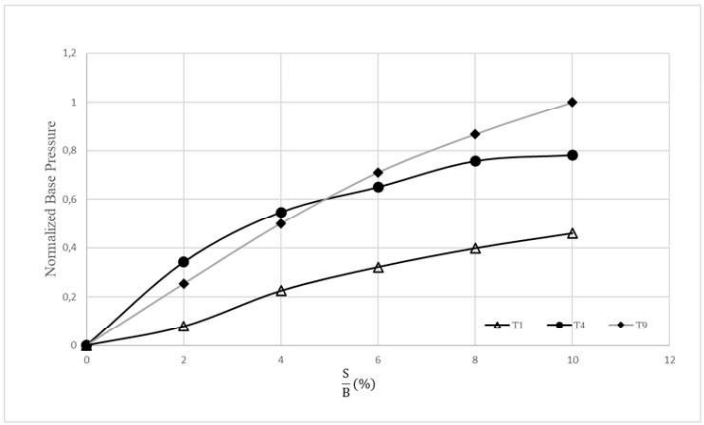


Figure 4.3. Normalized base pressure-model footing settlement ratios for T1,T4 and T7.

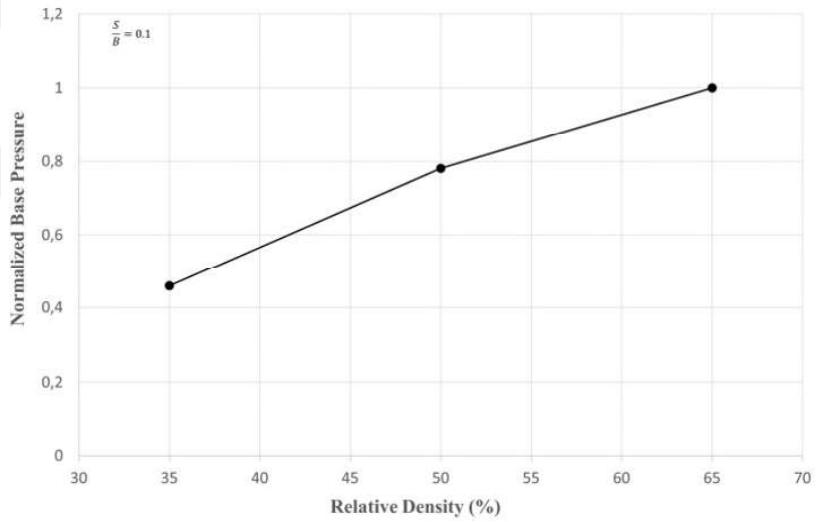


Figure 4.4. Normalized base pressure at ultimate model footing settlement state for T1, T4 and T7.

Secondly, the PIV results of T1, T4 and T7 are examined. The PIV results at the ultimate model footing settlement state, S/B=10%, for model tests T1, T4 and T7 are given in Figure 4.5, Figure 4.6 and Figure 4.7. The vectorial displacement comparison is given in Figure 4.8. PIV results consist of vertical displacement, resultant displacement and shear strain field. If the findings of the shear strain field are analyzed, it can be understood that additional base pressure would cause punching shear failure. Furthermore, dense strain field zone cannot develop further with increasing relative density. If the findings of the vectorial displacement are analyzed, the upward move-

ment of loose soil at T1 is lower compared to T4 and T7. Moreover, all of the model tests are similar according to the downward movement of soil; this might be the result of the same soil compaction procedures in the three model tests. If the findings of the resultant displacements are examined, it can be seen that the displacement patterns of the three model tests are the same. This might show that PIV results are consistent.

4.1.2. Effect on Bearing Capacity and Soil Displacement

In this section, the relative density effect of the buried pipe on bearing capacity and soil displacement is discussed. As in the previous section, the results will be analyzed in two parts. In order to understand the relative density effect, the location of a pipe will be constant and results will be compared as groups. Results of the model tests T2, T5, T8, T3, T6, T9, T10, T13, T11, T14, T12 and T15 will be used. Test setups of the model tests can be seen in Figure 4.9, Figure 4.10, Figure 4.11, Figure 4.12 and Figure 4.13. Which model tests will be compared to each other can be seen in Table 4.4.

Table 4.4. Relative density effect model tests comparisons.

Model Test	D_r(%)	**H/B**	**x/B**	**Comparison No.**
T2	35	0.75	-	1
T5	50			
T8	65			
T3	35	1.5	-	2
T6	50			
T9	65			
T10	35	0.75	0	3
T13	65			
T11	35	0.75	0.75	4
T14	65			
T12	35	0.75	1.5	5
T15	65			

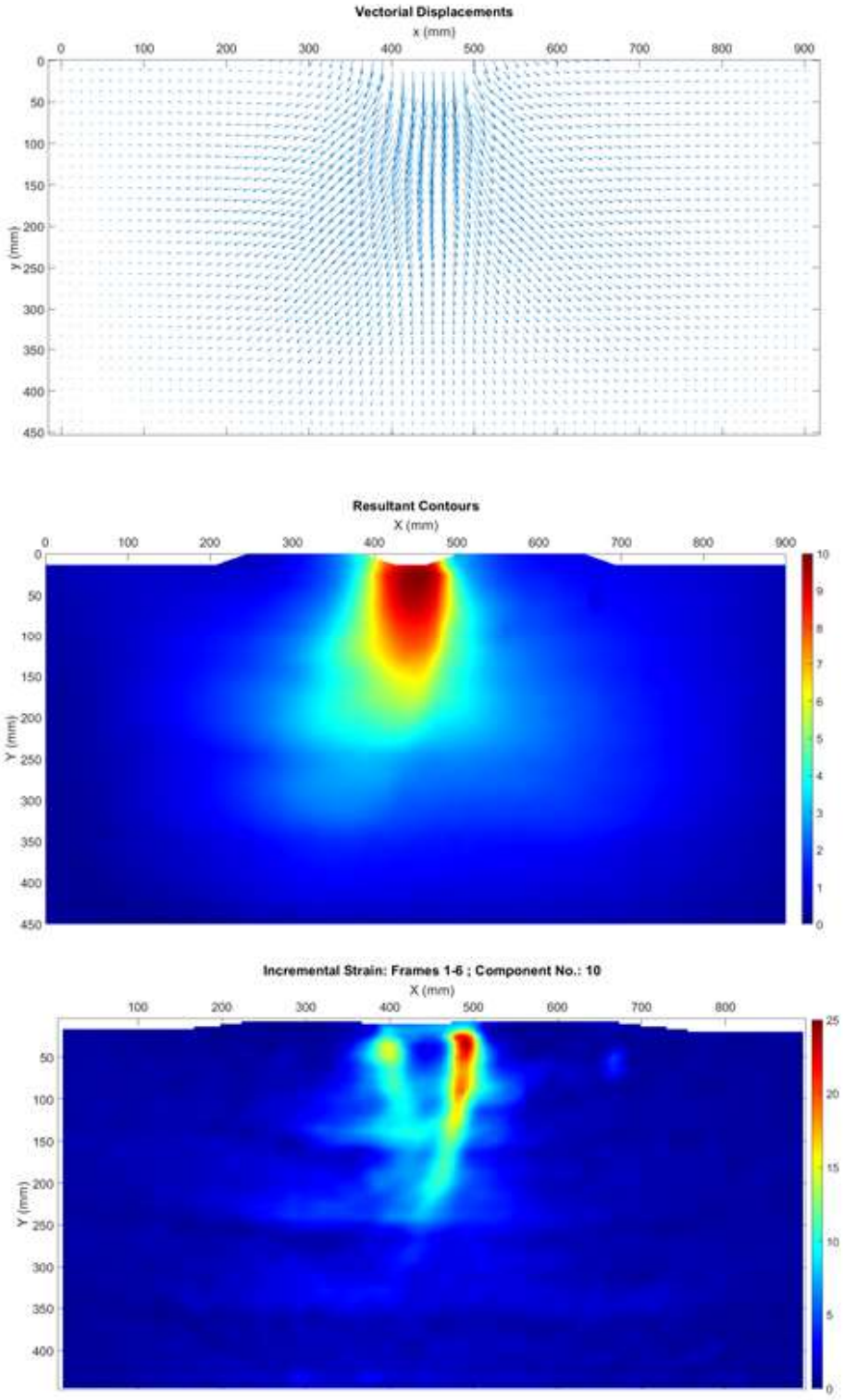


Figure 4.5. Vectorial displacement vectors, resultant displacement contours and shear strain contours at S/B=10% (10mm) vertical model footing settlement for T1.

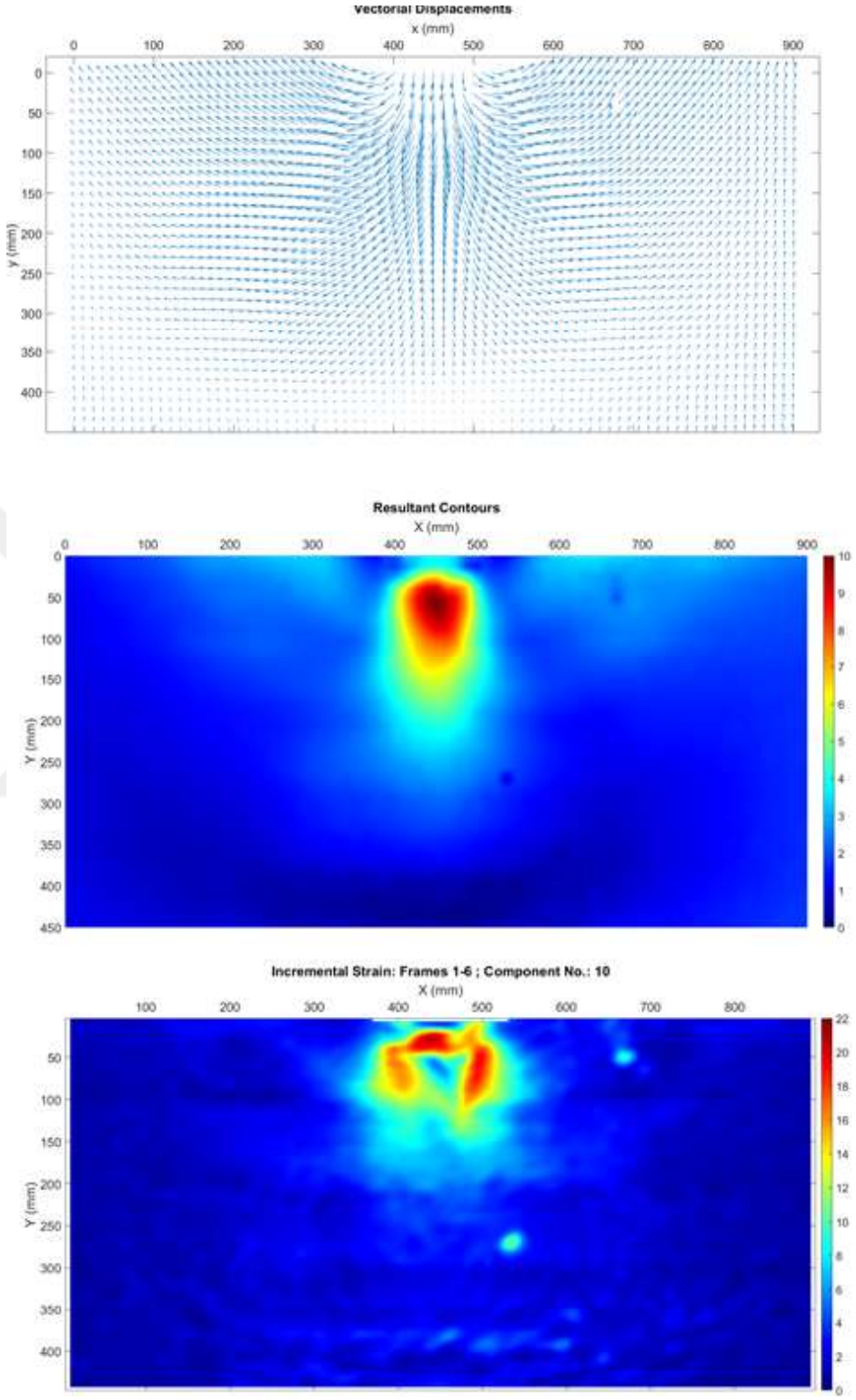


Figure 4.6. Vectorial displacement vectors, resultant displacement contours and shear strain contours at S/B=10% (10mm) vertical model footing settlement for T4.

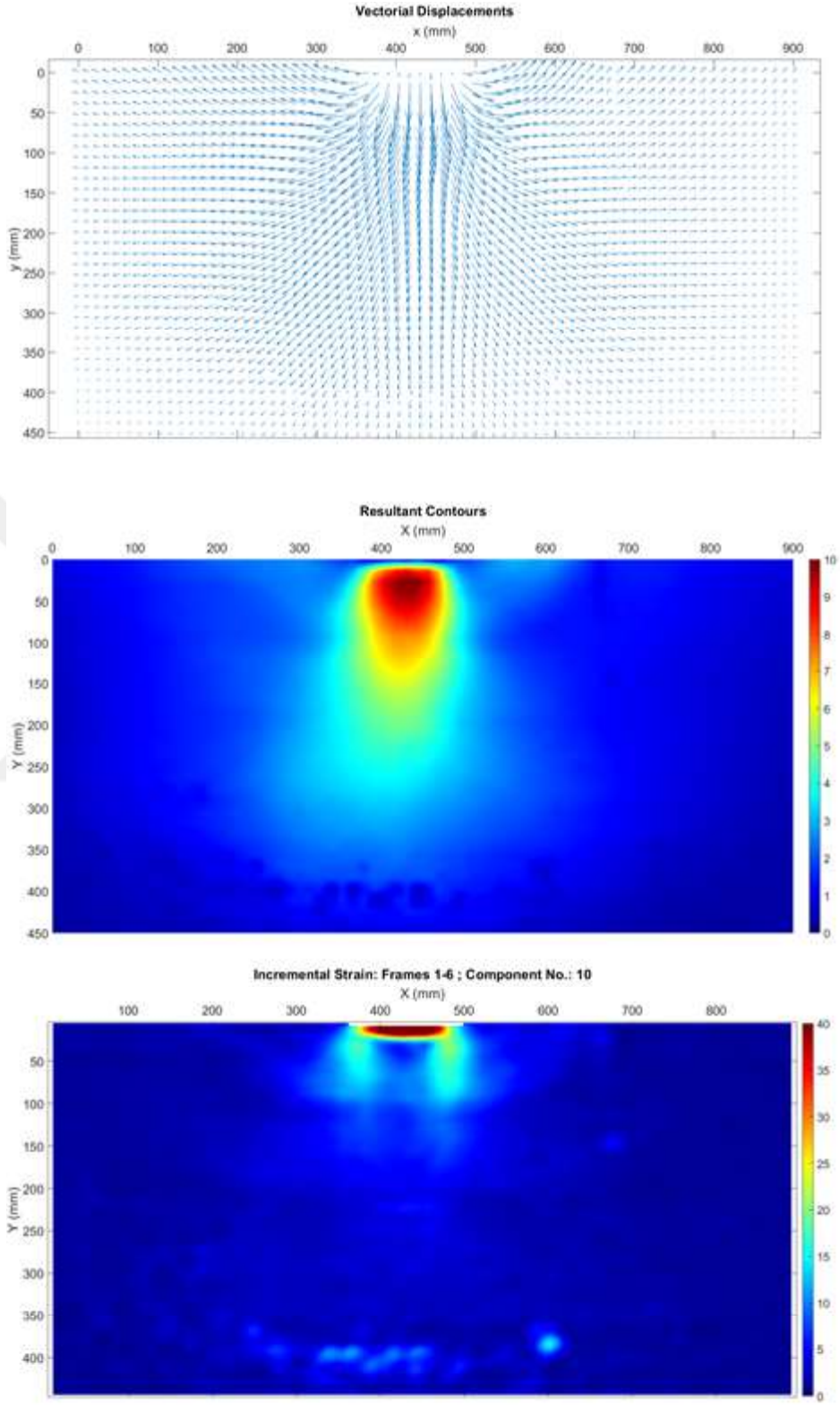


Figure 4.7. Vectorial displacement vectors, resultant displacement contours and shear strain contours at S/B=10% (10mm) vertical model footing settlement for T7.

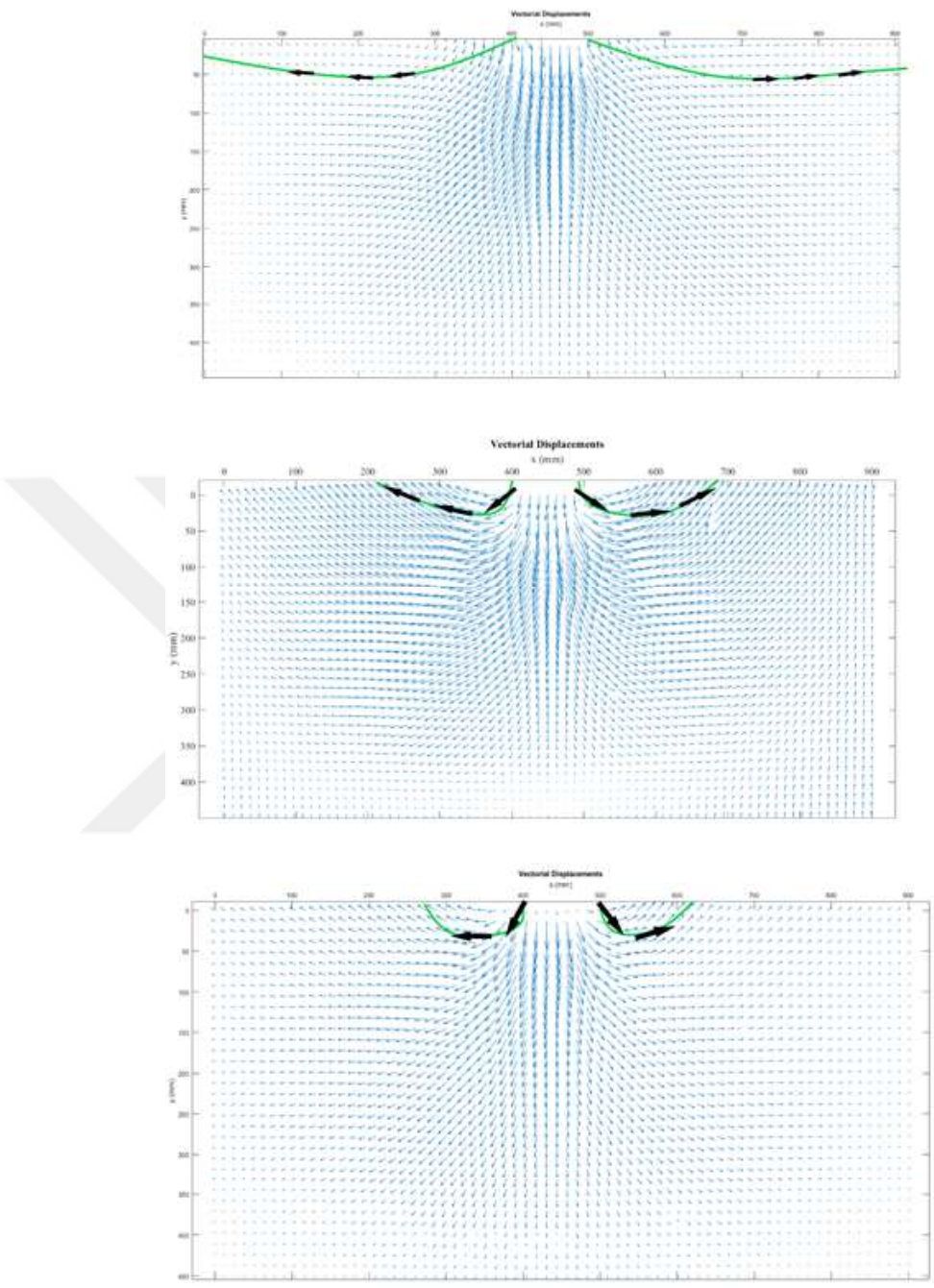


Figure 4.8. Vectorial displacement vectors comparison for T1, T4 and T7 at at S/B=10% (10mm) vertical model footing settlement.

For Comparison 1, firstly, base pressure-model footing settlement results are discussed in Figure 4.14 base pressure values normalized as explained in the previous section (Section 4.1.1.1.). Ultimate base pressures and model footing settlement ratios for the model tests in Comparison 1 are given in Table 4.5.

Table 4.5. Ultimate base pressure values (q_u), model footing settlement ratios and pipe location for comparison 1 model tests.

Model Test	q_u**(kPa)**	**H/B**	**S/B(%)**	D_r**(%)**	**x/B**
T2	32.25	0.75	10	35	-
T5	68.17		10	50	
T8	75.40		10	65	

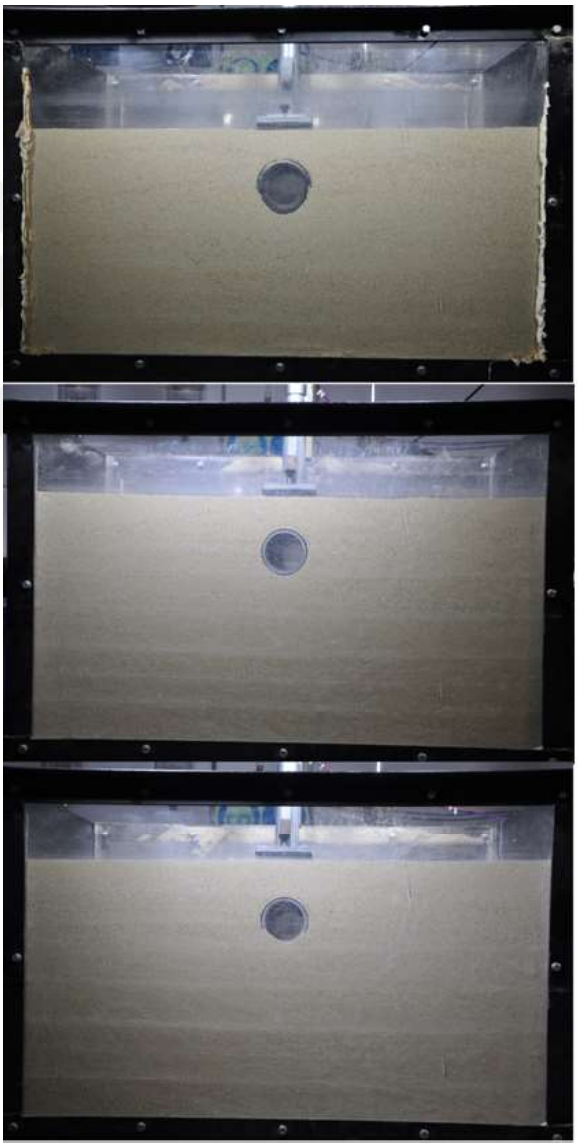


Figure 4.9. Comparison 1 test setups (T2, T5 and T8, respectively).

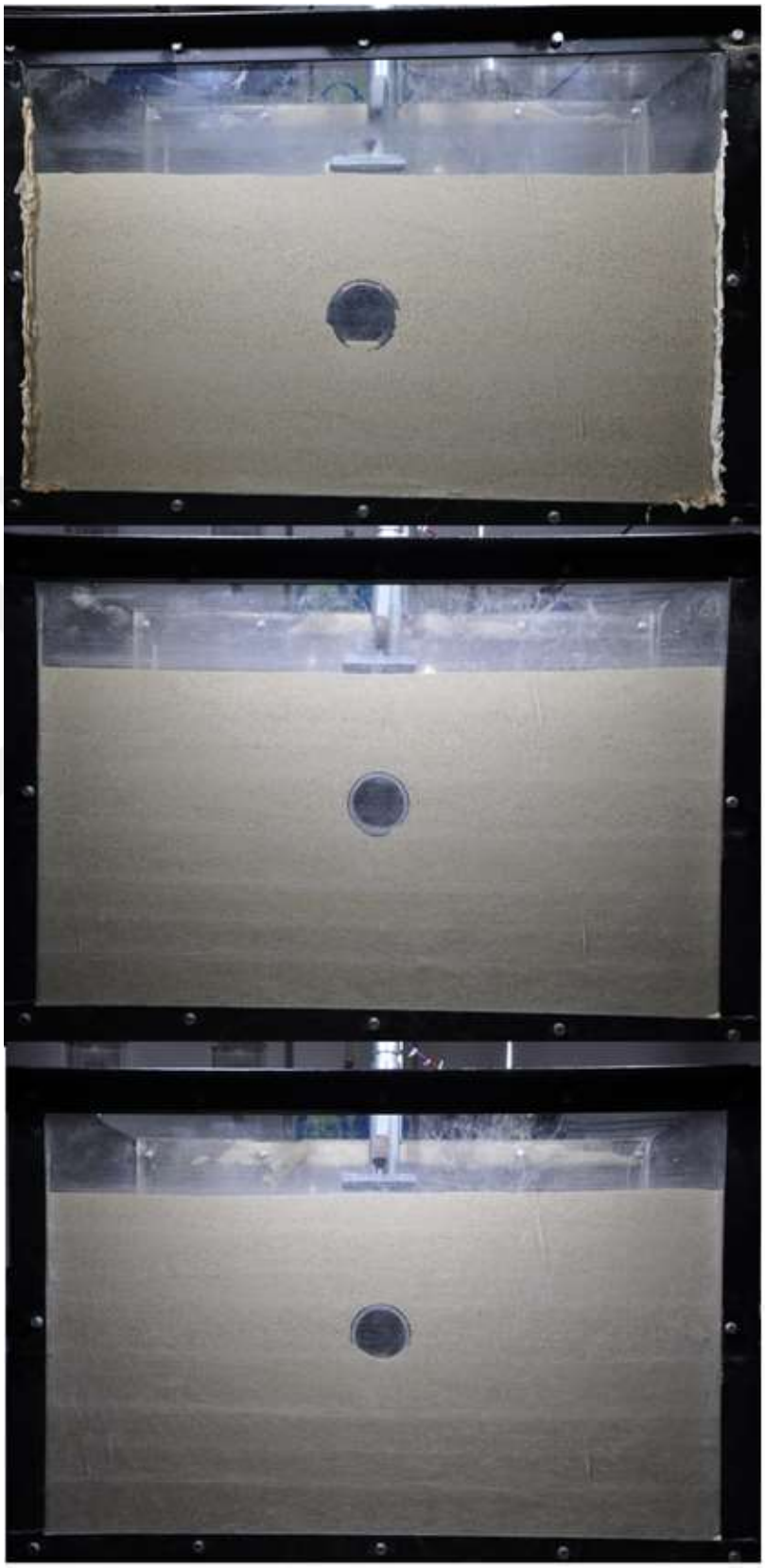


Figure 4.10. Comparison 2 test setups (T3, T6 and T9, respectively).

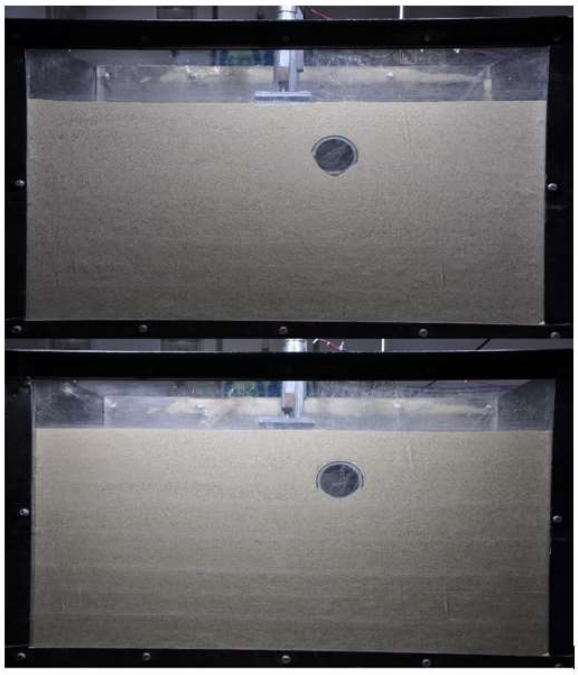


Figure 4.11. Comparison 3 test setups (T10 and T13, respectively).

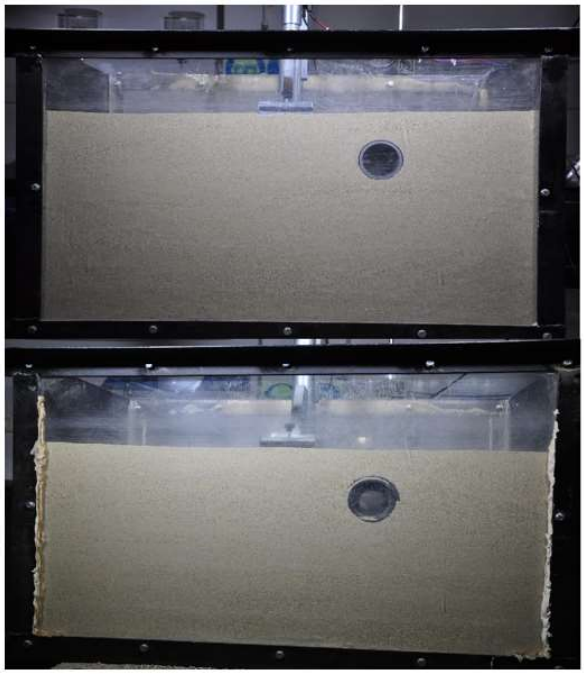


Figure 4.12. Comparison 4 test setups (T11 and T14, respectively).

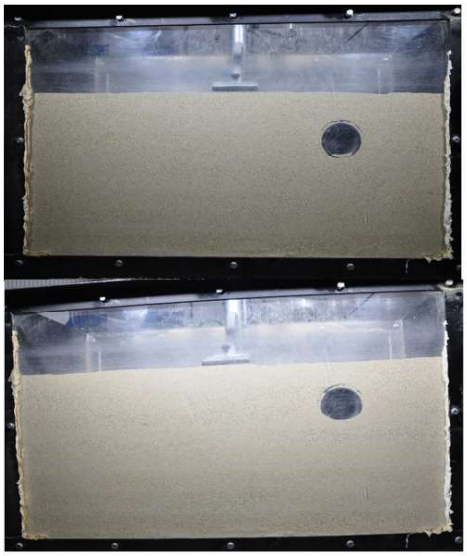


Figure 4.13. Comparison 5 test setups (T12 and T15, respectively).

From the results for the comparison 1, it can be seen that medium-dense soil, T5, creates extra resistance at 0.75 burial depth ratio. According to that, higher stress is expected at the crown of the pipe since this resistance and it should experience more strain. This situation will be analyzed in the following section. Furthermore, it can be seen that loose soil has a 46% ultimate base pressure of the dense soil and medium-dense soil has a 90% ultimate base pressure of the dense soil. These results show the relative density effect more between loose to medium than medium to loose.

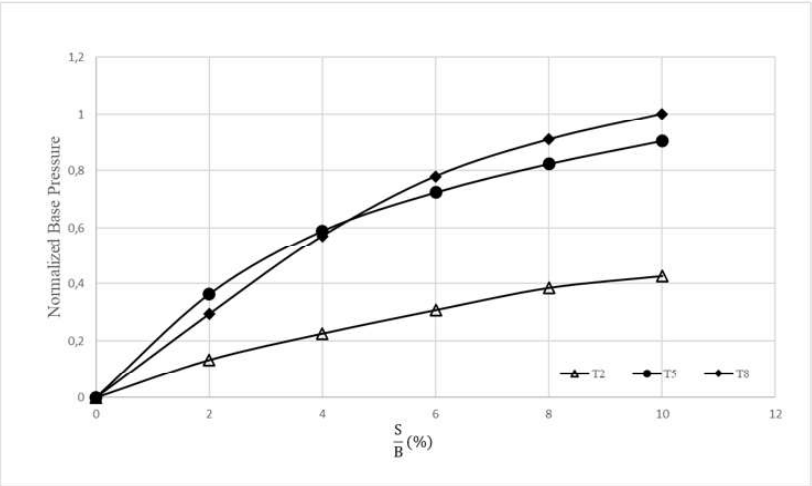


Figure 4.14. Normalized base pressure-model footing settlement ratios for T2,T5 and T8.

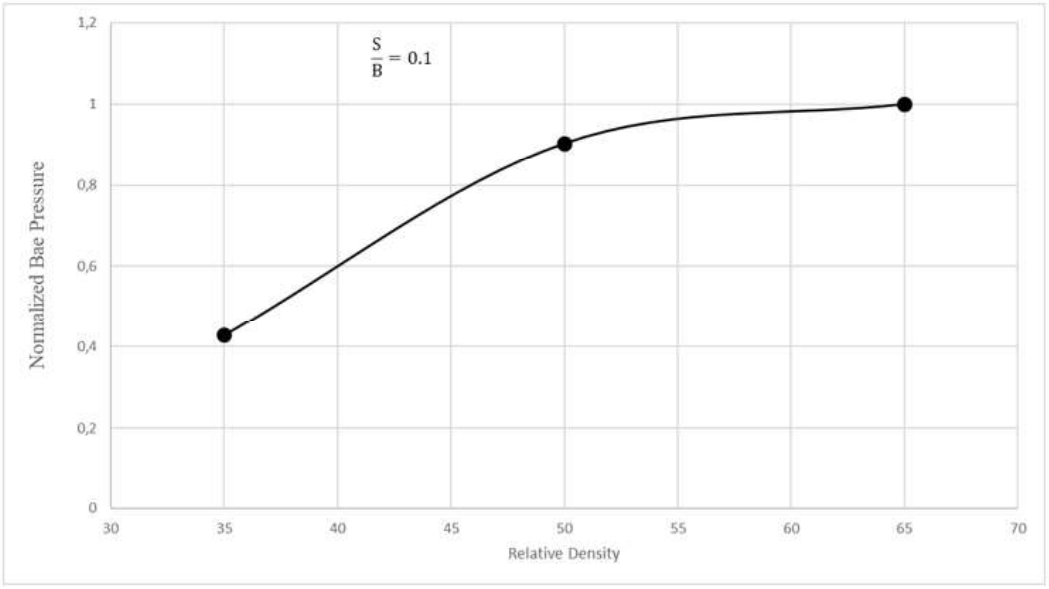


Figure 4.15. Normalized ultimate base pressure at ultimate model footing settlement state for T2, T5 and T8.

As mentioned in Section 3, pipe stresses are measured by strain gauges on pipes. In order to understand the relationship between stress acting on the pipe and the applied base pressure on the model footing, the pipe stress ratio to the model footing base pressure is calculated as;

As mentioned in Section 3, pipe stresses are measured by strain gauges on pipes. In order to understand the relationship between stress acting on the pipe and the applied base pressure on the model footing, the pipe stress ratio to the model footing base pressure is calculated by dividing pipe stress at the relevant strain gauge by applied base pressure on the model footing.

Ultimate base pressure on model footing, stress values on the pipe and stress ratio between them for S/B=0.1 can be seen in Table 4.6 for the comparison 1 model tests.

Table 4.6. Ultimate base pressure values, pipe stress values and stress ratios at S/B=0.1 for bomparison 1 model tests.

Model Test	**Q (kPa)**	s_c **(kPa)**	s_R **(kPa)**	s_L **(kPa)**	S_{RC}	S_{RR}	S_{RL}
T2	32.25	-9.96	0.40	8.46	0.31	0.26	0.26
T5	68.17	-42.06	40.45	37.98	0.62	0.59	0.55
T8	75.40	-24.78	23.10	21.48	0.33	0.31	0.28

It can be understood from Table 4.6 that T5 has the highest stress value, which is a model test conducted with medium-dense soil. The lowest stress ratio occurred at the T2, which is the model test that was conducted with loose soil. This may be because the lower relative density sands have more potential to compress with pressure increases on the footing and the pipe displaces freely, which causes no resistance on the pipe. Furthermore, stress ratio values for the T8 are close to the T2; the reason for this may be that the dense sands have less potential to compress because it is already compressed. Sand located above the pipe may resist the load, which leads to no resistance needed on the pipe. Additionally, stress ratios coming from left and right strain gauges are almost similar due to the centered location of the pipe.

For Comparison 1, secondly, PIV analysis results are discussed. PIV results for Comparison 1 model tests are shown in Figure 4.16, Figure 4.17 and Figure 4.18. It can be understood from the PIV results examination that there are more soil displacements under the pipe for the T2 model test. The reason for this is that T2 has the loosest sand and the expected pipe displacement on the T2 model test is relatively higher. The general soil failure mechanism occurs in between the pipe and the model footing on the T5 and T8 because of the higher relative density sands. For these two model tests, the general failure mechanisms are more clearly detected by PIV analysis.

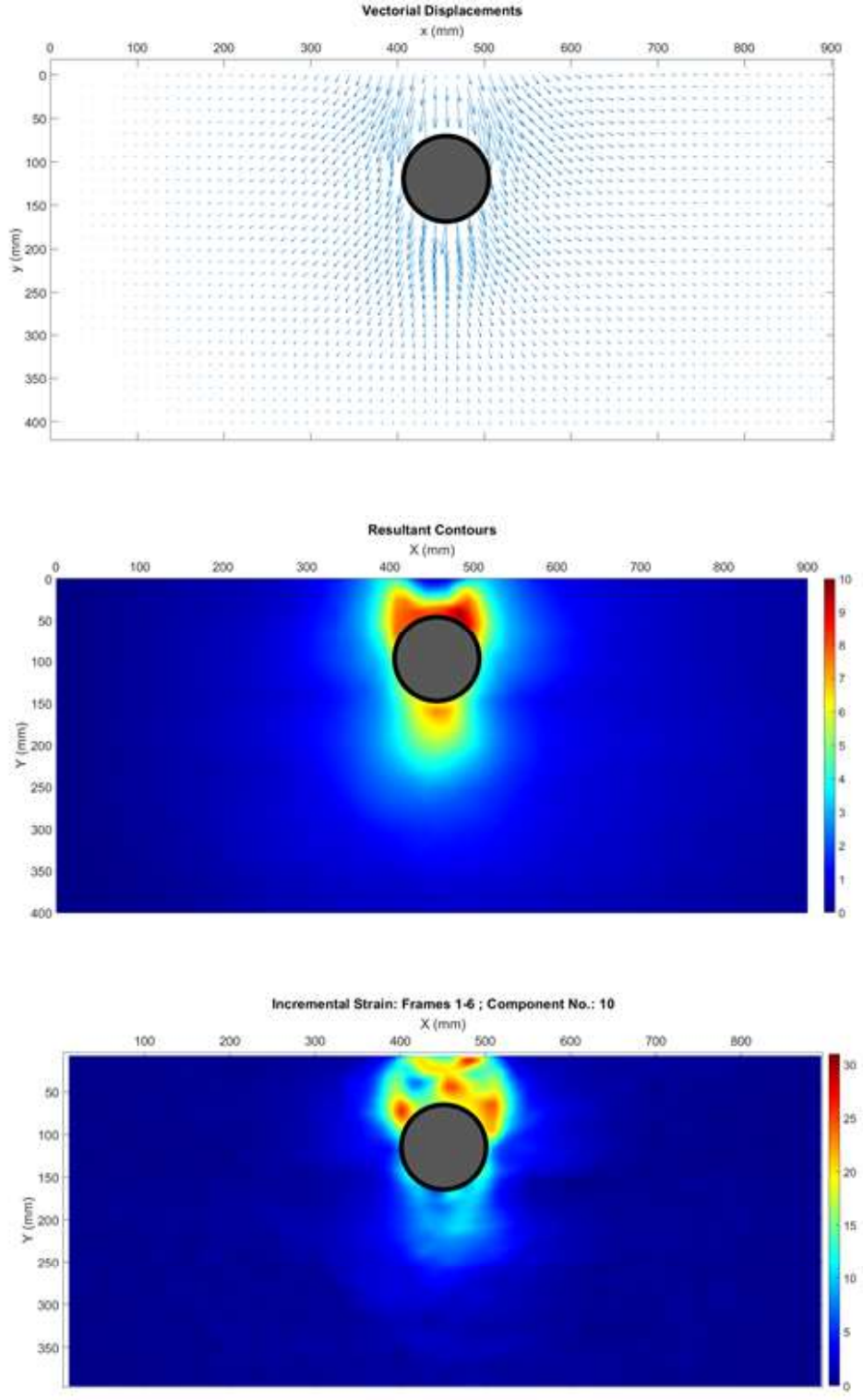


Figure 4.16. Vectorial displacement vectors, resultant displacement contours and shear strain contours at S/B=10% (10mm) vertical model footing settlement for T2.

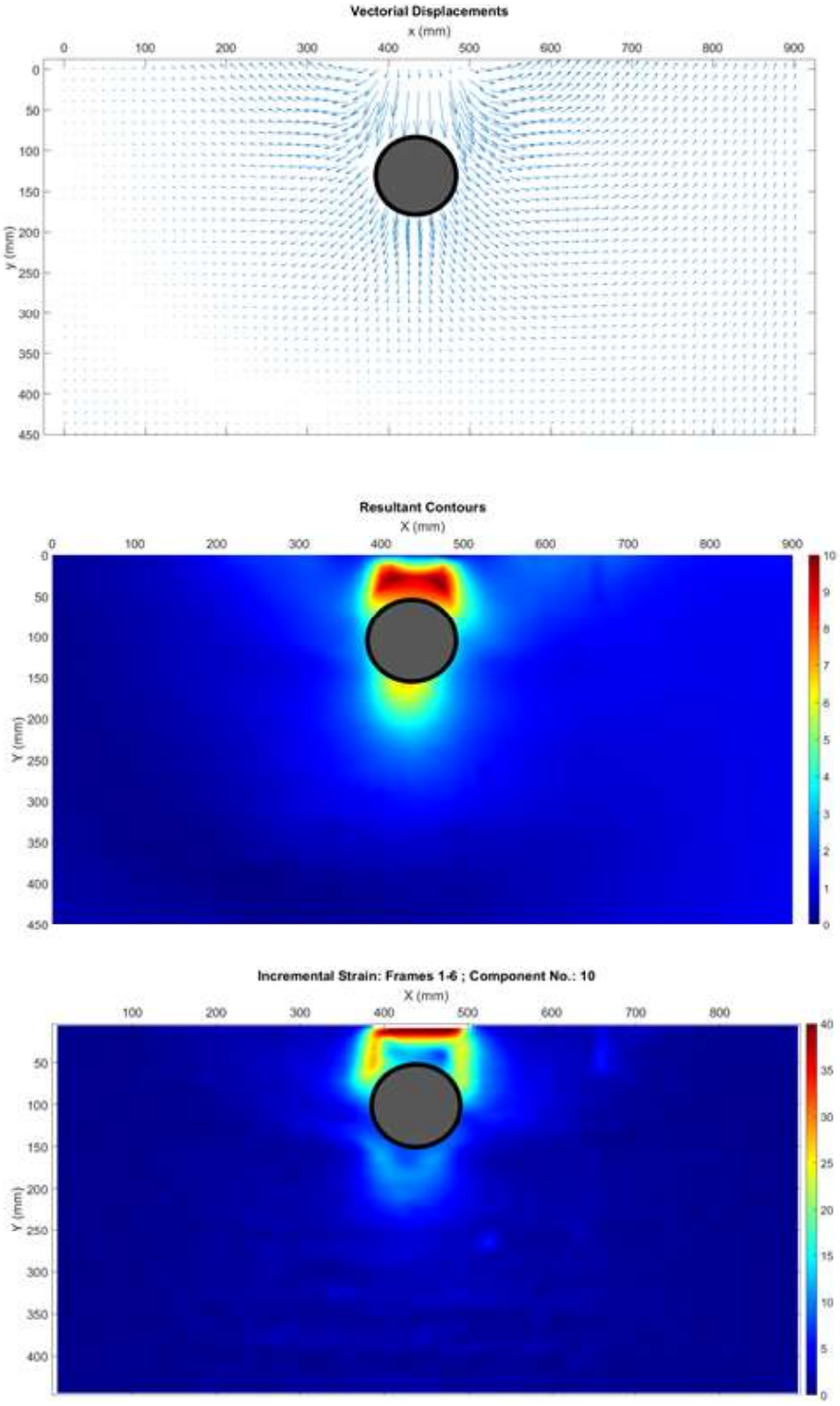


Figure 4.17. Vectorial displacement vectors, resultant displacement contours and shear strain contours at S/B=10% (10mm) vertical model footing settlement for T5.

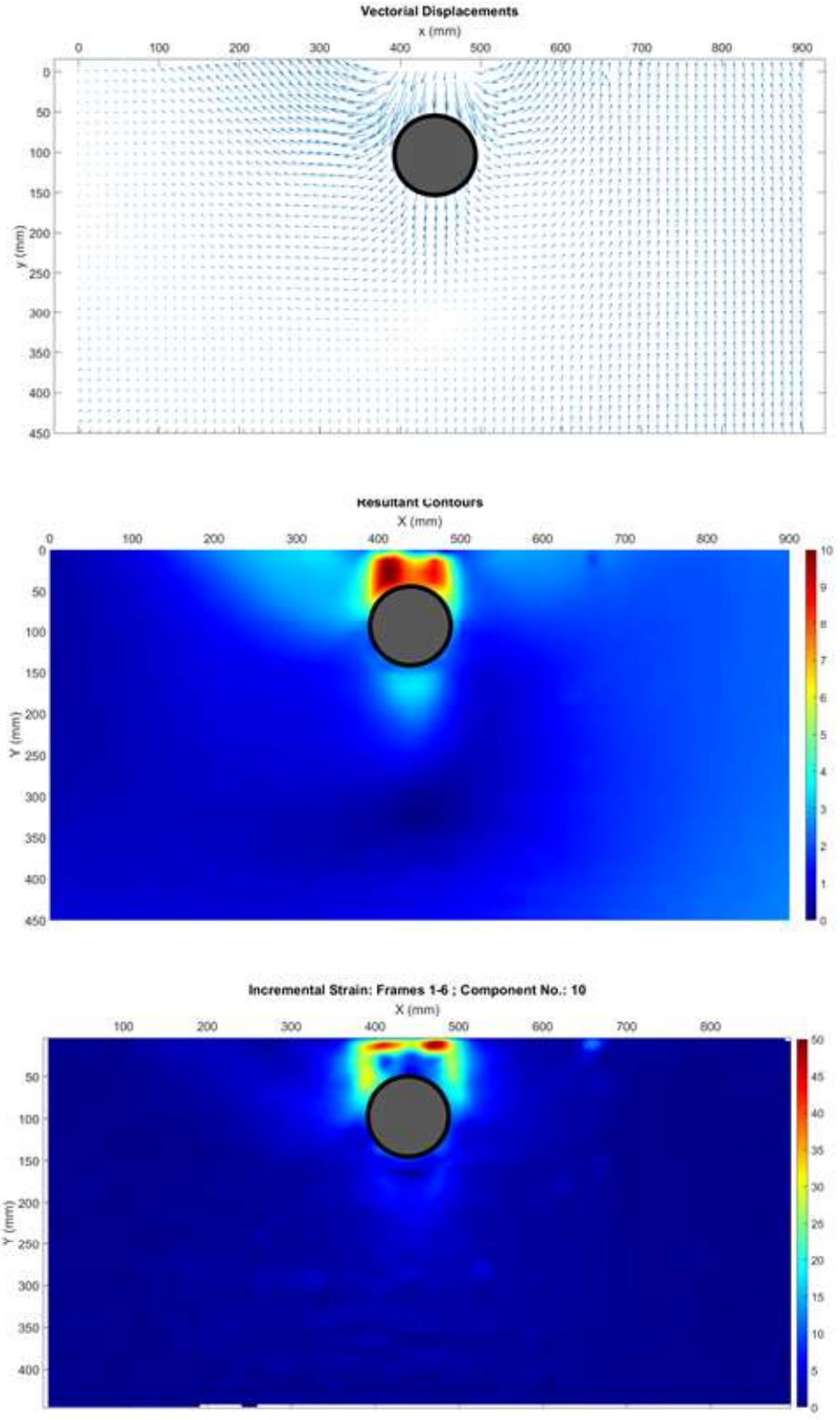


Figure 4.18. Vectorial displacement vectors, resultant displacement contours and shear strain contours at S/B=10% (10mm) vertical model footing settlement for T8.

When shear strain contours are evaluated, it can be seen that T2 model test has the biggest strain distribution on the crown of the pipe. With the increasing relative density, shear contours are located on the upper side of the pipe, not the crown location. Furthermore, when the shear contour scales are examined, it can be seen that, just below the model footing, the highest strain contour occurs for dense soil in the T8 since it has the biggest ultimate base pressure due to its high relative density.

For Comparison 2, firstly, base pressure-model footing settlement results are discussed. In Figure 4.19 base pressure values normalized as explained in the previous section (Section 4.1.1.1.). Ultimate base pressures and model footing settlement ratios for the model tests in Comparison 2 are given in Table 4.7.

Table 4.7. Ultimate base pressure values (q_u), model footing settlement ratios and pipe location for comparison 2 model tests.

Model Test	q_u**(kPa)**	**H/B**	**S/B(%)**	D_r**(%)**	**x/B**
T3	48.95	1.5	10	35	-
T6	73.70		10	50	
T9	77.31		8	65	

From Figure 4.19 it can be seen that the normalized base pressure of the T9 model test starts dropping at S/B=8% and it decreases until the value of S/B=6%. This situation indicates soil failure for dense soil in T9. Despite the soil failure, T9 still has the biggest ultimate base pressure, as expected. Moreover, after the S/B=6%, the slopes of the T3 and T6 curves are decreasing.

From Figure 4.20 indicates that, at S/B = 0.1, T3 and T6 reached around 60% and 90% of T9, respectively and T9 decreased to 95% of its ultimate base pressure at a value of S/B=6%. The soils at T3 and T6 carried additional loads due to their compaction potential at their looser state; nevertheless, the soil at T9 lost its ability to carry additional loads because it has relatively less compaction potential due to being dense soil. Having more compaction potential created an increase in ultimate base pressure for the model tests of T3 and T6.

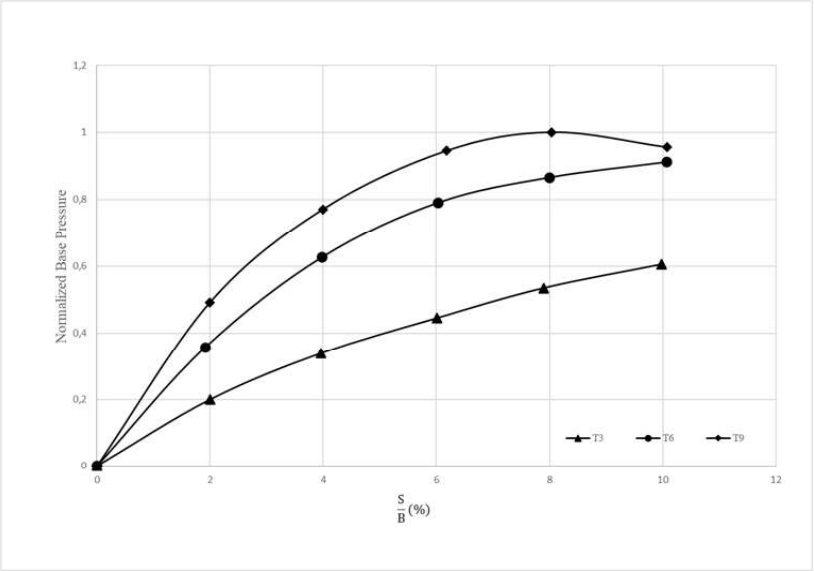


Figure 4.19. Normalized base pressure-model footing settlement ratios for T3,T6 and T9.

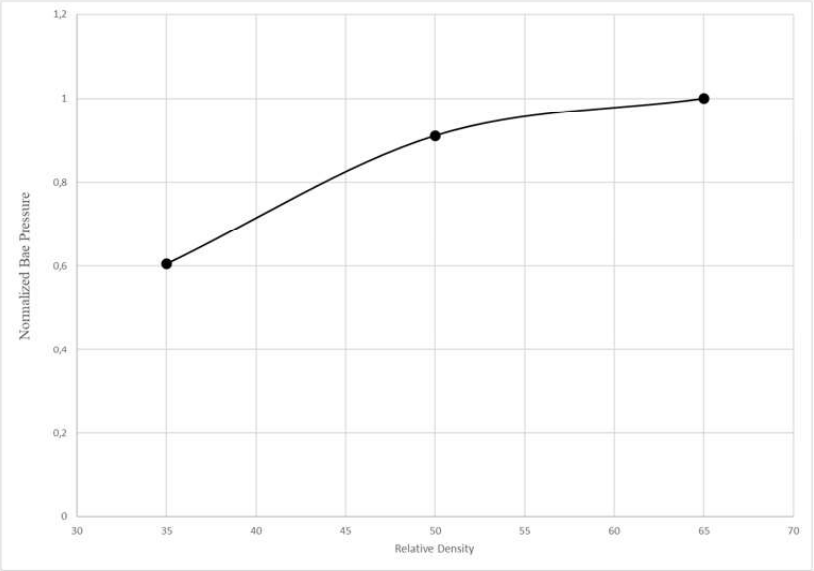


Figure 4.20. Normalized ultimate base pressure at ultimate model footing settlement state for T3, T6 and T9.

Ultimate base pressure on model footing, stress values on the pipe and stress ratio between for S/B=0.1 can be seen in Table 4.8 for the Comparison 2 model tests.

Table 4.8. Ultimate base pressure values, pipe stress values and stress ratios at S/B=0.1 for comparison 2 model tests.

Model Test	**Q (kPa)**	s_c **(kPa)**	s_R **(kPa)**	s_L **(kPa)**	S_{RC}	S_{RR}	S_{RL}
T3	48.95	-3.42	3.00	2.82	0.07	0.06	0.06
T6	73.70	-30.60	22.44	24.00	0.42	0.30	0.32
T9	77.31	-15.36	12.66	11.77	0.20	0.16	0.15

When Table 4.8 is examined, it can be seen that the highest stress ratio values occurred at T6, where soil is medium-dense soil. It can be explained by the fact that medium-dense soil has transmitted more load than others. Furthermore, stress ratios coming from left and right are similar to each other because pipe is located in the center. Although the ultimate base pressures of T6 and T9 are relatively close to each other, compared to T3 and T6, their stress ratios for the exact strain gauge locations are slightly different from each other.

For Comparison 2, secondly, PIV analysis results are discussed. PIV results for Comparison 2 model tests are shown in Figure 4.21, Figure 4.22 and Figure 4.23. It can be understood from the PIV results examination that there is more soil displacement under the pipe for the T3 model test. The reason for this is that T3 has the loosest sand and the expected pipe displacement on the T3 model test is relatively higher. The general soil failure mechanism occurs in between the pipe and the model footing on the T6 and T9 because of the higher relative density sands. For these two model tests, the general failure mechanisms are more clearly detected by PIV analysis. As can be seen from the PIV results, soil failure that occurred at T9 has not affected the PIV analysis.

When shear strain contours are evaluated, it can be seen that T3 model tests have the most shear strain distribution on the crown of the pipe. With the increasing relative density, shears strain contours located on the sand, which is at the above of the pipe, not the crown location. Furthermore, when the shear strain contour scales are examined, it can be seen that, just below the model footing, the highest strain contour

occurs for dense soil in the T9 since it carries the biggest ultimate base pressure due to its high relative density.

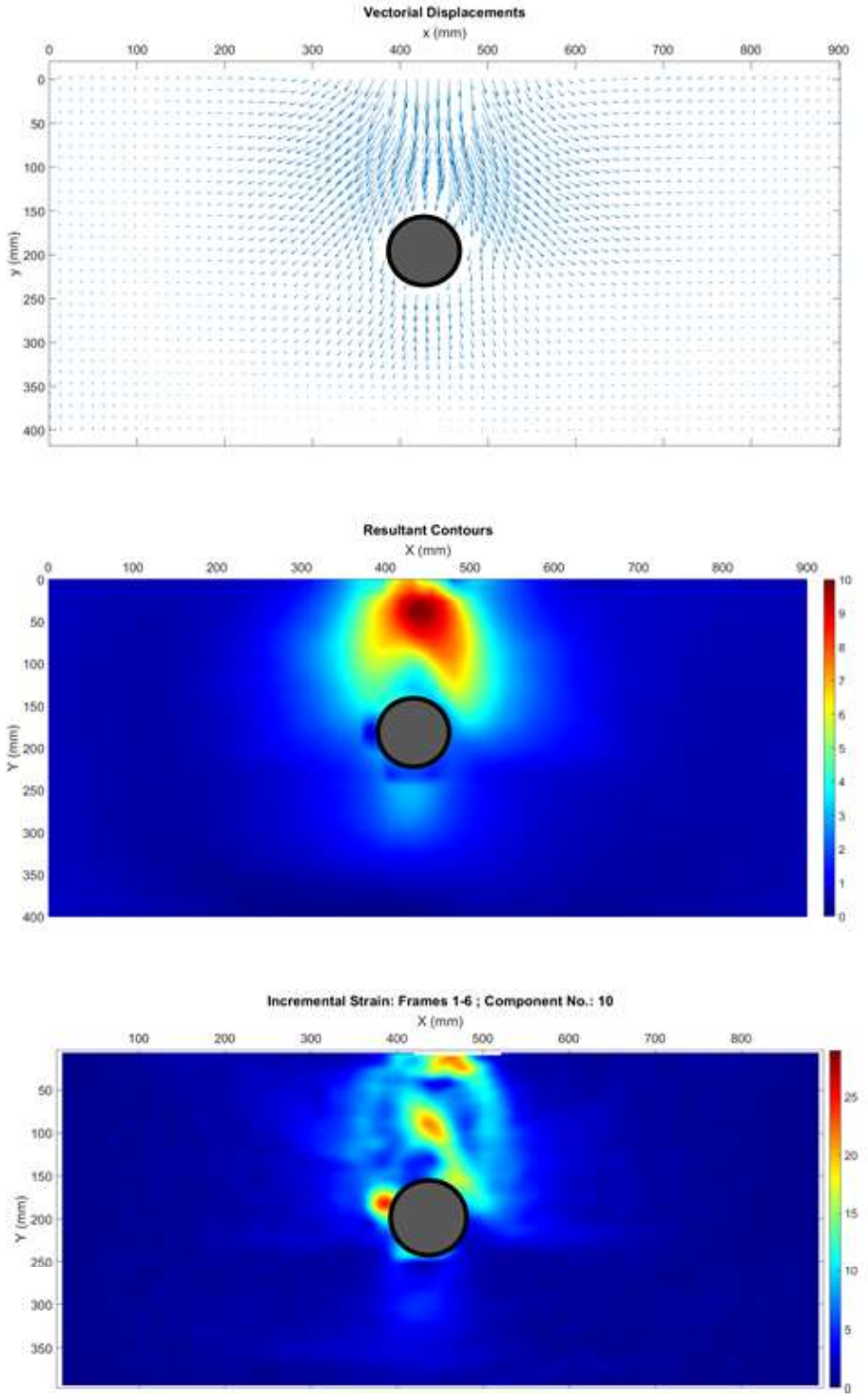


Figure 4.21. Vectorial displacement vectors, resultant displacement contours and shear strain contours at S/B=10% (10mm) vertical model footing settlement for T3.

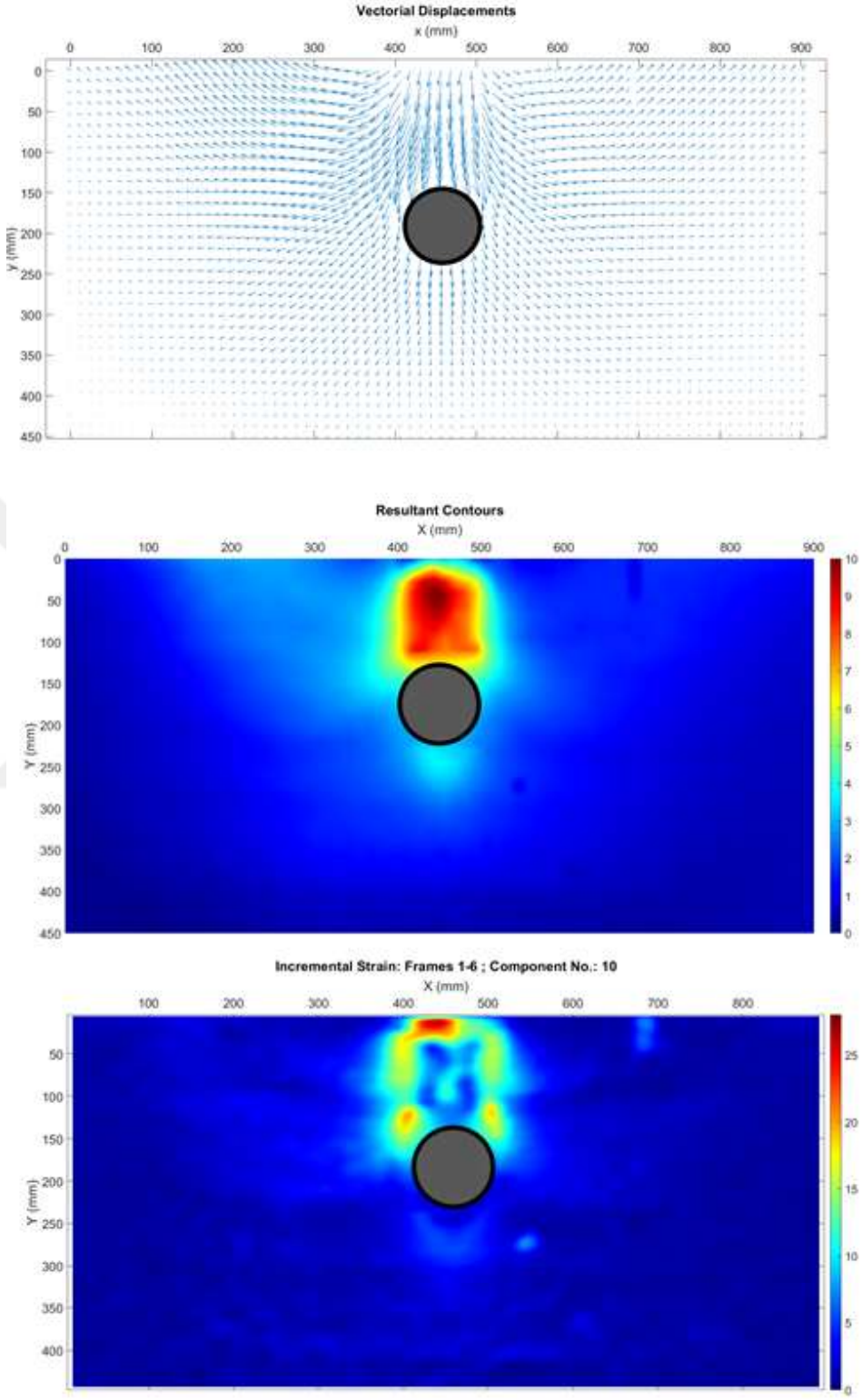


Figure 4.22. Vectorial displacement vectors, resultant displacement contours and shear strain contours at S/B=10% (10mm) vertical model footing settlement for T6.

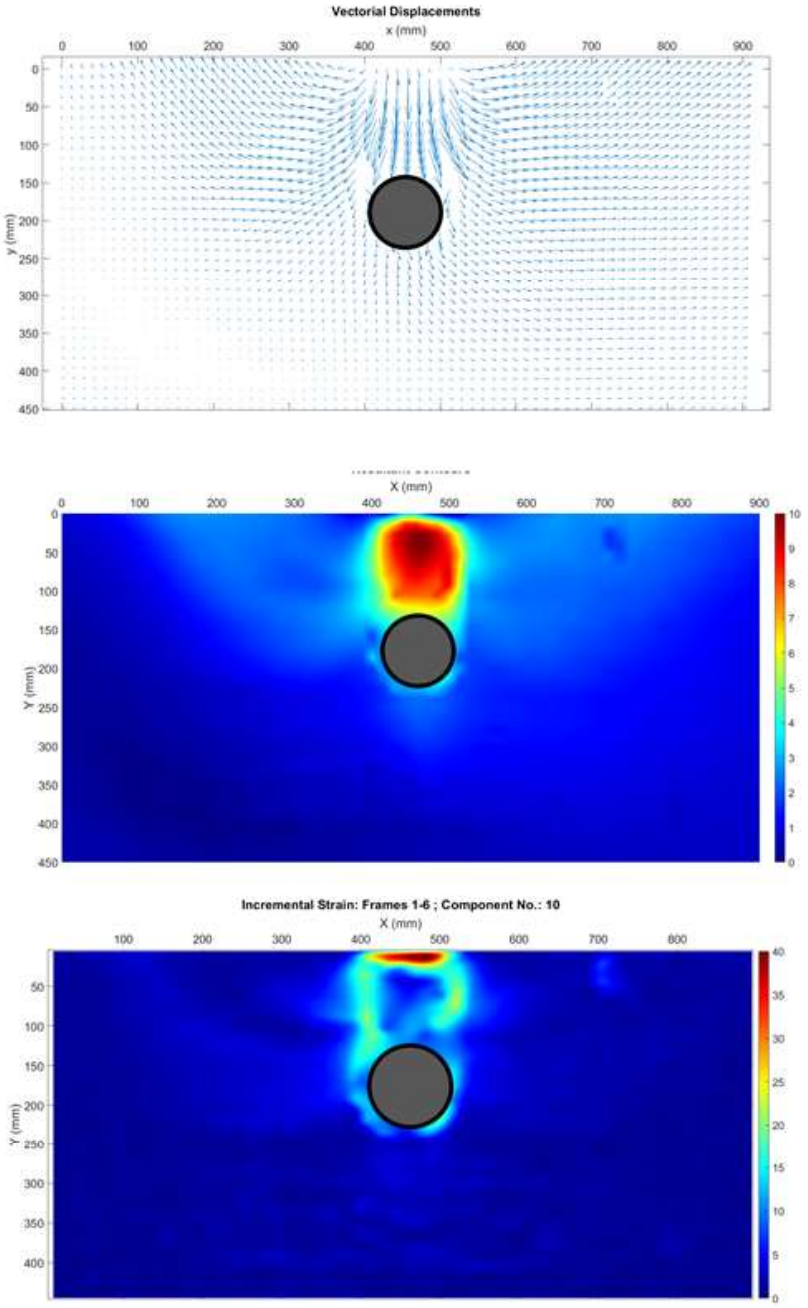


Figure 4.23. Vectorial displacement vectors, resultant displacement contours and shear strain contours at S/B=10% (10mm) vertical model footing settlement for T9.

Comparison 3, firstly, base pressure-model footing settlement results are discussed in Figure 4.19 base pressure values normalized as explained in the previous section (Section 4.1.1.1.). Ultimate base pressures and model footing settlement ratios for the model tests in Comparison 3 are given in Table 4.9.

Table 4.9. Ultimate base pressure values (q_u), model footing settlement ratios and pipe location for comparison 3 model tests.

Model Test	q_u**(kPa)**	**H/B**	**S/B(%)**	D_r**(%)**	**x/B**
T10	29.40	0.75	10	35	0
T13	68.16		10	65	

From Figure 4.19, it can be seen that both of the normalized base pressure-model footing settlement curves experienced a decrease according to their beginning slope after the S/B=6%. After S/B=6%, the curve of T10 has an almost steady slope until S/B=10%; nevertheless, curve T13's slope has decreased between the S/B=8% and S/B=10%. The last decrease of the curve slope shows that, after S/B=8%, dense soil of T13 resists less load per displacement.

Figure 4.20 indicates that, at S/B = 0.1, T10 reached around 40% of T13. These result is also coherent with the other comparisons, as expected.

Ultimate base pressure on model footing, stress values acting on the pipe and stress ratio between for S/B=0.1 can be seen in Table 4.10 for the Comparison 3 model tests.

Table 4.10. Ultimate base pressure values, pipe stress values and stress ratios at S/B=0.1 for comparison 3 model tests.

Model Test	**Q (kPa)**	s_c **(kPa)**	s_R **(kPa)**	s_L **(kPa)**	S_{RC}	S_{RR}	S_{RL}
T10	29.40	-0.48	0.36	0.54	0.0163	0.0122	0.0184
T13	68.16	-3.72	-0.6	5.58	0.0555	0.0082	0.082

When Table 4.10 examined, it can be seen that with higher relative density, stress ratios increased. For the T13 model test, the stress ratio for the left side strain is the highest one it could be because the left side strain is the closest one to the center of the footing. For the right side strain stress ratio values, T10 has the higher value and also, it can be seen that for T13, the right side of the pipe experienced compression due to having a negative strain value.

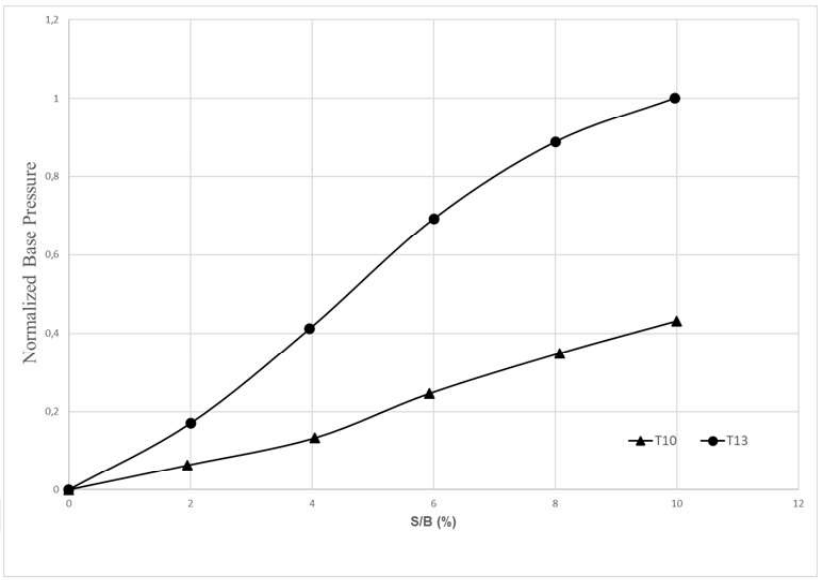


Figure 4.24. Normalized base pressure-model footing settlement ratios for T10 and T13.

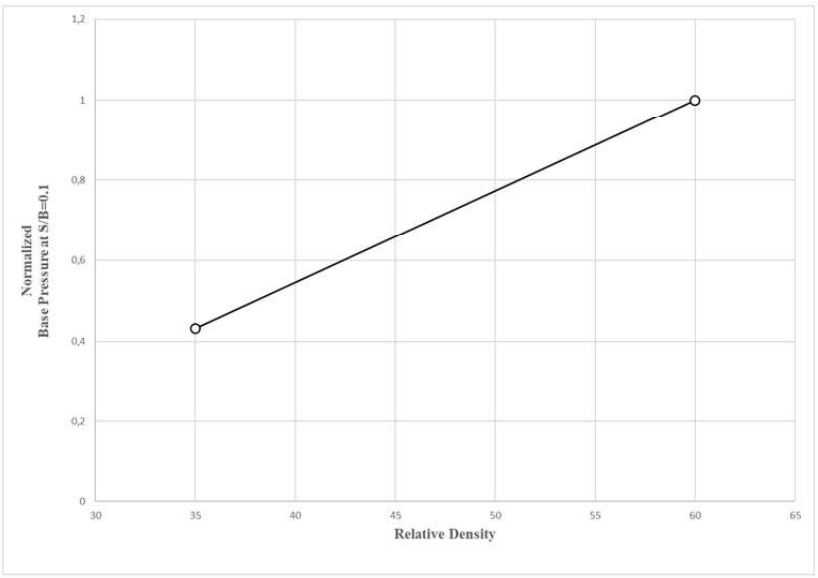


Figure 4.25. Normalized ultimate base pressure-model footing settlement ratios for T10 and T13.

For Comparison 3, secondly, PIV analysis results are discussed. PIV results for Comparison 3 model tests are shown in Figure 4.26 and Figure 4.27. It can be understood from the PIV results examination that, for T10, soil displacements reach a deeper level than T13. For both results, it can be seen that soil displacement happens

on the left side of the test box due to having an unsymmetrical pipe location. When the soil displacement was examined, it could be seen that the soil of T13 moved more to the left side of the test box than soil T10 since it can be seen that the displacement of soil T10 is wider. Furthermore, from the vectorial displacement vectors, it can be seen that for T13, there is an upward movement of the soil on the right side of the pipe. The movement of the soil located above the pipe is higher for T10 model tests; this may be due to having a lower relative density. Just below the pipe, almost no soil displacement occurred in T13; nevertheless, T10 soil experienced displacement just below the pipe.

When shear strain contours are evaluated, it can be seen that the T10 model test has a bigger shear strain distribution on the crown of the pipe. Just below the footing, the soil of T13 has the bigger shear strain due to resisting higher load because of its relative density. Shear strain distribution is identical for both model tests, but below the pipe soil of T10, it has experienced a slightly bigger shear strain. It can be understood that on the left side of the pipe, T13 has a bigger strain distribution. When the general shape of the shear strain contours is examined for both model tests, it can be seen as the same pathways, but T13 has more distribution at the elevation of the pipe location. This may be due to having bigger pressure on T13 coming from the model footing.

For Comparison 4, firstly, base pressure-model footing settlement results are discussed in Figure 4.28 base pressure values normalized as explained in the previous section (Section 4.1.1.1.). Ultimate base pressures and model footing settlement ratios for the model tests in Comparison 4 are given in Table 4.11.

Table 4.11. Ultimate base pressure values (q_u), model footing settlement ratios and pipe location for comparison 4 model tests.

Model Test	q_u**(kPa)**	**H/B**	**S/B(%)**	D_r**(%)**	**x/B**
T11	34.38	0.75	10	35	0.75
T14	70.72		10	65	

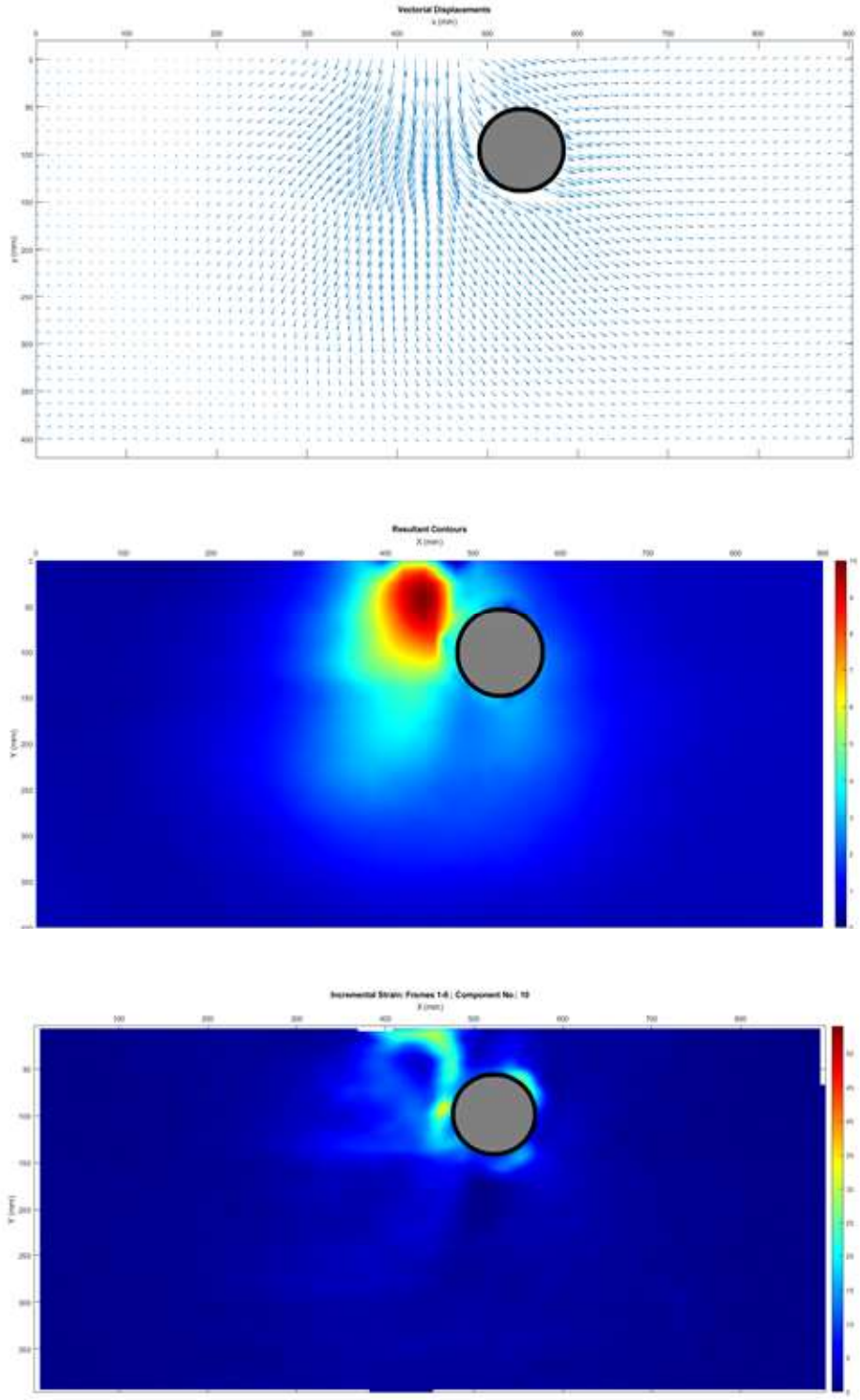


Figure 4.26. Vectorial displacement vectors, resultant displacement contours and shear strain contours at S/B=10% (10mm) vertical model footing settlement for T10.

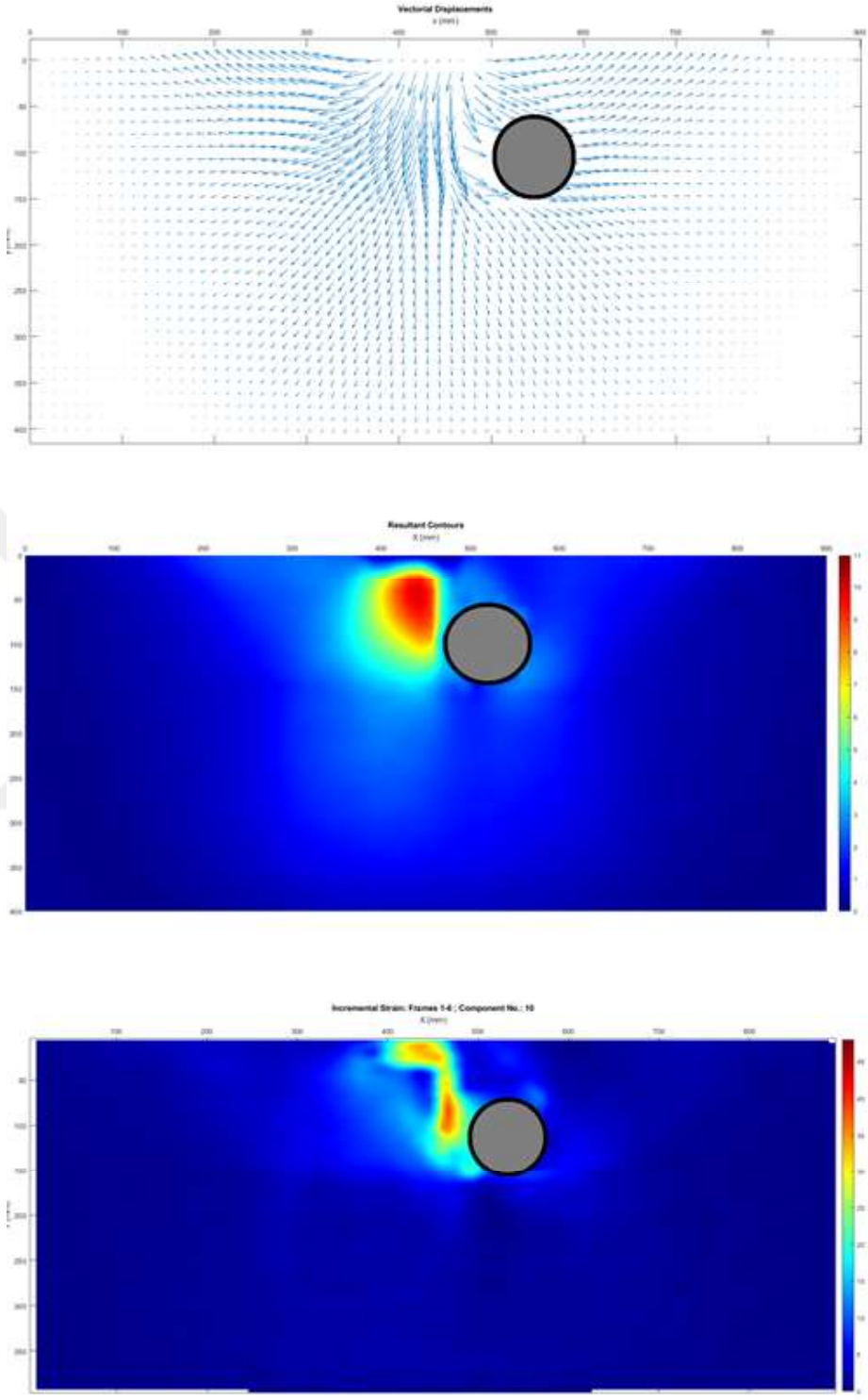


Figure 4.27. Vectorial displacement vectors, resultant displacement contours and shear strain contours at S/B=10% (10mm) vertical model footing settlement for T13.

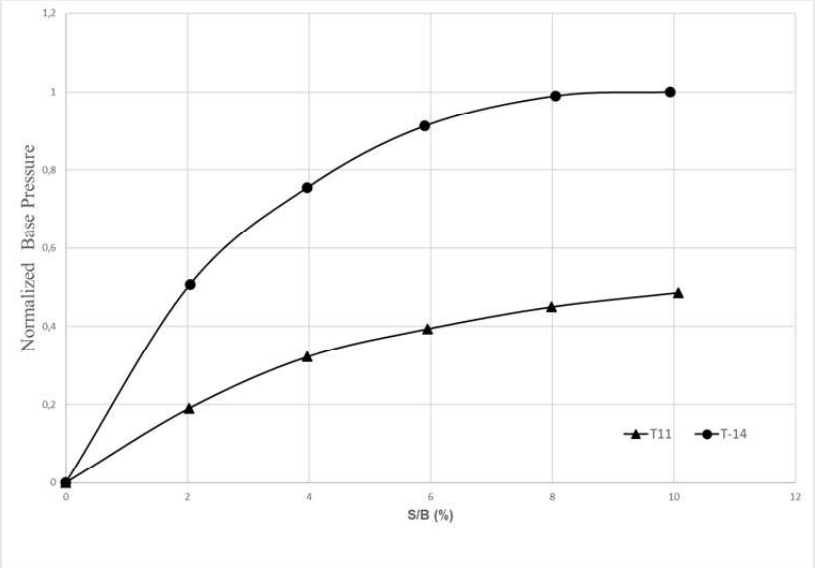


Figure 4.28. Normalized base pressure-model footing settlement ratios for T11 and T14.

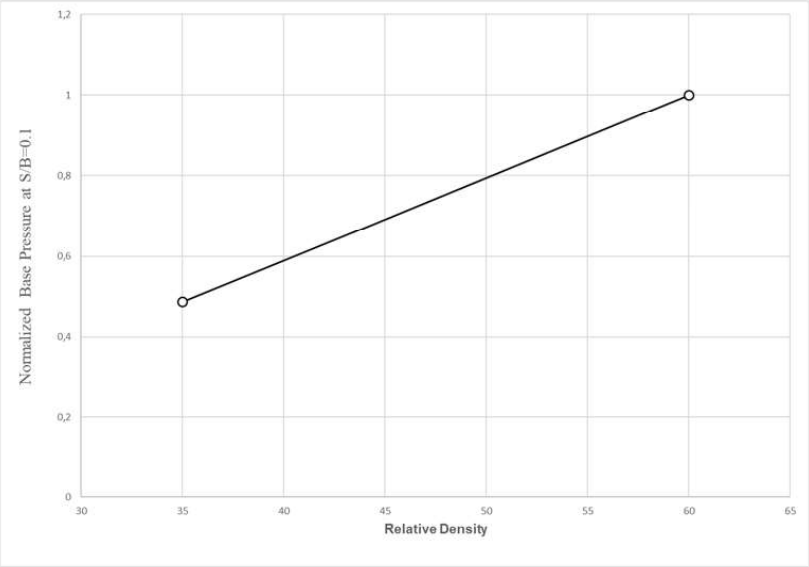


Figure 4.29. Normalized ultimate base pressure-model footing settlement ratios for T11 and T14.

From Figure 4.28, it can be seen that both of the normalized base pressure-model footing settlement curves started steep between S/B=0 to S/B=2%; then, they have a decrease in the curves' slopes. At S/B=8%, the soil of T14 almost reached its ultimate base pressure. It shows that between S/B=8% to S/B=10%, there is practically no bearing capacity increase; nevertheless, T11 has a steeper curve between S/B=8% to

S/B=10%. The reason for this result is the relative density difference between soils. Due to having larger voids with the pipe relatively close to the center, T11 has more compaction potential; therefore, its ultimate base pressure can increase more with the same amount of settlement, according to the T14. Furthermore, this can be supported by examining the normalized base pressure values at S/B=2%. At S/B=2%, T14 already reaches the ultimate base pressure value of T11, but at S/B=10%, which is five times higher than S/B=2%, the ultimate base pressure of T14 is only almost two times higher than the ultimate base pressure of T11.

Figure 4.29 indicates that, at S/B = 0.1, T11 reached almost 50% of T14. This result is also coherent with the other comparisons, as expected. Ultimate base pressure difference occurs due to having different relative densities, but uncentralized soil location also affected this result, which will be discussed in the following section.

Ultimate base pressure on model footing, stress values acting on the pipe and stress ratio between for S/B=0.1 can be seen in Table 4.12 for the Comparison 4 model tests.

Table 4.12. Ultimate base pressure values, pipe stress values and stress ratios at S/B=0.1 for comparison 4 model tests.

Model Test	**Q (kPa)**	s_c **(kPa)**	s_R **(kPa)**	s_L **(kPa)**	S_{RC}	S_{RR}	S_{RL}
T11	34.38	0.6	-0.12	-0.18	0.0175	0.0034	0.0052
T14	70.72	1.26	-1.14	-1.5	0.018	0.0161	0.0212

When Table 4.10 is examined, it can be seen that with higher relative density, stress ratios increased. For the T14 model test, the stress ratio for the left side strain is the highest one it could be because the left side strain is the closest one to the center of the footing. Stress ratios for crown location are almost the same for both tests; nevertheless, for the right and left sides, stress ratios are higher in the T14 due to having higher load transfer for the buried pipe's sides. Furthermore, it can be seen that in both of the tests, the crown of the pipe experienced tension; nevertheless, the sides

of the pipes experienced compression. Secondly, PIV analysis are discussed, which can be seen in Figure 4.30 and Figure 4.31.

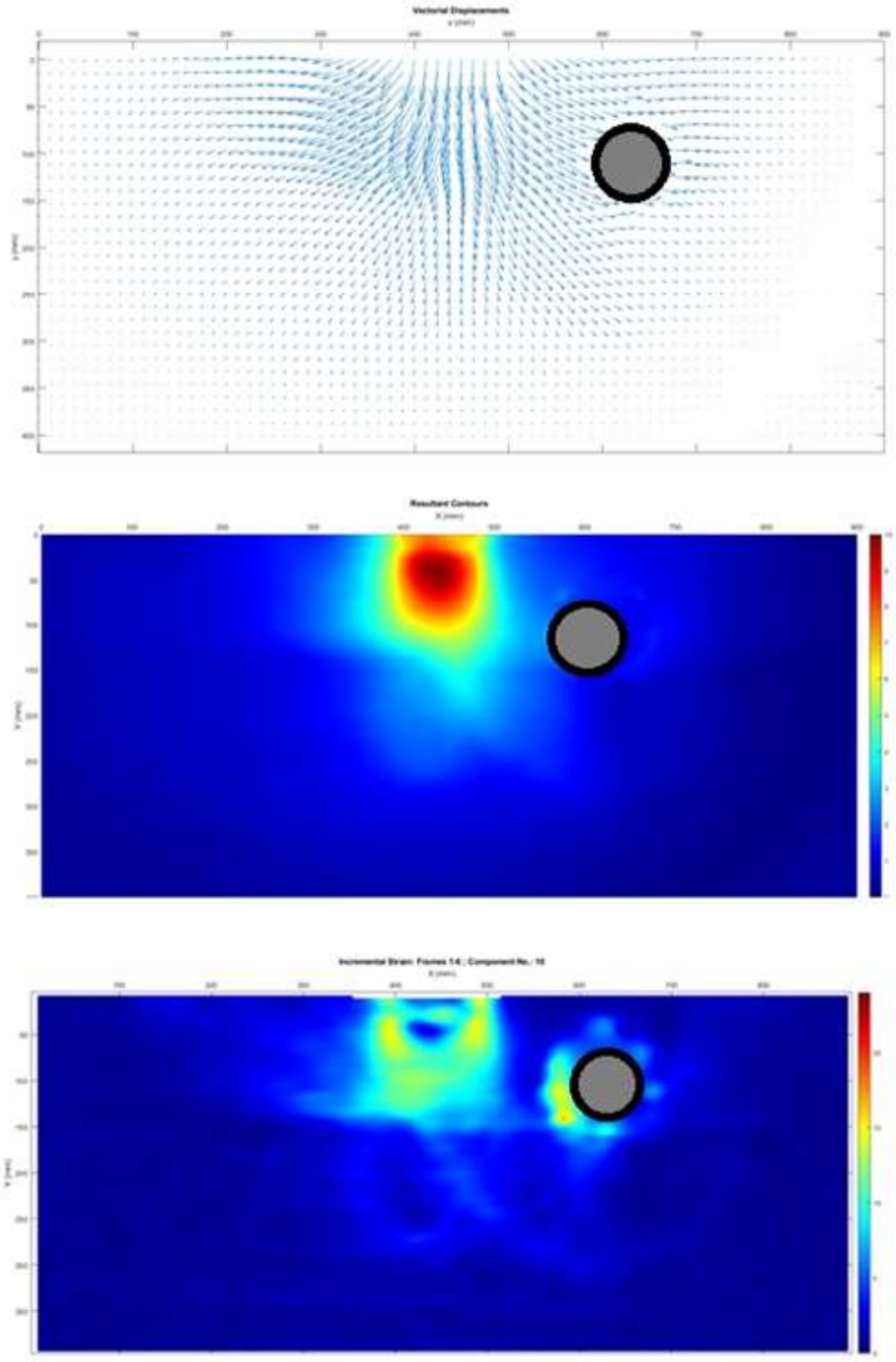


Figure 4.30. Vectorial displacement vectors, resultant displacement contours and shear strain contours at S/B=10% (10mm) vertical model footing settlement for T11.

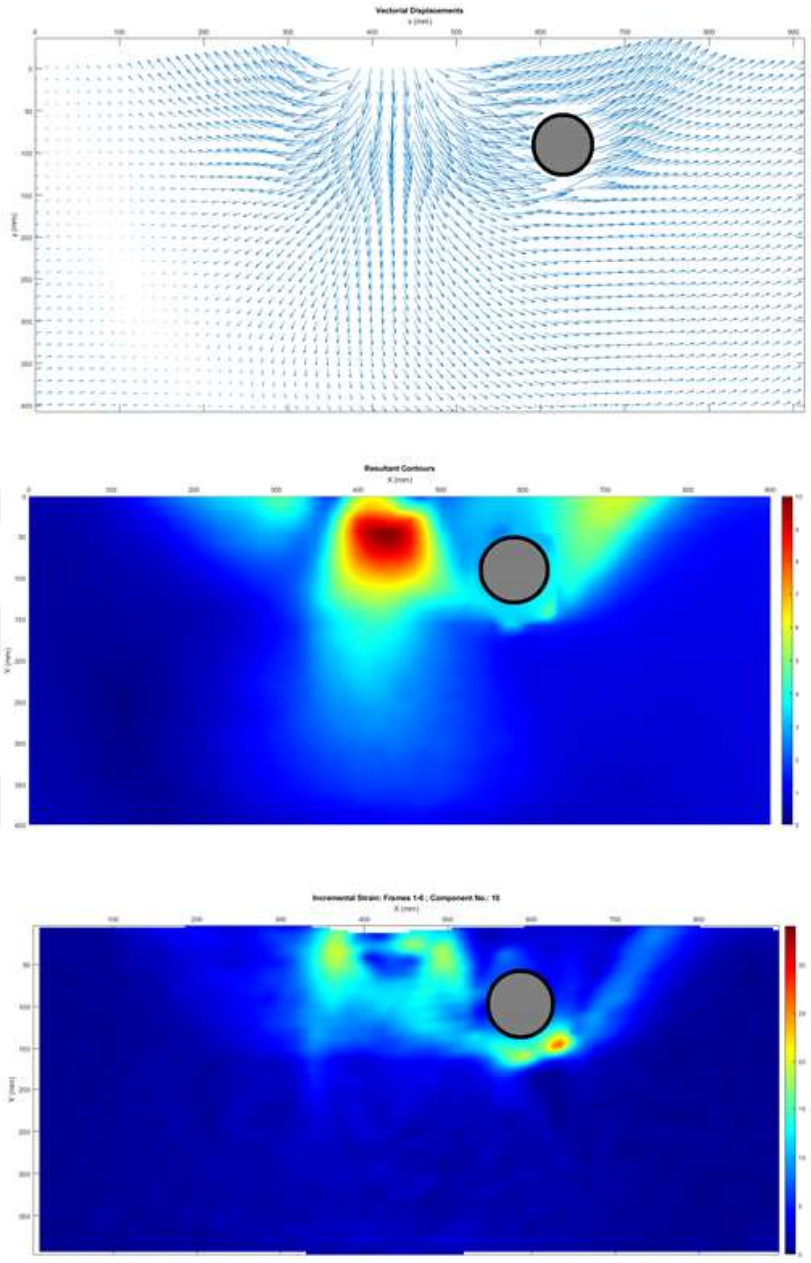


Figure 4.31. Vectorial displacement vectors, resultant displacement contours and shear strain contours at S/B=10% (10mm) vertical model footing settlement for T14.

It can be understood from PIV analysis that both of the general failure mechanisms can be seen under the model footing. On T11, soil movement occurred in the center; nevertheless, on T14, soil movement around the pipe can be identified. Furthermore, soil movement at the right side of the model test box only occurred on the T14 because the higher density resists higher loads, which creates upward soil movement to the right side. This result may be caused by a void that the pipe creates on

the right side of the text box. Not having an equal amount of soil on the right side with high base pressure may create right-upward movement on the dense soil. When soil displacement paths are examined, the soil of T11 is mostly displaced downward at the center, which is a similar displacement path to the T1 (without pipe) model test. With increasing relative density, the presence of the pipe affected soil displacement by concentrating on the right side of the model test box.

When shear strain contours are evaluated, it can be seen that the soil of the T11 model test has a bigger shear strain distribution on the crown of the pipe. However, the soil of T14 experienced more shear strain just below the pipe. Furthermore, when shear strain paths are examined, it can be seen that the soil of the T14 model test experienced shear strain starting from the below of the pipe to the top of the test box, which is relevant to the PIV displacement results. The soil of the T11 model test experienced more shear strain at the center area; nevertheless, in T14, shear strain distribution leans towards the pipe and less strain occurs at the center area.

For Comparison 5, firstly, base pressure-model footing settlement results are discussed. In Figure 4.32 base pressure values are normalized, as explained in the previous section (Section 4.1.1.1.). Ultimate base pressures and model footing settlement ratios for the model tests in Comparison 5 are given in Table 4.13.

Table 4.13. Ultimate base pressure values (q_u), model footing settlement ratios and pipe location for comparison 5 model tests.

Model Test	q_u**(kPa)**	**H/B**	**S/B(%)**	D_r**(%)**	**x/B**
T12	41.35	1.5	10	35	1.5
T15	88.84		10	65	

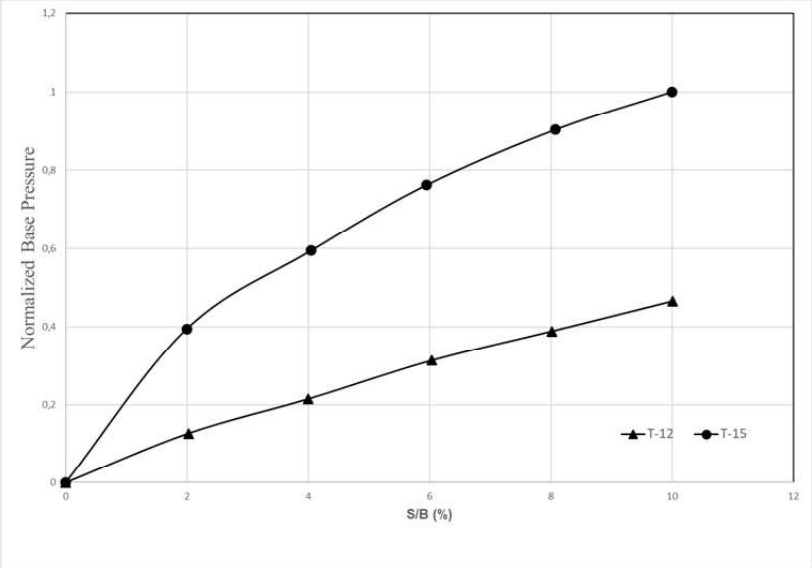


Figure 4.32. Normalized base pressure-model footing settlement ratios for T12 and T15.

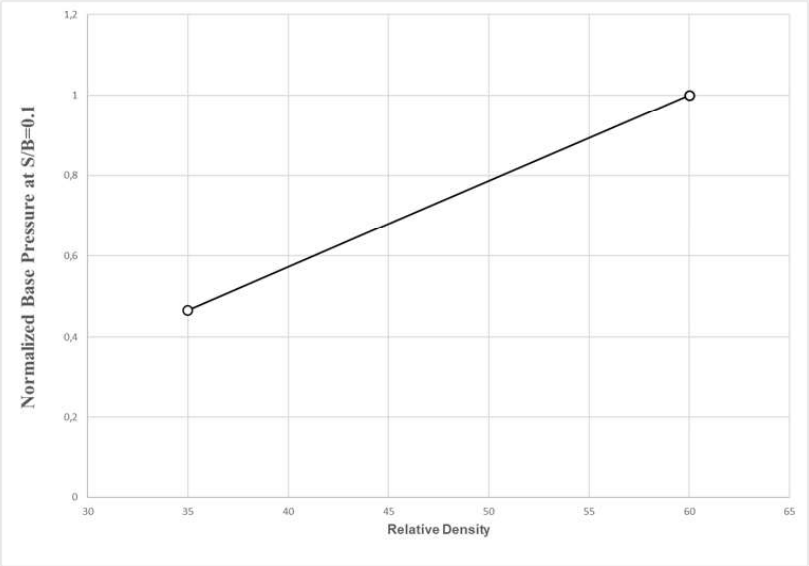


Figure 4.33. Normalized ultimate base Pressure-model footing settlement ratios for T12 and T15.

Figure 4.33 indicates that, at S/B = 0.1, T12 reached almost 45% of T15. This result is also coherent with the other comparisons, as expected. Ultimate base pressure difference occurred due to having different relative densities in soils, but this difference changes with the pipe location and will be discussed in a further section.

Ultimate base pressure on model footing, stress values acting on the pipe and stress ratio between for S/B=0.1 can be seen in Table 4.12 for the Comparison 5 model tests.

Table 4.14. Ultimate base pressure values, pipe stress values and stress ratios at S/B=0.1 for comparison 5 model tests.

Model Test	**Q (kPa)**	s_c **(kPa)**	s_R **(kPa)**	s_L **(kPa)**	S_{RC}	S_{RR}	S_{RL}
T12	41.35	0.36	-0.48	-0.48	0.0087	0.0116	0.0116
T15	88.84	1.14	-1.32	-1.92	0.0123	0.0148	0.0216

When Table 4.10 is examined, it can be seen that with higher relative density, stress ratios increased for left and right strain. For the T15 model test, the stress ratio for the left side strain is the highest one it could be because the left side strain is the closest one to the center of the footing. Stress ratios for crown location are almost the same for both tests; nevertheless, for the right and left sides, stress ratios are higher in the T15 due to having higher load transfer for the buried pipe's sides. Furthermore, it can be seen that in both of the tests, the crown of the pipe experienced tension; nevertheless, the sides of the pipes experienced compression. For the T12 model test, stress ratios of the right and left sides of the pipe; nevertheless, in the T15 model tests, they are different because the dense soil of T15 transmitted more load to the closer side of the model footing, which creates more stress on the pipe.

For Comparison 5, secondly, PIV analysis results are discussed. PIV results for Comparison 5 model tests are shown in Figure 4.34 and Figure 4.35. General failure mechanisms for both model tests can be seen when PIV analysis is examined.

There is almost no soil movement observed around the buried pipe in the T12 model test; nevertheless, for the T15 model test, soil located at the upper left side of the pipe experienced displacement due to having a larger load coming from the model footing. With a larger load coming from the model footing at the center, dense soil moved toward the upper side of the test box, as can be seen in Figure 4.35.

Furthermore, it can be understood that soil displacement distribution is more widely in the T12 model test because of its loose state.

Moreover, when the PIV analysis of T15 was examined, it can be seen that dense soil particles located on the left side of the center of the footing also experienced displacement, but for the T12 model test, there was no soil displacement in regions outside of the center. It can be seen that the PIV analysis resultant contours for T12 are almost identical to the T1. Nevertheless, PIV analysis resultant contours for T15 have visible differences according to the T3. These results show that, with increasing relative density, the presence of buried pipe affected soil displacement contours and paths more widely.

When shear strain contours are evaluated, it can be seen that the dense soil of T15 experienced more shear strain than the loose soil of T12 at the center of the test box. It can be understood that, just below the model footing at the center, both soils have experienced almost no shear strain. Around the pipe, the soil of T15 experienced more shear strain than the soil of T12. Furthermore, when Figure 4.35 is examined, it can be seen that dense soil located on the upper side of the buried pipe experienced more shear strain than dense soil located below the pipe.

Shear strain distribution is different for both tests; dense soil has experienced more shear strain for this comparison due to having higher relative density. For T12, displacement contours concentrated on the center; nevertheless, shear strain contours concentrated on the two sides of the model footing, not reaching around the pipe. For T15, both displacement contours and shear strain contours reach the pipe location and affect the pipe.

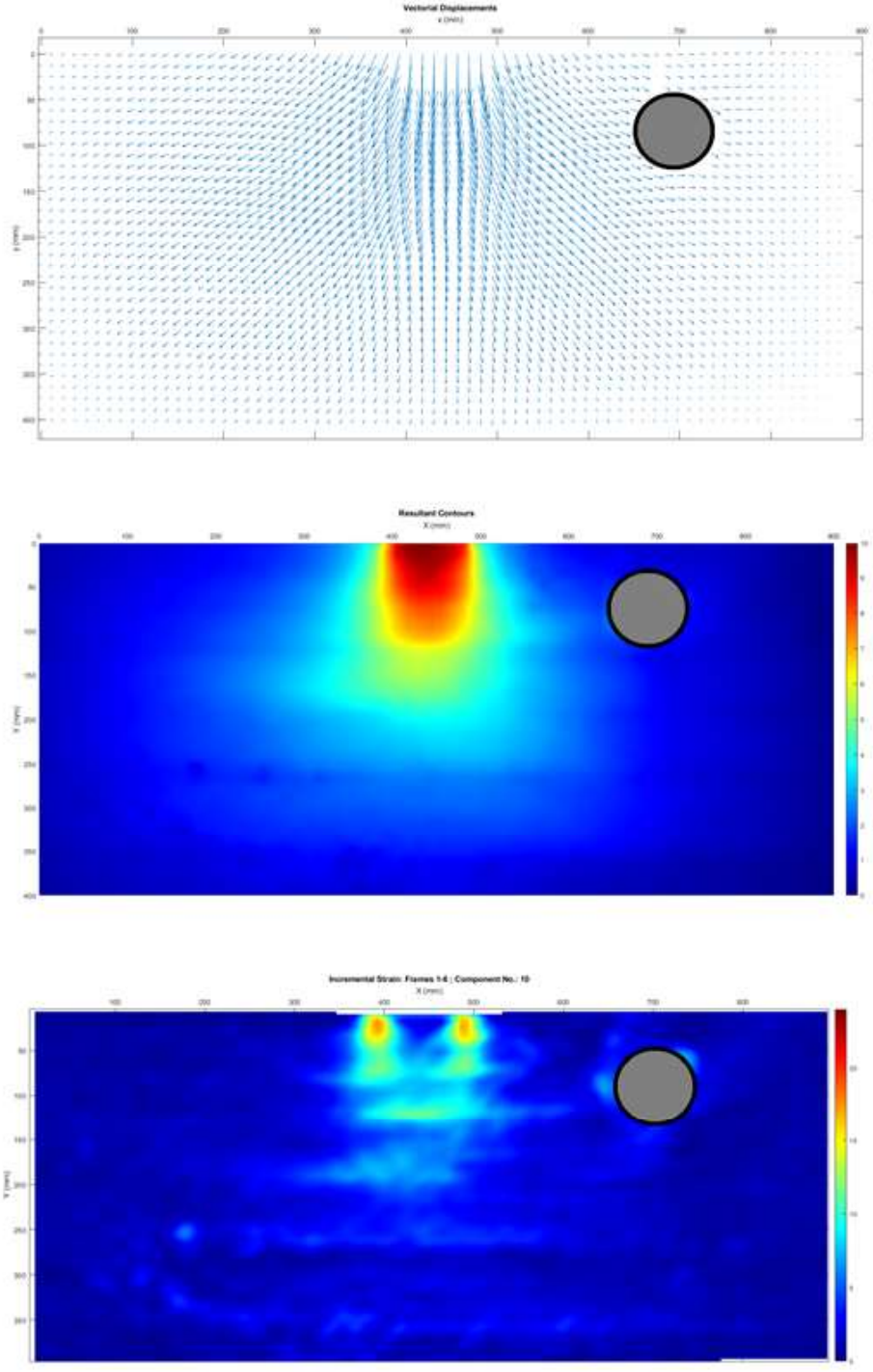


Figure 4.34. Vectorial displacement vectors, resultant displacement contours and shear strain contours at S/B=10% (10mm) vertical model footing settlement for T12.

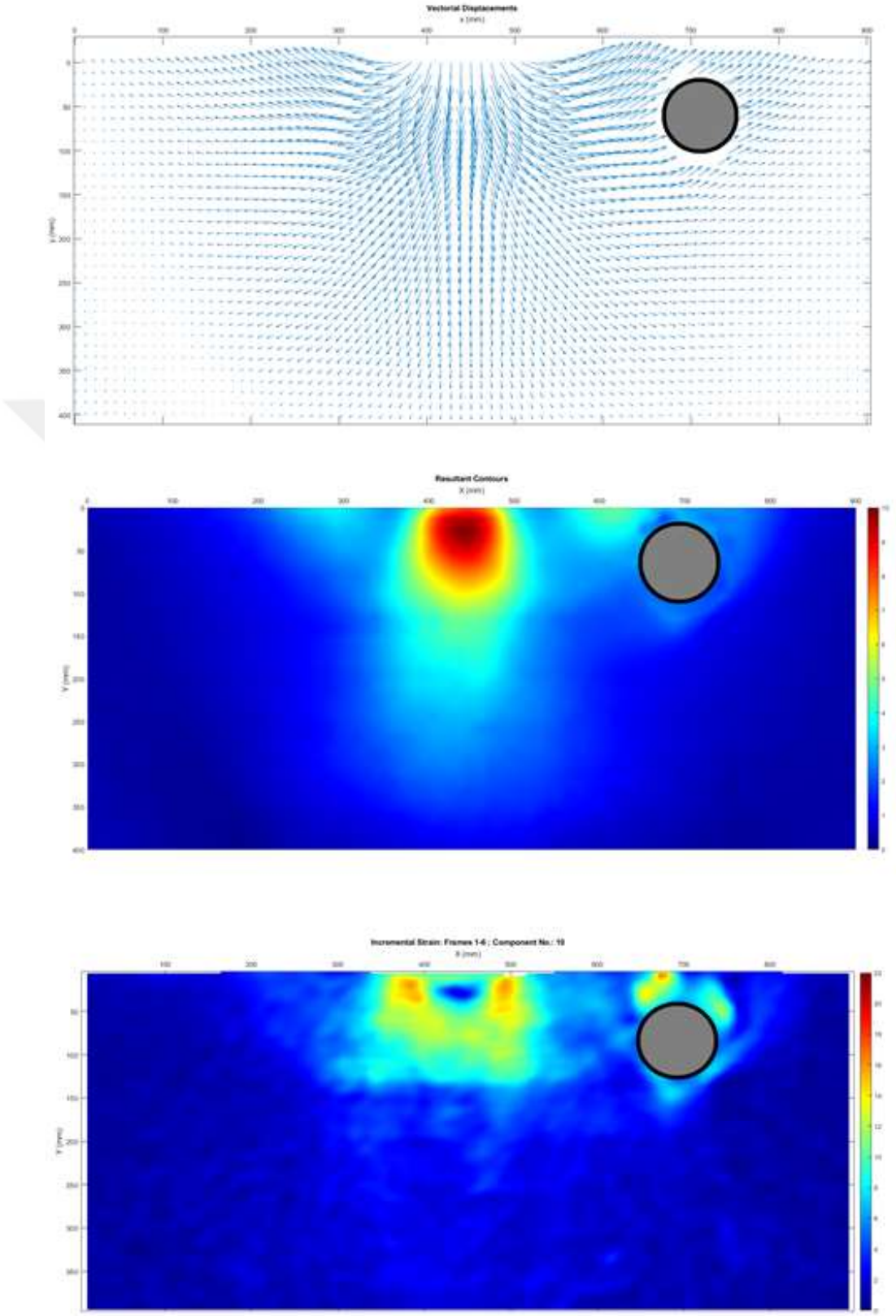


Figure 4.35. Vectorial displacement vectors, resultant displacement contours and shear strain contours at S/B=10% (10mm) vertical model footing settlement for T15.

4.2. Pipe Location Effect on Bearing Capacity and Soil Displacement

In this section, the buried pipe location effect on bearing capacity and soil displacement is discussed. The location effect was examined by considering both the burial depth and the horizontal distance from the center. As in the previous section, the results will be analyzed in two parts. Base pressure values normalized according to the pressure values at S/B=10% model footing settlement of the model tests without the pipe. In order to understand the buried pipe location effect, the relative density of soils and either buried depth or the horizontal distance between the outer left side of the pipe and the right end of the model footing will be constant and results will be compared as groups. The results of all model tests will be used in this section. Test setups of the model tests not shown previously (T16, T17 and T18) can be seen in Figure 4.36.

4.2.1. Burial Depth Effect (D_r=35%)

In order to investigate the burial depth effect on bearing capacity and soil displacement at 35% relative density (loose state), three model tests were conducted with constant relative density and buried pipes located in the center of the test box with different burial depths, which are shown as Comparison 6 in Table 4.15. Normalized base pressures and ultimate normalized base pressures are shown in Figure 4.37 and Figure 4.38.

Table 4.15. Ultimate base pressure values (q_u), model footing settlement ratios and pipe locations for comparison 6 model tests.

Model Test	q_u**(kPa)**	D_r**(%)**	**H/B**	**x/B**	**Comparison No.**
T1	43.61	35		-	6
T2	32.25		0.75		
T3	48.95		1.5		

From Figure 4.37 and Figure 4.38, it can be understood that for 35% relative density, the bearing capacity of soil increases with the increasing burial depth. At T2, the ultimate base pressure is equal to 76% of the T1 and 112% of the T1 in the T3. These results can be interpreted as the bearing capacity of soil not being affected if the pipe is placed far enough in the geometrical properties that have been used in the model tests. Furthermore, it can be seen that, until S/B=2%, the presence of the pipe positively affected the bearing capacity of the soil.

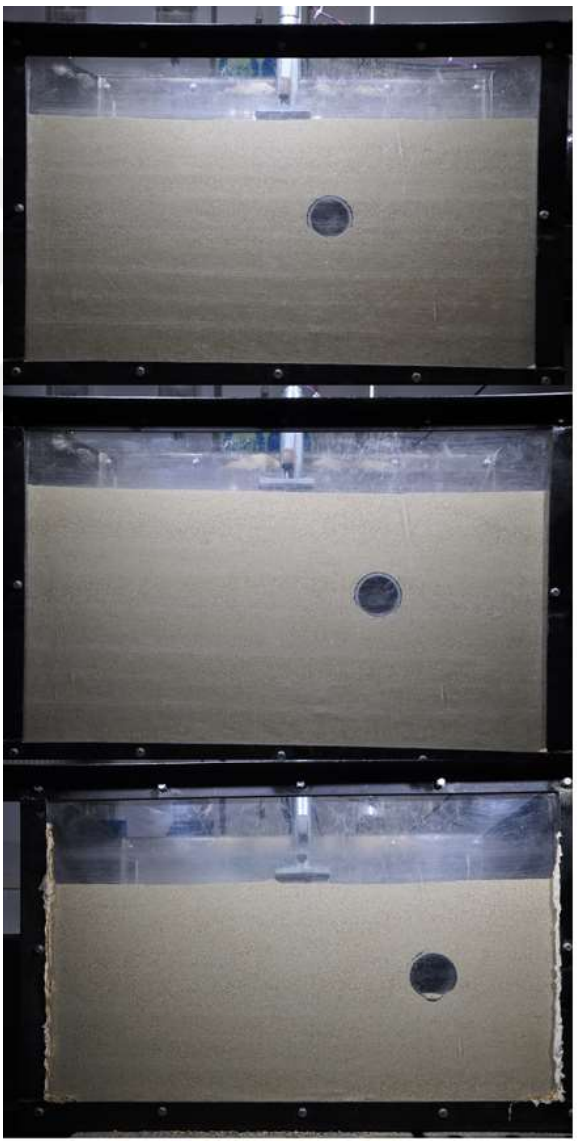


Figure 4.36. Test setups of T16, T17 and T18, respectively.

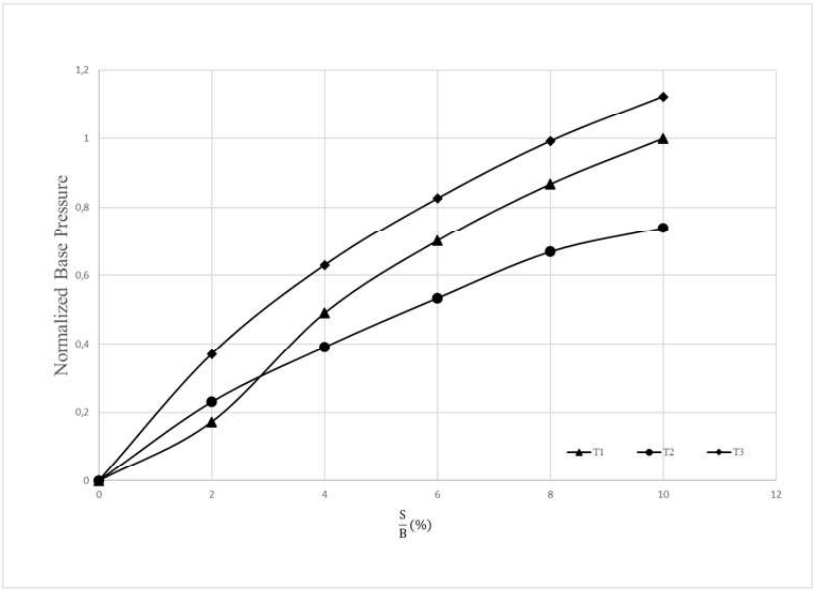


Figure 4.37. Normalized base pressure-model footing settlement ratios for T1, T2 and T3.

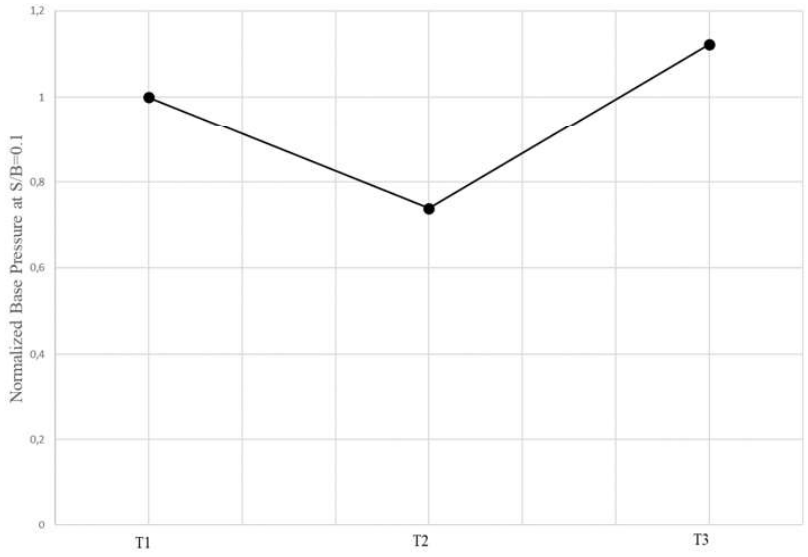


Figure 4.38. Normalized ultimate base pressure-model footing settlement ratios for T1 T2 and T3.

When PIV results (Figure 4.5, Figure 4.16 and Figure 4.21) of Comparison 6 model tests are examined, it can be seen that buried pipe limits resultant displacement contours. When T2 and T3 are compared to each other, it can be understood that the resulting displacement contours reached under the pipe for T2; nevertheless, almost

all soil displacement in T3 occurred above the pipe. In shear strain contours, the soil of T2 experienced more shear strain below the pipe than the soil of T3. Furthermore, above the pipe, the soil of T2 has more shear strain distribution due to the buried pipe being closer to the model footing.

4.2.2. Horizantal Distance Effect (D_r=35 H/B=0.75)

In order to investigate the horizontal distance from the center effect on bearing capacity and soil displacement at 35% relative density (loose state), five model tests were conducted with constant relative density and constant burial depth, which is shown in Comparison 7 in Table 4.16. Normalized base pressures and ultimate normalized base pressures are shown in Figure 4.39 and Figure 4.40.

Table 4.16. Ultimate base pressure values (q_u), model footing settlement ratios and pipe locations for comparison 7 model tests.

Model Test	q_u**(kPa)**	D_r**(%)**	**H/B**	**x/B**	**Comparison No.**
T1	43.61		-	-	
T2	32.25	-	0.75		
T10	29.40		0.75	0	
T11	34.38	35	0.75	0.75	7
T12	41.35		0.75	1.5	

When, Figure 4.39 and Figure 4.40 are examined, it can be understood that for 35% relative density, the bearing capacity of soil increases with the increasing horizontal distance from the center after x/B=0. At T12, which is the farthest from the center, the ultimate base pressure at S/B=10% corresponds to 94% of the T1. Nevertheless, the ultimate base pressure at S/B=10% at T2 is bigger than T10, which means that if the buried pipe is placed just near the end of the model footing at H/B=0.75, bearing capacity decreases. Also, until S/B=2%, the soil of the T1 model test could not resist too much pressure and then it started to resist. This may be due to having no pipe.

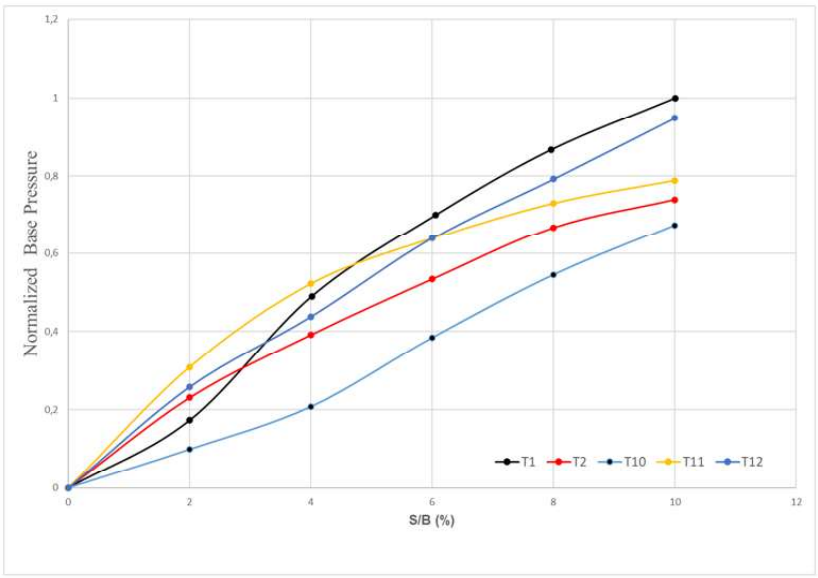


Figure 4.39. Normalized base pressure-model footing settlement ratios for T1, T2, T10, T11 and T12.

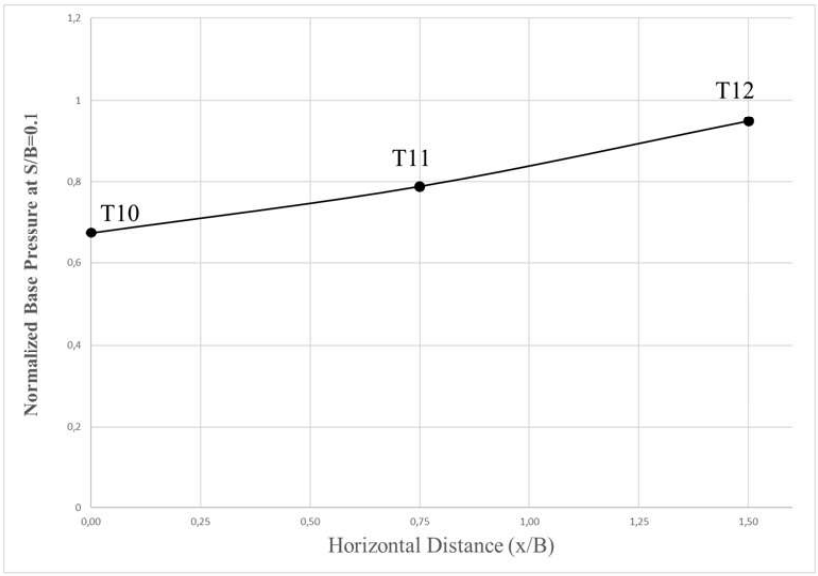


Figure 4.40. Normalized ultimate base pressure-model footing settlement ratios for T10 T11 and T12.

When PIV results (Figure 4.5, Figure 4.16, Figure 4.26, Figure 4.30 and Figure 4.34) of Comparison 7 model tests are examined, it can be seen that increased horizontal distance of buried pipe from the center reduces the effect of buried pipe on soil displacement. It can be understood that there is almost no soil displacement under

the buried pipe for the $x/B0$ model tests. When the T1, T11 and T12 model tests' PIV results are compared to each other, it can be understood that they have the same pattern of soil displacement because buried pipe has almost no effect on soil displacement when x/B=1 in loose state (D_r: 35) model tests. Also, an increased horizontal distance of buried pipe from the center increases the distribution of shear strain that soil experiences.

4.2.3. Burial Depth Effect (D_r= 50%)

In order to investigate the burial depth effect on bearing capacity and soil displacement at 50% relative density (medium-dense state), three model tests were conducted with constant relative density and buried pipes located in the center of the test box with different burial depths, which are shown as Comparison 8 in Table 4.17. Normalized base pressures and ultimate normalize base pressures are shown in Figure 4.41 and Figure 4.42.

Table 4.17. Ultimate base pressure values (q_u), model footing settlement ratios and pipe locations for comparison 8 model tests.

Model Test	q_u**(kPa)**	D_r**(%)**	**H/B**	**x/B**	**Comparison No.**
T4	74.25	50	-	-	8
T5	68.17		0.75		
T6	73.70		1.5		

It can be understood from the Figure 4.41 and Figure 4.42 that the bearing capacity increases with the increasing burial depth and approximates the bearing capacity that T4 has. At T6, the ultimate base pressure is 99% of the T4 and 108% of the T5. Although, until S/B=2%, T5 and T6 behaved almost the same curve, after S/B=2%, T6 resisted more load at the same amount of displacement. This result may be caused by increased burial depth.

When PIV results (Figure 4.6, Figure 4.17 and Figure 4.22) of Comparison 8 model tests are examined, it can be seen that soil displacements concentrated around the pipe and for both T5 and T6, soil displacement contours can be seen below the buried pipe. Furthermore, shear strain contours were concentrated on the crown of the pipe.

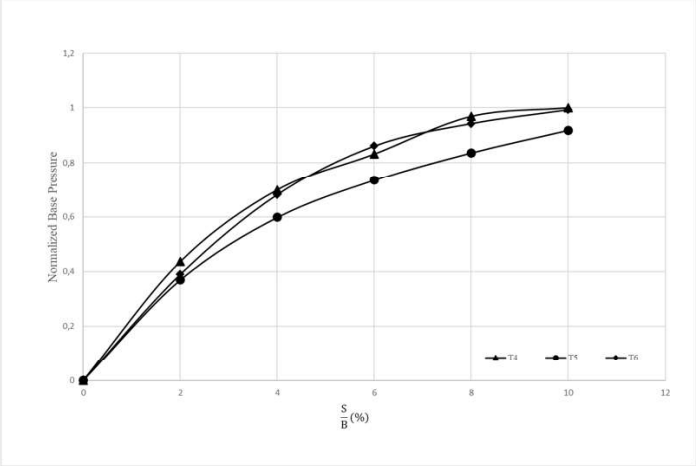


Figure 4.41. Normalized base pressure-model footing settlement ratios for T4, T5, and T6.

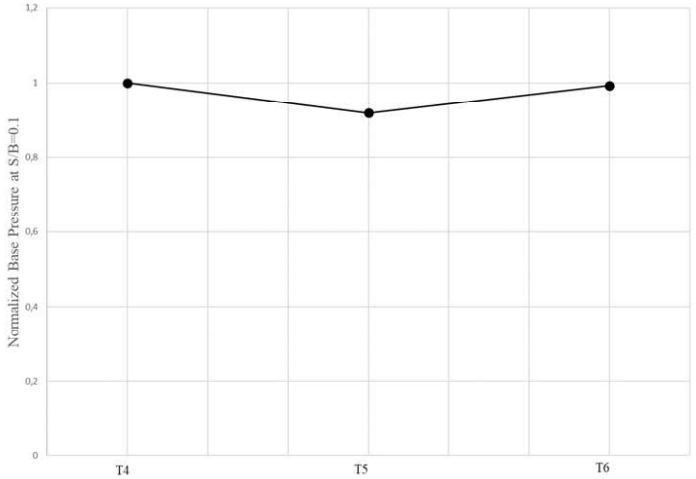


Figure 4.42. Normalized ultimate base pressure-model footing settlement ratios for T4, T5 and T6.

4.2.4. Burial Depth Effect (D_r= 65%)

In order to investigate the burial depth effect on bearing capacity and soil displacement at 65% relative density (dense state), three model tests were conducted with constant relative density and buried pipes located in the center of the test box with different burial depths, which are shown as Comparison 9 in Table 4.11. Normalized base pressures and ultimate normalized base pressures are shown in Figure 4.43 and Figure 4.44.

Table 4.18. Ultimate base pressure values (q_u), model footing settlement ratios and pipe locations for comparison 9 model tests.

Model Test	q_u**(kPa)**	D_r**(%)**	**H/B**	**x/B**	**Comparison No.**
T7	95.12	65	-	-	9
T8	75.40		0.75		
T9	77.31		1.5		

Figure 4.43 and Figure 4.44 show that, for Comparison 9, the bearing capacity of soil did not increase with the increasing burial depth as much as in Comparison 6 and 8. At T9, the ultimate base pressure is 81% of the T4 and 102% of the T5. It can be understood from Figure 4.43 that normalized base pressure-model footing settlement curves for both T7 and T9 behaved almost similarly until the S/B=8%, the soil of T9 experienced failure, which reduced the bearing capacity. At S/B=2%, T9 resisted much more pressure than other model tests, although this resistance from the beginning resulted in bearing capacity failure at S/B=8%. This result may be due to the void created by the buried pipe, which is placed relatively further away from the model footing in dense soils.

When PIV results (Figure 4.7, Figure 4.18 and Figure 4.23) of Comparison 9 model tests are examined, it can be seen that almost no soil displacement occurred below the buried pipe. It can be understood from the resultant displacement contours that soil displacement is less than according to Comparisons 6 and 8. For T7 and T9, the general failure mechanism of the soil can be seen clearly; it cannot be seen for T8

due to the presence of a pipe. Shear strain contours show that, around the pipe, the soil of T9 experienced more shear strain than the soil of T8. Furthermore, increasing buried depth increased the shear strain distribution for Comparison 9 model tests.

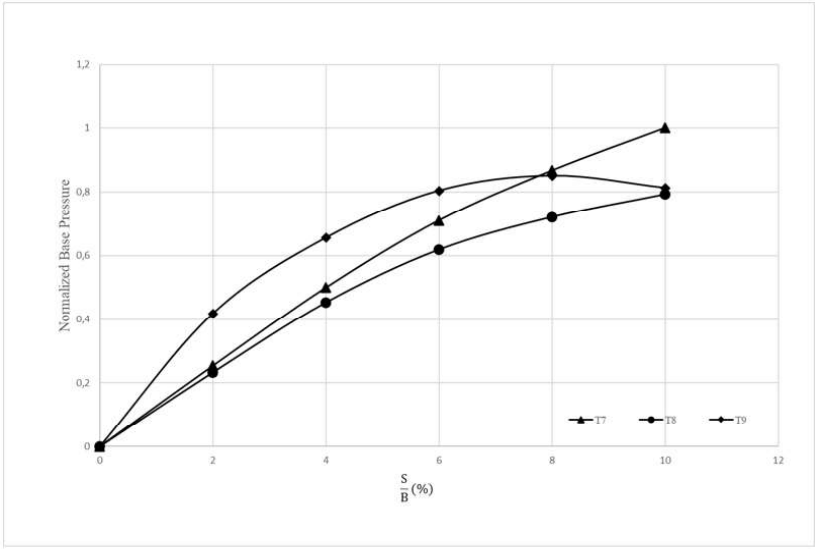


Figure 4.43. Normalized base pressure-model footing settlement ratios for T7, T8, and T9.

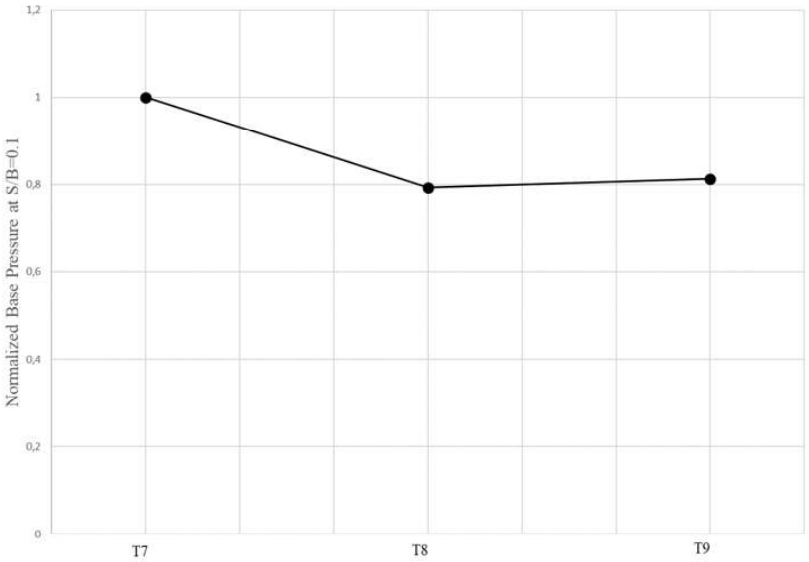


Figure 4.44. Normalized ultimate base pressure-model footing settlement ratios for T7, T8 and T9.

4.2.5. Horizantal Distance Effect (D_r= 65%, H/B= 0.75)

In order to investigate the horizontal distance from the center effect on bearing capacity and soil displacement at 65% relative density (dense state), five model tests were conducted with constant relative density and constant burial depth (H/B=0.75), shown as Comparison 10 in Table 4.19. Normalized base pressures and ultimate normalized base pressures are shown in Figure 4.45 and Figure 4.46.

Table 4.19. Ultimate base pressure values (q_u), model footing settlement ratios and pipe locations for comparison 10 model tests.

Model Test	q_u**(kPa)**	D_r**(%)**	**H/B**	**x/B**	**Comparison No.**
T7	95.12	65	-	-	10
T8	75.40		0.75	-	
T13	68.16		0.75	0	
T14	70.72		0.75	0.75	
T15	88.72		0.75	1.5	

When, Figure 4.45 and Figure 4.46 are examined, it can be understood that for 65% relative density, the bearing capacity of soil increases with the increasing horizontal distance from the center after x/B=0 for H/B=0.75. At T15, which is the farthest from the center, the ultimate base pressure at S/B=10% corresponds to 93% of the T7. Nevertheless, ultimate base pressure at S/B=10% at T8 is bigger than both T13 and T14, which means that if the buried pipe is placed horizontally further from x/B= 0.75, bearing capacity starts to increase for the buried pipe case. Also, until S/B=2%, the soil of the T7 model test could not resist as much pressure as T14 and T15, but then it started to resist more pressure than T14 and T15; this may be due to having no pipe. Moreover, T14 and T15 normalized base pressure-model footing settlement ratio curves behaved similarly until the S/B=4%. After that point, T14 experienced a decrease in bearing capacity.

When PIV results (Figure 4.7, Figure 4.18, Figure 4.27, Figure 4.31 and Figure 4.35) of Comparison 10 model tests are examined, it can be seen that the general failure mechanism can be clearly seen in PIV results of T14 and T15. Furthermore, with increasing horizontal distance from the center, soil displacement was observed at the upper right and upper left side of the text box. This situation can also be supported by examining the vectorial displacement contours for the Comparison 10 model tests. When shear strain contours are examined, it can be understood that, with increasing horizontal distance, soil located around the pipe experienced more shear strain.

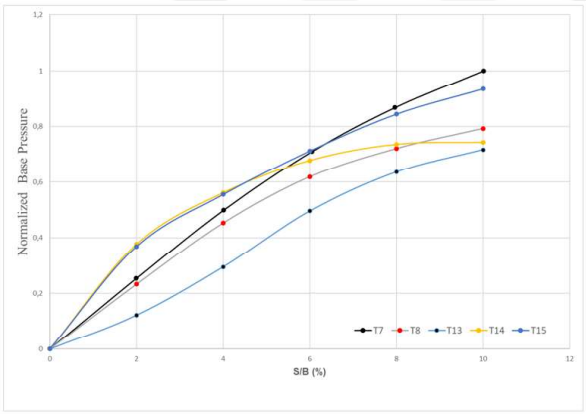


Figure 4.45. Normalized base pressure-model footing settlement ratios for T7, T8, T13, T14 and T15.

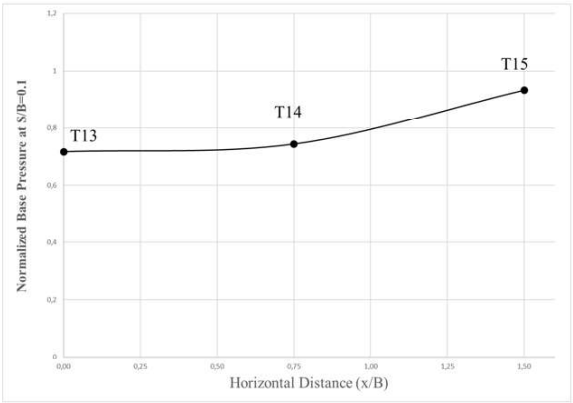


Figure 4.46. Normalized ultimate base pressure-model footing settlement ratios for T7, T8, T13, T14 and T15.

4.2.6. Horizantal Distance Effect (D_r = 65%, H/B = 1.5)

In order to investigate the horizontal distance from the center effect on bearing capacity and soil displacement at 65% relative density (dense state), five model tests were conducted with constant relative density and constant burial depth (H/B=1.5), which is shown as Comparison 11 in Table 4.20. Normalized base pressures and ultimate normalized base pressures are shown in Figure 4.47 and Figure 4.48. PIV results of the model tests (T16, T17, and T18) that were not presented in previous sections are shown in Figure 4.49, Figure 4.50 and Figure 4.51.

Table 4.20. Ultimate base pressure values (q_u), model footing settlement ratios and pipe locations for comparison 11 model tests.

Model Test	q_u**(kPa)**	D_r**(%)**	**H/B**	**x/B**	**Comparison No.**
T7	95.12	65	-	-	11
T9	75.40		1.5	-	
T16	86.47		1.5	0	
T17	79.96		1.5	0.75	
T18	89.78		1.5	1.5	

Figure 4.48 are examined, it can be understood that for 65% relative density, the bearing capacity of soil increases if the buried pipe is placed horizontally away from the center. At T18, which is the farthest from the center, the ultimate base pressure at S/B=10% corresponds to 94% of the T7. Nevertheless, the ultimate base pressure at S/B=10% at T16 is bigger than T9, which means that if the buried pipe is placed horizontally further from x/B=0, the soil has more bearing capacity according to the placing buried pipe on the center. Nevertheless, for Comparison 11, the bearing capacity of soil does not increase linearly as placing the pipe horizontally away further from the center. At T17, the ultimate base pressure at S/B=10% corresponds to 84% of the T7, which is a smaller normalized base pressure according to the T16.

When PIV results (Figure 4.7, Figure 4.23, Figure 4.49, Figure 4.50 and Figure 4.51) of Comparison 11 model tests are examined, general failure mechanisms can be

seen clearly for horizontally placed model tests. Besides T16, the soil of model tests did not experience notable displacement. Furthermore, the PIV results of T7 and T18 are almost similar to each other. According to those results, it can be said that buried pipe has almost no effect on soil displacement at H/B=1.5, x/B=1.5. Shear strains mostly concentrated on the center; with increasing horizontal distance, the soil around the pipe did not experience notable shear strains.

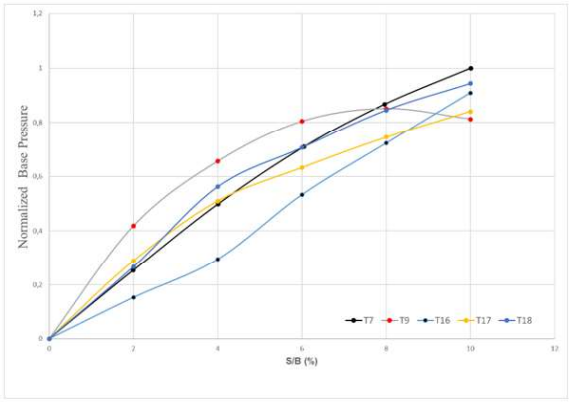


Figure 4.47. Normalized base pressure-model footing settlement ratios for T7, T9, T16, T17 and T18.

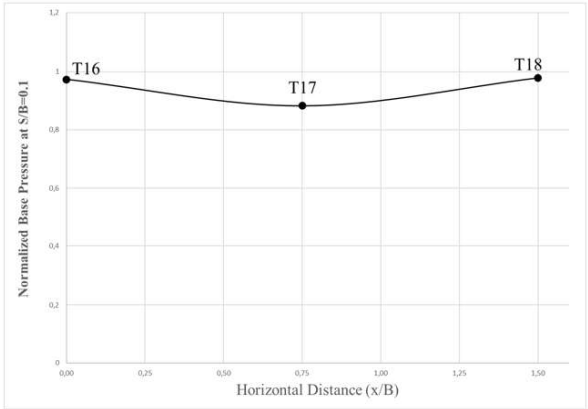


Figure 4.48. Normalized ultimate base pressure-model footing settlement ratios for T16, T17 and T18.

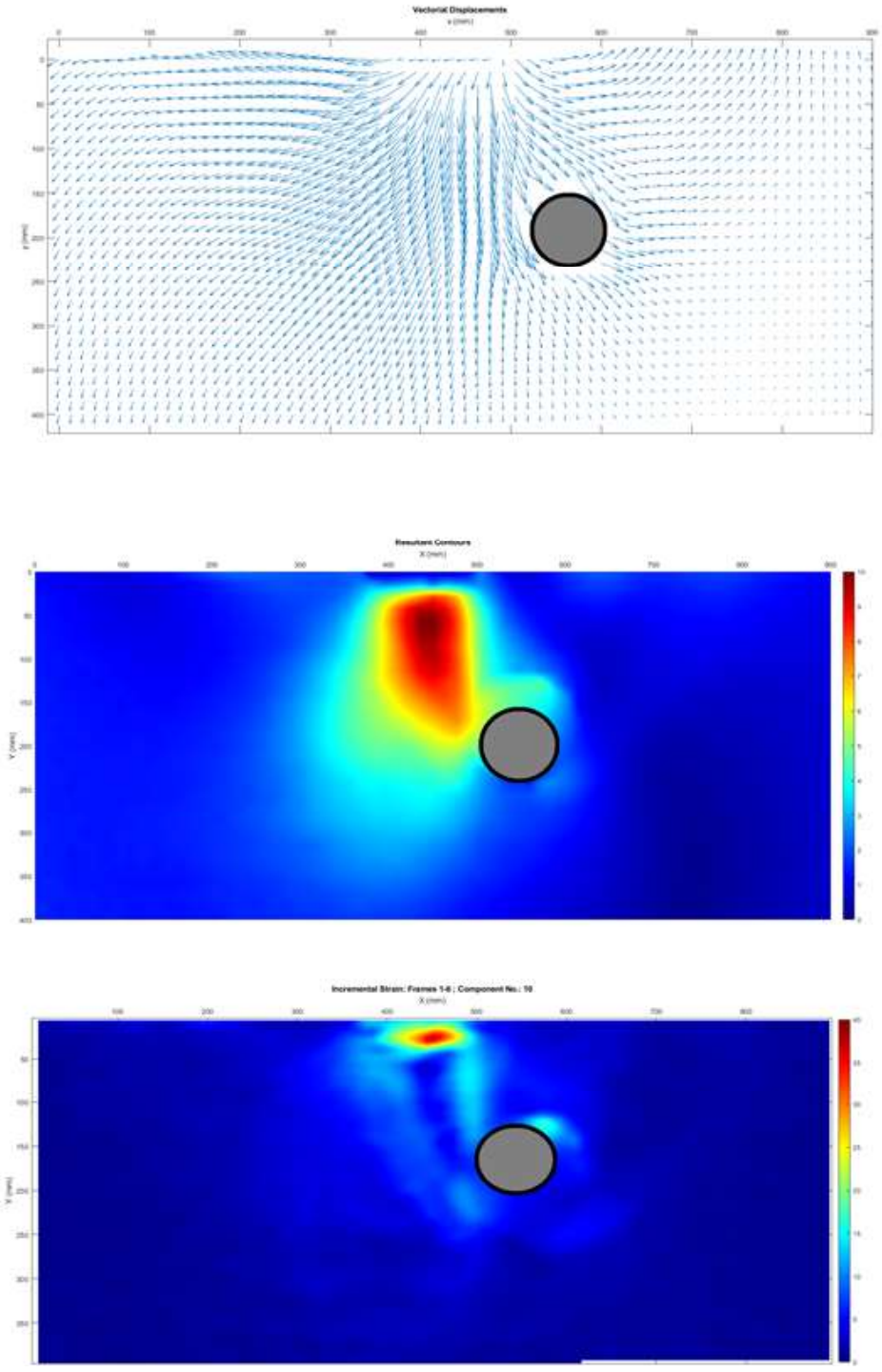


Figure 4.49. Vectorial displacement vectors, resultant displacement contours and shear strain contours at S/B=10% (10mm) vertical model footing settlement for T16.

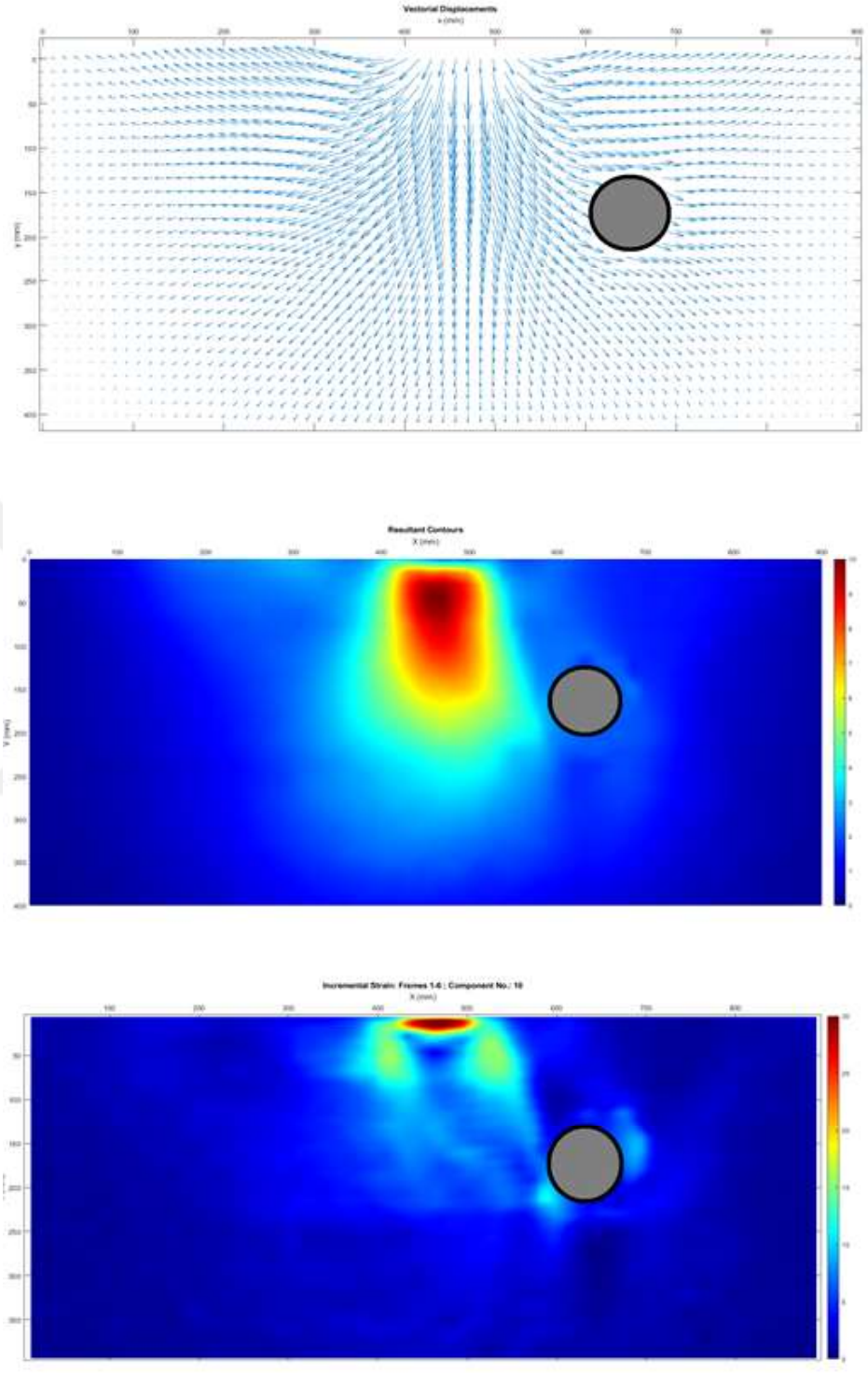


Figure 4.50. Vectorial displacement vectors, resultant displacement contours and shear strain contours at S/B=10% (10mm) vertical model footing settlement for T17.

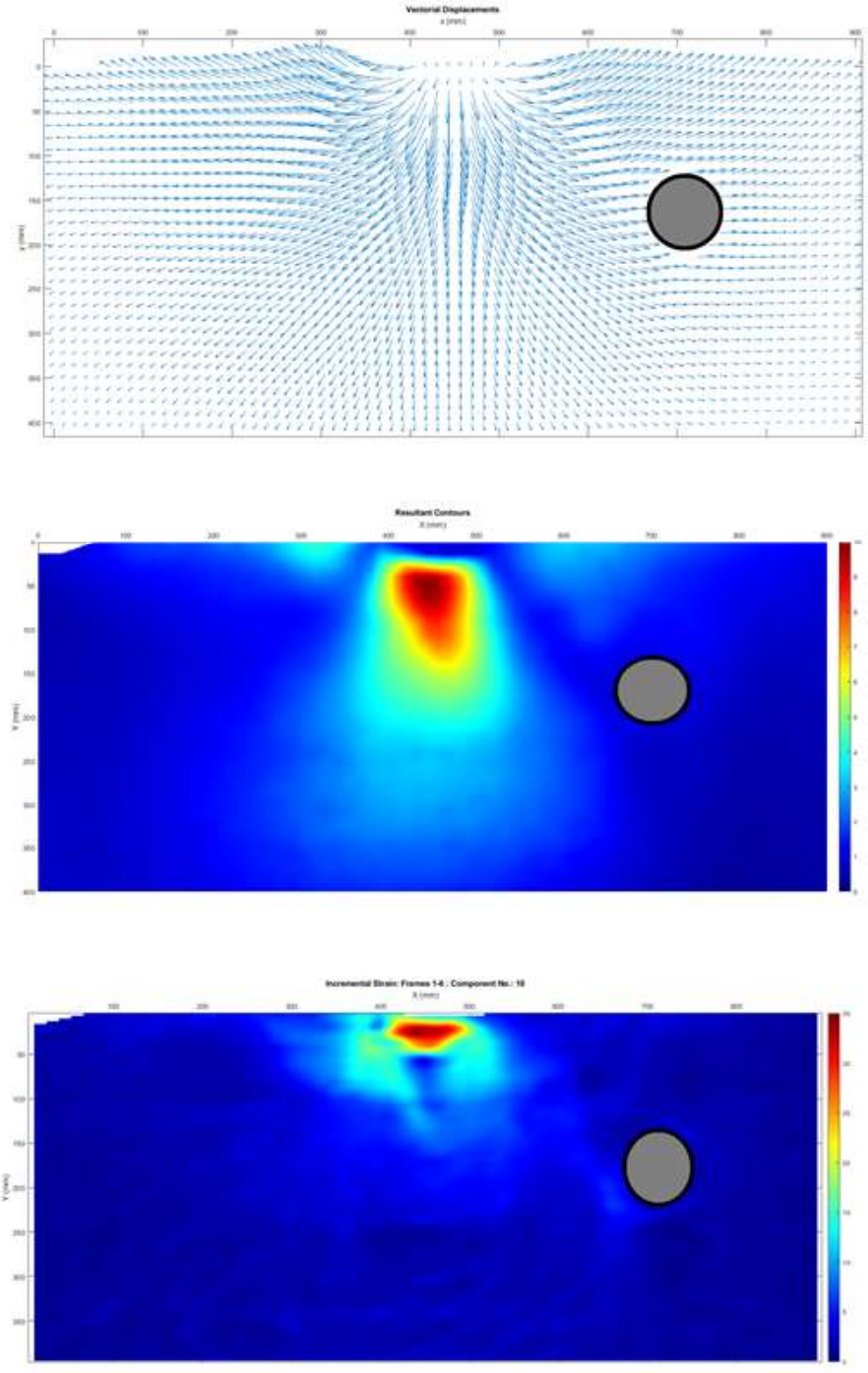


Figure 4.51. Vectorial displacement vectors, resultant displacement contours and shear strain contours at S/B=10% (10mm) vertical model footing settlement for T18.

5. DISCUSSION

First and foremost, this study revealed how image analysis improves the understanding of physical model tests when it is used in a well-structured way. Almost all of the measurements obtained from load cells, strain gauges and LVDT became more clear when it was supported by the results of image analysis.

In this section, all the findings are discussed. Firstly, the relative density effect on bearing capacity and soil displacement was examined with the model tests. Five comparison has been done with 15 model tests. The most crucial thing to say about these results is that increasing relative density creates a higher bearing capacity of backfill soil. According to the results of Comparison 1 and 2, in comparison 1, loose backfill soil has 40 percent of the bearing capacity of dense backfill soil, while in comparison 2, loose backfill soil has 60 percent of the bearing capacity of dense backfill soil. This shows that, in terms of bearing capacity, the relative density effect decreases as the burial depth increases. Also, these results indicate that if the compaction cost is higher, burying the pipe can be the more economical solution when the pipe is located under the center of the foundation. Moreover, according to the PIV results, increased relative density leads to the formation of general shear failure. In terms of pipe stresses, in both comparisons 1 and 2, the medium-dense backfill soil had the highest stress ratios, which means that medium-dense soil transferred a relatively higher load to the pipe according to its base pressure, which is another criterion for buried pipe placement, according to the Comparison 3, 4 and 5, which are the comparison for the buried pipe horizontally offset from the center, bearing capacity increases with increasing relative density. Furthermore, increasing relative density made PIV results clearer for soil displacement and failure surfaces in the model tests with buried pipe horizontally offset from the center.

Secondly, the pipe location effect on bearing capacity and soil displacement was examined with the model tests. Six comparison has been done with 18 model tests in

order to investigate the pipe location effect. For loose soil states, increasing burial depth increases bearing capacity and it approximates the without pipe condition. Moreover, the general shear failure surface can be seen more clearly in PIV results with increasing burial depth for loose state backfill soil. Burial depth affects bearing capacity more in the dense state according to the loose state. According to the results, in a loose state, the backfill bearing capacity of the model test with H/B=1.5 is 112% of the bearing capacity without the pipe case. Nevertheless, in a dense state, the backfill bearing capacity of the model test with H/B=1.5 is 81% of the backfill bearing capacity without the pipe case. Therefore, with increasing relative density, the effect of burial depth gains more importance on bearing capacity. According to all the results, the safest approach is D_r= 65 at H/B=1.5 when taking into account normalized stresses and pipe stress ratios. The horizontal distance from the model footing is another location effect on bearing capacity and soil displacement. For all relative density states, increased horizontal distance from the model footing leads to an increase in bearing capacity. In a dense state, horizontal distance from the model footing at different burial depths affected bearing capacity almost equally rate. Furthermore, according to the PIV results, with increasing horizontal distance, the displacement of soil grains became more predictible.

Considering the results of all the studies in this thesis, increased burial depth, horizontal distance and higher relative density yielded better backfill bearing capacity, pipe pressure ratios and soil displacement prediction. Also, the results show that PIV analysis is an effective tool to visually present soil deformations and strains. Nevertheless, pipe placement must be done according to all aspects, like economy and needed bearing capacity. Sufficient bearing capacity selection must be done according to the loads and after that, pipe placement can be done with the necessary relative density and proper buried pipe location.

For the future studies, the soil improvement effect can be analyzed. Using geosynthetic reinforcement may increase bearing capacity and limit soil displacement; therefore, it can be studied. Nevertheless, there are various studies with geosynthetic re-

inforcement on buried pipes and most of them do not include image analysis. Furthermore, stresses acting on the geosynthetic reinforcement can be measured in future studies using strain gauges. Moreover, pipes with different diameters can be used in order to determine the effect of pipe size on bearing capacity and soil displacement patterns.

6. CONCLUSION

In this thesis, the aim is to investigate the effect of buried pipe location and relative density on the bearing capacity of used soil, stress acting on the buried pipes and the displacement of the backfill soil under surficial loading by using the image analysis method PIV. Various physical model tests were conducted using a test box within the scope of TUBITAK Project No. 116R020. The strain values of the buried pipes were measured by using strain gauges and strain measurements used to calculate pipe stresses. Base pressure acting on the model footing and settlement of the model footing was obtained using LVDT transducers and load cells. Image analysis of model tests was done via PIV modules, which are MATLAB-based. Results of image analysis and model tests were obtained for the purpose of comparison, evaluation and interpretation.

PIV analyses were examined and it was seen that the backfill soil around the pipe experienced shear strain regardless of the burial depth. Nevertheless, the same situation was not observed when the pipe was displaced horizontally. Suppose a buried pipe is placed at H/B=1.5, x/B=1.5; the soil around the pipe would not experience considerable shear strain. Furthermore, by using displacement contours, formed failure surfaces on backfill soil were observed.

From the data obtained from load cells and LVDT, it was observed that both location and relative density have a significant effect on bearing capacity and soil displacement patterns. First of all, the bearing capacity increased as the relative density increased, as expected. Location was taken into account in two ways: burial depth and horizontal distance from the center. Bearing capacity increased as the burial depth of the pipe increased, as expected. The highest bearing capacity loss was observed when the backfill soil had a relative density of 50%. Moreover, the highest stress ratio on the pipe was observed when the backfill soil had a relative density of 50%. In terms of horizontal distance, with increasing horizontal distance, bearing capacity increased.

Nevertheless, according to the results of Comparison 11, it can be seen that the backfill soil of the modern test, which pipe located at x/B=0, has a bigger bearing capacity than both x/B=0.75 and centered. This situation was not encountered in loose state soils or burial depth H/B=0.75. Therefore, with increasing burial depth and relative density, horizontal offset may not always mean increased bearing capacity for the buried pipes.

REFERENCES

Ahmed, M.R., V.D.H. Tran and M.A. Meguid, 2015, "On the Role Geogrid Reinforcement in Reducing Earth Pressure on Buried Pipes: Experimental and Numerical Investigations", *Soils and Foundation*, Vol. 55, No. 3, pp. 588-599.

Bildik, S. and M. Laman, 2019, "Experimental Investigation of Soil-Structure-Pipe Interaction", *KSCE Journal of Civil Engineering*, Vol. 23, No. 9, pp. 3753-3763.

Chapman, D., P. Fleming, C. Rogers and R. Talby, 2007, "The Response of Flexible Pipes Buried in Sand to Static Surface Stress", *Geomechanics and Geoengineering: An International Journal*, Vol. 2, pp. 17-28.

Chen, Y., F. Lu, A. Namdar and J. Cai, 2019, "Working mechanism of Pile Group 101 with Different Pile Spacing", *Advances in Civil Engineering*, Vol. 2019, pp. 150-272.

Coduto, D., W. Kitch and M.C. Yeung, 2015, *Foundation Design: Principles and Practices*, Third Edition, Pearson, Boston.

Daiyan, N., S. Kenny, R. Philips and R. Popescu, 2010, "Numerical Investigation of Oblique Pipeline/Soil Interaction In Sand", *Proceedings of the 8th. International Pipeline Conference*, Alberta, Canada, Vol. 2, pp. 154-167.

Duan, X.F., Y.F. Wang and X.M. Yuan, 2019, "State-of-the-Art Review of Particle Image Velocimetry (PIV) in Geotechnical Engineering", *International Confrence on Applied Mechanics*, Mathematics, Modeling and Simulation, Hong Kong, China, Vol 1. pp. 482-488.

Elshesheny, A., Mohamed, M. and T. Sheehan, 2019, "Buried Flexible Pipes Behaviour in Unreinforced and Reinforced Soils Under Cyclic Loading", *Geosynthetics Inter-*

national, Vol. 26, No. 2, pp. 184-205.

Fattah, M.Y., W.H. Hassan and S.E. Rasheed, 2018, "Behavior of Flexible Buried Pipes under Geocell Reinforced Subbase Subjected to Repeated Loading", *International Journal of Geotechnical Earthquake Engineering*, Vol. 9, No. 1, pp. 22-41.

Grant, I., "Particle Image Velocimetry: A Review", 1997, *Proceedings of the Institution of Mechanical Engineers, Part C: Journal of Mechanical Engineering Science*, Vol. 211, No. 1, pp. 55–76.

Hoeg, K., 1968, "Stresses against Underground Structural Cylinders, American Society of Civil Engineers Proceedings", *Journal of the Soil Mechanics and Foundation Division*, Vol. 94, No.4, pp. 853-858.

Kawabata, T., K. Uchida, T. Hirai, Y. Mohri, H. Ling and N. Koyama, 2003, "Experiments on Buried Pipe Using Backfill of Cover with Geosynthetics", *in Pipeline Engineering and Construction International Conference 2003*, Mohammad Najafi, Baltimore, Maryland, United States, pp. 1271– 1278.

Kou, Y. and S. Shukla, 2019, "Analytical Investigation of Load Over Pipe Covered with Geosynthetic-Reinforced Sandy Soil", *International Journal of Geosynthetics and Ground Engineering*, Vol. 5, No. 5, pp. 1-8.

Lu, H., S. Behbahani, M. Azimi, J.C. Matthews, S. Han, T. Iseley, 2020, "Trenchless Construction Technologies for Oil and Gas Pipelines: State-of-the-art Review", *Journal of Construction Engineering and Management*, Vol. 146, No. 6, pp. 110-135.

Maljaei, S.R., H. Katebi, M. Mahdi and A. Javadi, 2021, "Modeling of Uplift Resistance of Buried Pipeline by Geogrid and Grid-Anchor System", *Journal of Pipeline Systems Engineering and Practice*, Vol. 13, No. 1, p.04021075.

Marshall, A.M., R. Farrel, A. Klar and R. Mair, 2010, "Tunneling Beneath Buried Pipes: View of Soil Strain and Its Effect on Pipeline Behavior", *Journal of Geotechnical and Geoenvironmental Engineering*, Vol. 136, No. 12, pp. 1664-1672.

Mehrjardi, G.T., S.N. Moghaddas Tafreshi, A.R. Dawson, 2012, "Combined Use of Geocell Reinforcement and Rubber Soil Mixtures to Improve Performance of Buried Pipes", *Geotextiles and Geomembranes*, Vol. 34, No. 1, pp. 116-130.

Moore, I. D., 2001, *Buried Pipes and Culverts*, Springer US, Boston.

Oner, C., 2020, *Influence of Buried Pipes on Deformations Near Shallow Foundations*, M.S. Thesis, Bogazici University.

Paulin, M.J., R. Philips, Clark, J.I., Trigg, A. and I. Konuk, 1998, "A Full-Scale Investigation Into Pipeline/Soil Interaction", *Proceedings of the 2nd. International Pipeline Conference*, Alberta, Canada, Vol. 2, pp. 779-787.

Pires, A.C.G. and E.M. Palmeria, 2017, "Geosynthetic Protection for Buried Pipes Subjected to Surface Surcharge Loads", *International Journal of Geosynthetics and Ground Engineering*, Vol. 3, No. 4, pp. 1-11.

Spangler, M.G. and R.L. Handy, 2007, *Geotechnical Engineering: Soil and Foundation Principles and Practice*, Fifth Edition, McGraw-Hill, New York.

Stanier, S., J. Blaber, W. Take and D. White, 2015, "Improved Image-Based Deformation Measurement for Geotechnical Applications", *Canadian Geotechnical Journal*, Vol.53, pp. 1-13.

Tafreshi, S. M. and O. Khalaj, 2011, "Analysis of Repeated-Load Laboratory Tests on Buried Plastic Pipes in Sand", *Soil Dynamics and Earthquake Engineering*, Vol.31, No.1, pp. 1-15.

Terzaghi, K., 1943, *Theoretical Soil Mechanics*, Wiley, New York.

Terzi, N.U., 2007, *Gömülü Borulara Etkiyen Düşey ve Yatay Yüklerin Boru Stabilitesine Olan Etkilerinin Araştırılması*, Ph.D. Thesis, Yıldız Teknik Üniversitesi.

Wang, D.-Y., Z. Hong-Hu, W. Bao-Jun and B. Shi, 2021, "Performance Evaluation of Buried Pipe Under Loading Using Fiber Bragg Grating and Particle Image Velocimetry Techniques", *Measurement*, Vol.186, p. 110086.

White, D., W. Take and M. Bolton, 2003, "Soil Deformation Measurement Using Particle Image Velocimetry (PIV) and Photogrammetry", *Geotechnique*, Vol. 53, pp. 619-631.

Won, M.S., Ling H.I., H.I. Kim, 2004, "A Study of the Deformation of Flexible Pipes Buried under Model Reinforced Sand", *KSCE Journal of Civil Engineering*, Vol. 8, pp. 377-385.

Wu, J., G. Kouretzis and L. Suwal, 2021, "Bearing Capacity Mechanisms for Pipes Buried in Sand", *Canadian Geotechnical Journal*, Vol. 58, No. 6, pp. 834-847.

APPENDIX A: MODEL FOOTING SETTLEMENT AND BASE PRESSURE VALUES OF MODEL TESTS

Table A.1. Model footing and base pressure values of T1.

S(**mm**)	Q(**kPa**)
0	0.00
2	7.53
4	21.38
6	30.55
8	37.83
10	43.61
12	49.00
14	52.47
16	53.67
18	55.00
20	55.94

Table A.2. Model footing and base pressure values of T2.

S(**mm**)	Q(**kPa**)
0	0.00
2	10.05
4	17.06
6	23.27
8	29.11
10	32.25
12	34.22
14	36.34
16	40.10
18	43.04
20	45.91

Table A.3. Model footing and base pressure values of T3.

S**(mm)**	Q**(kPa)**
0	0.00
2	16.18
4	27.43
6	36.01
8	43.25
10	48.95
12	53.24
14	56.65
16	60.21
18	64.85
20	69.15

Table A.4. Model footing and base pressure values of T4.

S**(mm)**	Q**(kPa)**
0	0.00
2	32.44
4	51.96
6	61.77
8	71.94
10	74.25
12	75.50
14	76.62
16	78.51
18	80.29
20	81.45

Table A.5. Model footing and base pressure values of T5.

S(**mm**)	Q(**kPa**)
0	0.00
2	27.40
4	44.40
6	54.57
8	62.07
10	68.17
12	73.51
14	78.50
16	78.32
18	84.81
20	87.50

Table A.6. Model footing and base pressure values of T6.

S(**mm**)	Q(**kPa**)
0	0.00
2	28.95
4	50.64
6	63.93
8	69.99
10	73.70
12	74.62
14	72.97
16	75.63
18	78.60
20	81.88

Table A.7. Model footing and base pressure values of T7.

S**(mm)**	Q**(kPa)**
0	0.00
2	24.14
4	47.49
6	67.54
8	82.48
10	95.12
12	104.97
14	107.25
16	102.30
18	102.39
20	103.42

Table A.8. Model footing and base pressure values of T8.

S**(mm)**	Q**(kPa)**
0	0.00
2	22.15
4	43.08
6	58.84
8	68.55
10	75.40
12	75.58
14	69.85
16	70.92
18	71.71
20	73.61

Table A.9. Model footing and base pressure values of T9.

S**(mm)**	Q**(kPa)**
0	0.00
2	39.75
4	62.36
6	76.46
8	80.94
10	77.31
12	78.88
14	82.51
16	86.09
18	87.84
20	88.36

Table A.10. Model footing and base pressure values of T10.

S**(mm)**	Q**(kPa)**
0	0.00
2	4.31
4	9.06
6	16.76
8	23.78
10	29.40
12	32.84
14	35.84
16	38.42
18	40.78
20	43.22

Table A.11. Model footing and base pressure values of T11.

S(**mm**)	Q(**kPa**)
0	0.00
2	13.48
4	22.76
6	27.84
8	31.82
10	34.38
12	36.64
14	N.D.
16	N.D.
18	N.D.
20	N.D.

Table A.12. Model footing and base pressure values of T12.

S(**mm**)	Q(**kPa**)
0	0.00
2	11.25
4	19.09
6	27.88
8	34.54
10	41.35
12	45.12
14	45.16
16	47.34
18	49.73
20	52.40

Table A.13. Model footing and base pressure values of T13.

S(**mm**)	Q(**kPa**)
0	0.00
2	11.63
4	28.05
6	47.16
8	60.50
10	68.16
12	72.42
14	71.16
16	69.93
18	71.35
20	71.61

Table A.14. Model footing and base pressure values of T14.

S(**mm**)	Q(**kPa**)
0	0.00
2	35.87
4	53.40
6	64.51
8	70.00
10	70.72
12	69.86
14	68.83
16	68.51
18	69.46
20	70.48

Table A.15. Model footing and base pressure values of T15.

S(**mm**)	Q(**kPa**)
0	0.00
2	35.06
4	52.80
6	67.69
8	80.25
10	88.84
12	90.46
14	85.74
16	82.16
18	82.02
20	82.59

Table A.16. Model footing and base pressure values of T16.

S(**mm**)	Q(**kPa**)
0	0.00
0	0.00
2	14.52
4	28.05
6	50.66
8	68.73
10	86.47
12	92.64
14	93.78
16	93.72
18	96.15
20	100.26

Table A.17. Model footing and base pressure values of T17.

S(**mm**)	Q(**kPa**)
0	0.00
2	27.47
4	48.46
6	60.17
8	70.81
10	79.96
12	84.15
14	83.41
16	84.12
18	85.74
20	86.04

Table A.18. Model footing and base pressure values of T18.

S(**mm**)	Q(**kPa**)
0	0.00
2	25.38
4	53.46
6	67.18
8	80.42
10	89.78
12	93.06
14	90.84
16	91.70
18	93.91
20	96.32

APPENDIX B: STRESSES ACTING ON A PIPE AND CORRESPONDING SETTLEMENT VALUES

Table B.1. Pipe stresses and corresponding settlement values in T2.

s_C (kPa)	s_R (kPa)	s_L (kPa)	S (mm)
0	0	0	0
-1.44	1.44	1.32	2
-3.72	3.30	3.30	4
-6.06	5.34	5.34	6
-8.58	7.38	7.50	8
-9.96	8.40	8.46	10
-9.36	8.34	8.22	12
-9.06	8.34	8.22	14
-9.84	9.18	9.00	16
-10.44	9.84	9.54	18
-11.10	10.50	10,14	20

Table B.2. Pipe stresses and corresponding settlement values in T3.

s_C (kPa)	s_R (kPa)	s_L (kPa)	S (mm)
0	0	0	0
-0.84	0.6	0.72	2
-1.62	1.26	1.44	4
-2.22	1.86	1.98	6
-2.88	2.34	2.40	8
3.42	3.00	2.82	10
-3.78	3.36	3.06	12
-4.02	3.06	3.30	14
-4.32	3.30	3.48	16
-4.86	3.60	3.90	18
-5.34	3.90	4.20	20

Table B.3. Pipe stresses and corresponding settlement values in T5.

s_C **(kPa)**	s_R **(kPa)**	s_L **(kPa)**	S **(mm)**
0	0	0	0
-8.10	7.32	6.66	2
-17.28	16.68	15.30	4
-25.86	25.50	23.52	6
-33.66	33.78	30.48	8
-42.06	42.60	37.98	10
-50.34	51.00	45.12	12
-59.70	59.94	52.56	14
-69.60	66.06	59.22	16
-79.68	73.62	66.48	18
-89.52	81.60	72.66	20

Table B.4. Pipe stresses and corresponding settlement values in T6.

s_C **(kPa)**	s_R **(kPa)**	s_L **(kPa)**	S **(mm)**
0	0	0	0
-4.26	2.10	2.58	2
-13.38	8.52	10.02	4
-20.58	14.04	16.26	6
-25.68	18.60	20.94	8
-30.60	22.44	24.00	10
-31.68	24.00	24.60	12
-29.52	24.48	23.46	14
-29.10	24.84	22.56	16
-30.42	25.56	22.98	18
-32.22	26.70	23.64	20

Table B.5. Pipe stresses and corresponding settlement values in T8.

s_C **(kPa)**	s_R **(kPa)**	s_L **(kPa)**	S **(mm)**
0	0	0	0
-1.02	0.30	0.28	2
-7.56	5.40	5.02	4
-13.80	11.40	10.60	6
-18.90	16.62	15.46	8
-24.78	23.10	21.48	10
-29.88	28.08	26.11	12
-39.60	30.42	28.30	14
-43.92	32.88	30.58	16
-43.26	33.30	32.58	18
-41.88	32.22	32.28	20

Table B.6. Pipe stresses and corresponding settlement values in T9.

s_C **(kPa)**	s_R **(kPa)**	s_L **(kPa)**	S **(mm)**
0	0	0	0
-4.26	1.86	1.73	2
-9.96	5.04	4.69	4
-13.86	7.62	7.09	6
-15.42	9.84	9.15	8
-15.36	12.66	11.77	10
-16.02	14.16	13.17	12
-17.94	15.00	13.95	14
-21.12	16.32	15.18	16
-24.00	17.46	16.24	18
-25.14	18.00	16.74	20